Statistical Models for Characterizing Heterogeneous Wake Effects in a Wind Farm

by

Mingdi You

A dissertation submitted in partial fulfillment
of the requirements for the degree of
Doctor of Philosophy
(Industrial and Operations Engineering)
in the University of Michigan
2017

Doctoral Committee:

Assistant Professor Eunshin Byon, Chair
Associate Professor Veronica Berrocal
Associate Professor Seth Guikema
Professor Judy Jin

Mingdi You

mingdyou@umich.edu

ORCID iD: 0000-0002-5213-2107

To my family

ACKNOWLEDGEMENTS

This dissertation would not been accomplished without support from lots of people. I would like to express my sincere appreciations to all of them.

First, I would like to thank my advisor, Professor Eunshin Byon, for her inspiration and guidance throughout my study and research. I deeply appreciate her insightful encouragements and endless patience, which eventually help me become a qualified researcher.

I would also express my immense gratitude to other committee members, Professor Judy Jin, Professor Seth Guikema, and Professor Veronica Berrocal. Their intelligent advices and comments guide me through lots of challenges from both the course work and research.

I am also grateful for other faculty and staff at the IOE department, particularly Tina, Matt, Chris, Professor Siqian Shen, and Professor Xiuli Chao, for their assistance and suggestions. I also want to thank my fellow students in Ann Arbor: Dr. Youngjun Choe, Dr. Grace Guo, Yaser Zerahsaz, Qiyun Pan, Yuhui Shi, and Wenyi Wu.

Last but not least, I want to thank my family for their unconditional love. Without their support, I would not have chance to get the Ph.D degree.

PREFACE

This dissertation consists of five chapters. Chapter I introduces the background and motivation of my research to readers. Chapters II to IV discuss three main topics in my research. Chapter II is based on the published article (*You et al.*, 2017), which was originally published by the Taylor & Francis. The Taylor & Francis group gives me the permission to reuse the content in this dissertation. Chapters III and IV are based on my working manuscripts. Chapter V concludes the dissertation with a summary of contributions and future research directions.

TABLE OF CONTENTS

LIST OF FIGURES

Figure

LIST OF TABLES

Table

LIST OF ABBREVIATIONS

KW kilowatt

MW megawatt

GW gigawatt

VG vortex generator

GMRF Gaussian Markov random field

CFD computational fluid dynamics

LES large eddy simulation

NREL National Renewable Energy Laboratory

SCADA Supervisory Control and Data Acquisition

MCMC Markov Chain Monte Carlo

WinBUGS Microsoft Windows operating system version of BUGS: Bayesian Analysis Using Gibbs Sampling

met-tower meteorology tower

CV cross validation

RMSE root mean square error

MAE mean absolute error

APG average power gain

NTF Nacelle Transfer Function

MLE maximum likelihood estimation

ABSTRACT

Statistical Models for Characterizing Heterogeneous Wake Effects in a Wind Farm

by

Mingdi You

Chair: Eunshin Byon

Wind energy is becoming one of the most promising renewable sources. With the rapid growth of wind energy, modern utility-scale wind farms consist of a large number of wind turbines. In order to improve the power generation efficiency of wind turbines, an accurate quantification of power generations from multiple turbines is critical in both wind farm design and operational controls. One challenging issue is that the power outputs from turbines are different from a stand-alone turbine because of complex interactions among turbines, known as the wake effects. In general, upstream turbines absorb kinetic energy from wind. Therefore, downstream turbines tend to produce less power than upstream turbines. Moreover, depending on weather conditions, the power deficits of downstream turbines exhibit heterogeneous patterns.

In order to address these challenges, this dissertation study initiates two major ideas: (1) to analyze the stochastic nature of generating wind energy, this study avoids the traditional approach which focuses on wind field modeling within a wind farm. Instead, this study proposes new statistical approaches that directly model the relationship between free-flow wind conditions and power generations from multiple turbines; (2) to analyze the physical interactions among wind turbines, this disserta-

tion proposes data-driven approaches in a comprehensive framework.

The objective of this research is to provide a new integrative methodology to characterize multi-turbines' heterogeneous performance at a wind farm scale. Specifically, this dissertation develops:

- a new statistical model for characterizing heterogeneous wake effects under the dominant wind direction;
- a canonical model-based approach to handle wake effects under different wind directions; and
- a new method to quantify the improvement of power productions through retrofitting, e.g., the vortex generator (VG) installation.

In a wind farm, interactions among turbines alter the power generation efficiency of turbines. Moreover the power deficits of downstream turbines in a wind farm exhibit heterogeneous patterns, depending on wind conditions. This study first characterizes heterogeneous wake effects under a dominant wind direction. The proposed model decomposes the power outputs into the average pattern commonly exhibited by all turbines and the turbine-to-turbine variability caused by multi-turbine interactions. To capture the interactions among turbines, turbine-specific regression parameters are modeled using a Gaussian Markov random field (GMRF).

Second, the power curve of each turbine becomes heterogeneous when changes in wind directions cause some upstream turbines to become downstream turbines. This dissertation proposes an integrative methodology that quantifies the heterogeneous wake effects over a range of wind directions by utilizing the concept of canonical models and similarity functions. The direction-dependent multi-turbine power curves are modeled in a Bayesian hierarchical framework.

Lastly, based on the model quantifying the wake effects proposed in this dissertation, a new method is introduced to quantify the retrofitting effect on the power

generation performance. The result can help practitioners perform the cost and benefit analysis when they consider the retrofitting for existing turbines.

The advantages of all proposed approaches are demonstrated with the data collected from operational wind farms. The results of case studies validate that the proposed models successfully resolve some issues observed from the real world data.

CHAPTER I

Introduction

Wind energy is extracted from air flow by using wind turbines to produce electrical power. As an renewable energy source, wind energy produces no greenhouse gas emissions during operations and can be widely distributed (*Boyle*, 2012; *Enkvist et al.*, 2007; *Fthenakis and Kim*, 2009). These advantages make the wind energy one of the most promising energy sources in the United States (*U.S. Global Wind Energy Council*, 2015; *American Wind Energy Association*, 2015).

In the United States, wind energy installation increased by more than a factor of ten in the past decade, from 4.2 GW in 2001 to more than 60 GW by the end of 2014 as shown in Figure 1.1. The U.S. Department of Energy's Wind Vision study scenario, recently announced in *U.S. Department of Energy* (2015), envisions that wind energy will supply 35% of U.S. domestic electrical power by 2050.

Unlike fossil fuel-based power systems which generally operate in a steady state, wind power systems operate in highly stochastic conditions (*Barton and Infield*, 2004; *Kaltschmitt et al.*, 2007; *Weigt*, 2009; *Byon et al.*, 2010; *Byon*, 2013; *Lee et al.*, 2015a). Because the wind speed has been deemed the major factor influencing power productions, many data-driven methods including the neural network (*Barbounis et al.*, 2006; *Li et al.*, 2005), support vector regression (*Mohandes et al.*, 2004; *Yampikulsakul et al.*, 2014), and other statistical methods (*Damousis et al.*, 2004; *Chen et al.*,

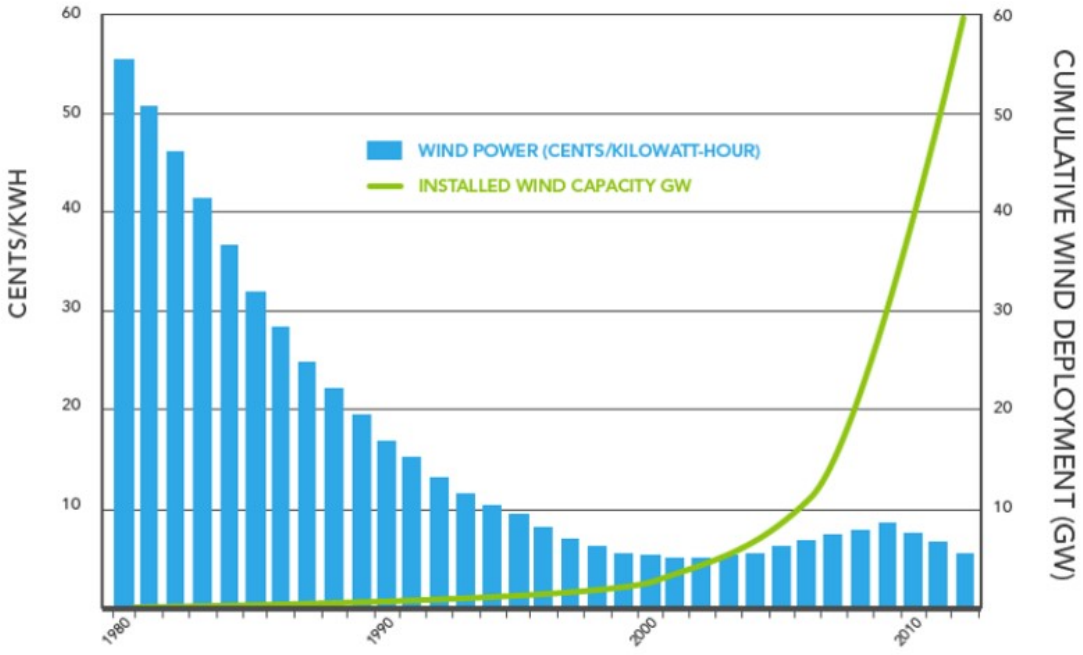

Figure 1.1: Rapid growth of the installed wind capacity in GW (excerpted from *American Wind Energy Association* (2014))

2010; *Sánchez*, 2006; *Byon et al.*, 2016) have been developed to quantify the power output at a single turbine, given a wind speed. This wind-to-power relationship is called a power curve in the wind industry (*Korpaas et al.*, 2003). Recently, turbulence intensity, air density, and other weather factors have also received attention in studying their effects on the power generation efficiency (*Bianchi et al.*, 2007; *Hansen et al.*, 2012; *Lee et al.*, 2013, 2015a).

A recent trend of wind energy projects is to develop and operate a large-scale wind farm with multiple turbines. As a result, modern utility-scale wind farms consist of dozens or hundreds of turbines in general. One interesting, yet, challenging aspect is that power generation patterns of multiple turbines in a wind farm are different from that of a stand-alone turbine; in fact, there are wide differences in power outputs due to the complex interactions, known as the wake effects, among turbines (*Crespo et al.*, 1999; *Vermeer et al.*, 2003; *Christiansen and Hasager*, 2005; *Kusiak and Song*, 2010; *Adaramola and Krogstad*, 2011). The explanation is simple. As wind passes through,

upstream turbines absorb kinetic energy from the wind. As a result, the downstream turbines installed behind the upstream turbines have less kinetic energy to convert, thus generating less power than the upstream turbines (see Figure 1.2). Although it is recommended to maintain a certain minimum spacing between turbines to alleviate the negative influence of wake effects on power loss, often it is not practical due to local geography and economic constraints such as transmission costs, etc. (*Kim et al.*, 2015). Therefore, maximizing the net energy production in the layout design (i.e., where to install turbines) (*Lackner and Elkinton*, 2007; *Kusiak and Song*, 2010; *Chowdhury et al.*, 2012) and operational controls (e.g., yaw and pitch control) (*de Almeida et al.*, 2006; *Johnson and Thomas*, 2009) relies heavily on accurately quantifying the wake effects in a utility-scale wind farm.

Figure 1.2: Wake effects (excerpted from *National Renewable Energy Laboratory* (2012), Courtesy of Vattenfall Wind Power, Denmark)

Some initial attempts have been made to understand the wake effects in wind farm

operations. The wake effects literature falls roughly into three categories. Studies in the first category focus on analytically predicting wind speeds at downstream turbines based on the physical understanding (*Jensen*, 1983; *Katic et al.*, 1986). Physics-based engineering models such as Jensen's model (*Jensen*, 1983), also known as the Park model, estimate the wind speed deficits at downstream turbines in an explicit functional form of the wind speeds at upstream turbines and other factors such as a distance between turbines. For mathematical tractability, these models are typically built upon simplifying assumptions and as such, they cannot capture the complicated nature of wake effects (*Staid*, 2015; *Yang et al.*, 2016).

Studies in the second category use sophisticated simulation models, such as computational fluid dynamics (CFD), to obtain detailed wind flow in wind farms (*Fleming et al.*, 2014; *Porté-Agel et al.*, 2010). Recently, Large Eddy Simulation (LES), which investigates the wake characteristics including the turbulence generated from wind turbines in fine scales, has proven valuable in reducing modeling uncertainties (*Wu and Porté-Agel*, 2011). However, running the numerical simulation model is extremely time-demanding. For example, *Fleming et al.* (2014) use SOWFA (Simulator fOr Wind Farm Applications), which is a high-fidelity simulation software developed by the National Renewable Energy Laboratory (NREL), and simulate the wake effects in a wind farm of size of 2142 meter (m) $\times$ 378 meter (m) with a single NREL 5-MW baseline turbine. It takes 34.4 hours to simulate 1000 seconds of turbine operations using the NREL Red Mesa supercomputer with 256 processors. Therefore, the application of this numerical approach has been limited to specific cases for detailed analysis, e.g., at certain wind conditions (*Fleming et al.*, 2014).

Lastly, the third approach develops statistical methods to estimate the spatial wind field in a wind farm (*Ailliot et al.*, 2006; *Lei et al.*, 2009; *Pourhabib et al.*, 2016; *Dowell and Pinson*, 2016). Recently, *Pourhabib et al.* (2016) employ vector autoregressive models to predict wind speeds using historical wind conditions collected from

anemometers mounted on each turbine's nacelle. However, the quantification of wake effects such as power deficits, or deficits in incoming wind speeds that turbines face, is not addressed because their focus is predicting downwind speeds at anemometers.

The three different approaches commonly focus on estimating the spatial wind field in a wind farm (see Figure 1.3). In these approaches, each turbine's power generation prediction is based on the wind-to-power relationship resulting from the estimated wind condition at the specific site. Under this framework, however, the estimation error in predicting the spatial wind field can be translated (or even escalated) to inaccurate power predictions. More importantly, this approach does not directly quantify the interactions of multiple turbines. As such, decision-makings of wind farm layout or operational controls would become complicated with these approaches.

The approach proposed in this dissertation focuses on directly estimating the performance of multiple interacting turbines, instead of estimating the spatial wind field in a wind farm (see Figure 1.4). In particular, we study three specific topics, which are briefly outlined below.

1.1 Characterizing Heterogeneous Wake Effects in the Dominant Wind Direction

To better understand the relationship between wake effects and the differences in power generations, Chapter II proposes a new modeling approach that directly quantifies different power generations at multiple interacting turbines in the dominant wind direction. The proposed approach has two components. The first component characterizes the general nonlinear relationship between the power generation and weather conditions, which are commonly exhibited in all of the turbines in a wind farm. We call this a global trend and model it with spline functions. The second component captures the turbine-to-turbine variations caused by the wake effects. We

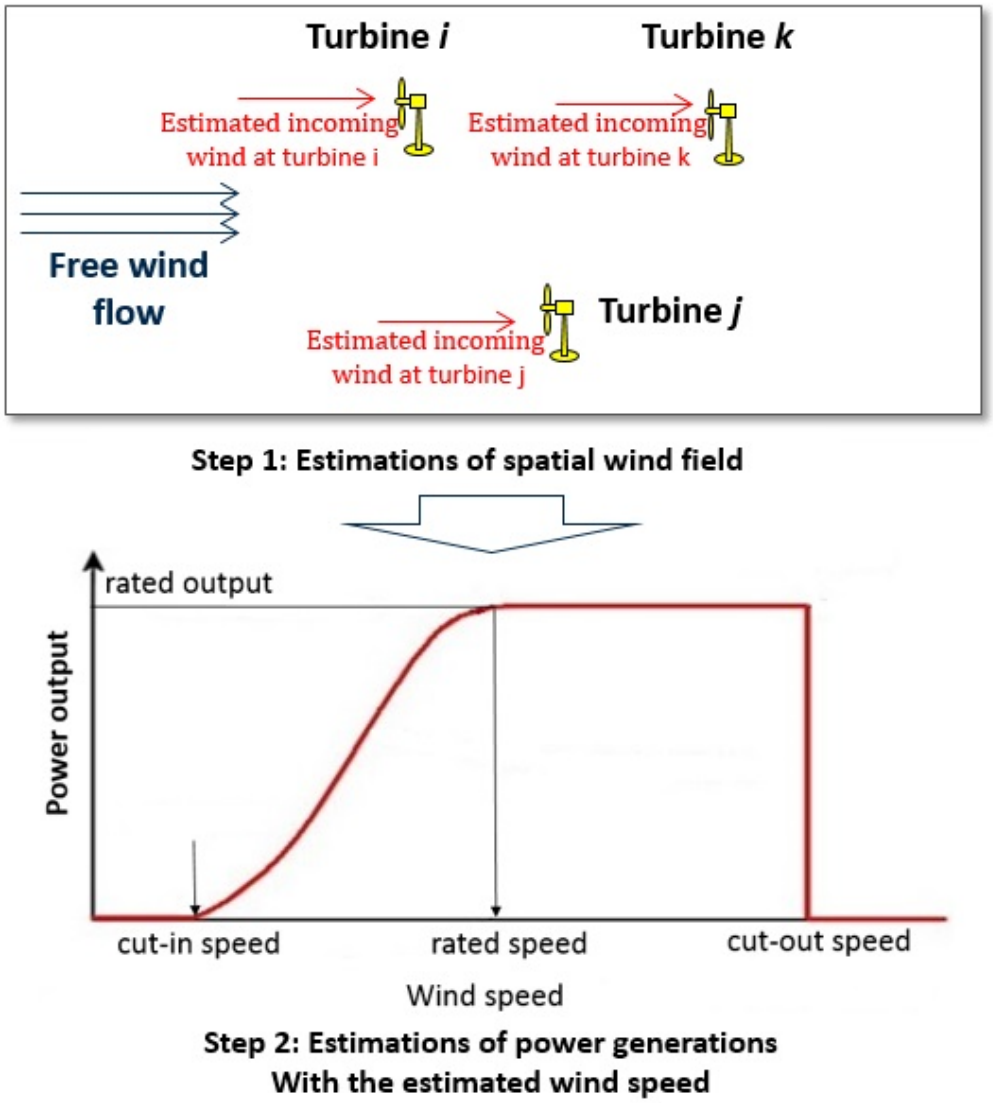

Figure 1.3: Existing two-step approach for estimating power generations in multiple turbines

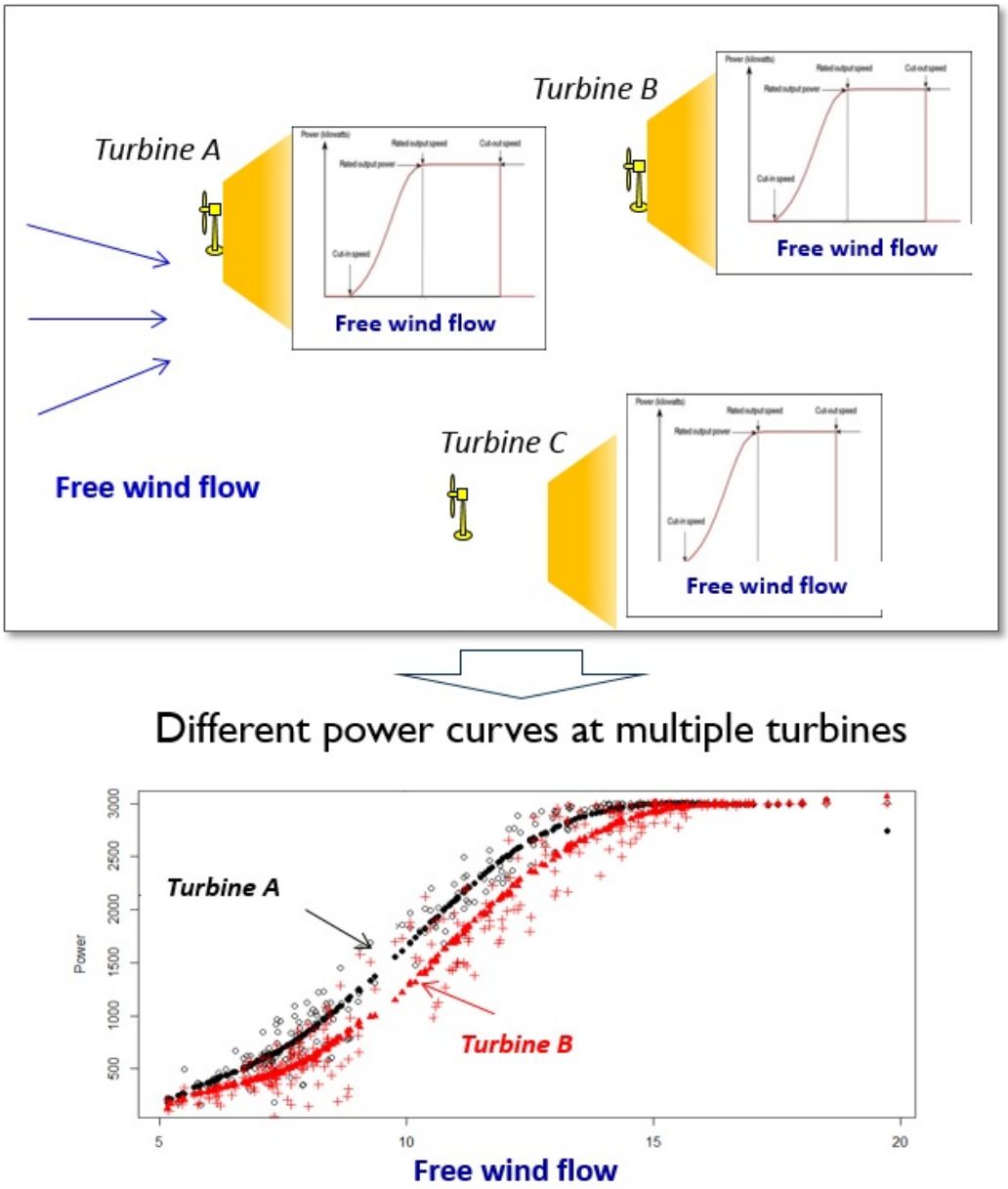

Figure 1.4: Proposed approach: Estimating the power generations based on the free-flow wind

call this spatial variations in this study.

In particular, the differences of power outputs among turbines are heterogeneous, depending on weather conditions. To characterize such heterogeneous turbine interactions, we model the spatial variations with spline functions of weather conditions where the spline regression parameters are modeled with GMRF (*Rue and Held*, 2005; *Cressie*, 2015; *Banerjee et al.*, 2014). Our implementation results with wind farm data collected during actual operations indicate that the proposed approach can successfully quantify the heterogeneous wake effects, demonstrating its superior performance over other alternative methods.

1.2 Direction-dependent Power Curve Modeling for Multiple Interacting Wind Turbines

In modeling the wake effects, one of the important weather factors is the wind direction. When the wind direction changes, the power generation pattern of wind turbines also changes. Building upon the approach in Chapter II, Chapter III models the direction-dependent power curves of multi-turbines, providing an integrative framework that quantifies the power generation performance of turbines in all wind directions.

To learn the heterogeneous power curves in different directions, a set of representative models, referred to as canonical spatial models, is introduced in Chapter III. Let us consider K canonical spatial models, each of which corresponds to its canonical wind direction. For example, with $K = 4$, we consider four spatial models representing the power variation patterns in four directions, e.g., 45°, 135°, 225° and 315°. In practice, the incoming wind direction ranges between 0° and 360°. For example, when wind direction is 70°, the wake pattern would be similar to that in 90°, but also resembles the wake pattern in 0° to some extent. As such, in constructing power curves,

we consider the similarities to the canonical models. We treat the canonical models as latent and integratively learn them by modeling the direction-dependent power curves in the Bayesian hierarchical inference and estimating the model parameters using the Markov Chain Monte Carlo (MCMC) (*Banerjee et al.*, 2014).

1.3 Quantification of the VG Upgrade under Wake Effects

In order to improve the performance of existing turbines, industry practitioners consider several upgrading or retrofitting technologies such as installation of VGs on turbine blades (*Flohr et al.*, 2003; *Mueller-Vahl et al.*, 2012; *Brake et al.*, 2014). However, upgrading existing turbines is costly due to expensive material, labor and equipment rental costs. Practitioners are often interested in how much those upgrades can improve the power generation efficiency to perform cost and benefit analysis in their investment decision-making.

Among several upgrading technologies, we consider the effect of VG installation on the power generation efficiency (see the red fins in Figure 1.5). The VG is designed to help wind turbine generate more power by improving the blades' lift characteristics and reducing the vibrations of wind flows (*Lee et al.*, 2015b).

Recently *Lee et al.* (2015b) propose a kernel-based statistical model to quantify the power gain due to the VG's installation, but they do not consider the VG effect in the presence of wake effects. When a turbine that undergoes the upgrade is inside a wind farm, it is important to quantify the power gain considering wake effects. Based on the model discussed in Chapter II, Chapter IV quantifies the VG performance upgrade. We also investigate how the VG upgrade in one turbine affects its downstream turbines.

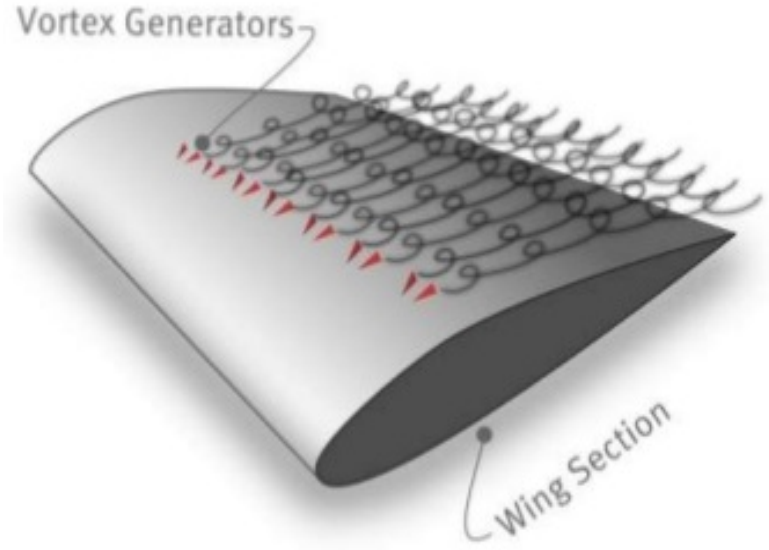

Figure 1.5: Vortex generator (VG) attached to a wind turbine blade (excerpted from *UpWind Solutions* (2015))

CHAPTER II

Characterizing Heterogeneous Wake Effects in the Dominant Wind Direction

2.1 Introduction

In general, turbines in downwind rows are impacted by wind deficits, producing less power, compared to upstream turbines. Therefore, the generation performance of multiple turbines differs from one another. We describes dynamic characteristics of wake effects using a real data. Figure 2.1 shows a partial layout of the actual wind farm with 30+ turbines used in this chapter (for confidentiality, the geographical coordinates have been rotated). The x- and y-axes, scaled in 0-1 in the x-axis and 0-1.5 in the y-axis, depict the relative locations of the turbines in the longitude and latitude in the rotated coordinates. The solid circles represent the wind turbines, and the solid square is the meteorology tower (henceforth, met-tower) that collects meteorological measurements including wind speed, wind direction, turbulence intensity, air density and humidity. The height of the met-tower and the hub heights of the wind turbines are the same in this wind farm.

The wind farm considered in this study has only one met-tower, which is placed facing the dominant wind direction. Therefore, the met-tower can measure the free-flow wind conditions in most times. However, when wind blows in non-dominant

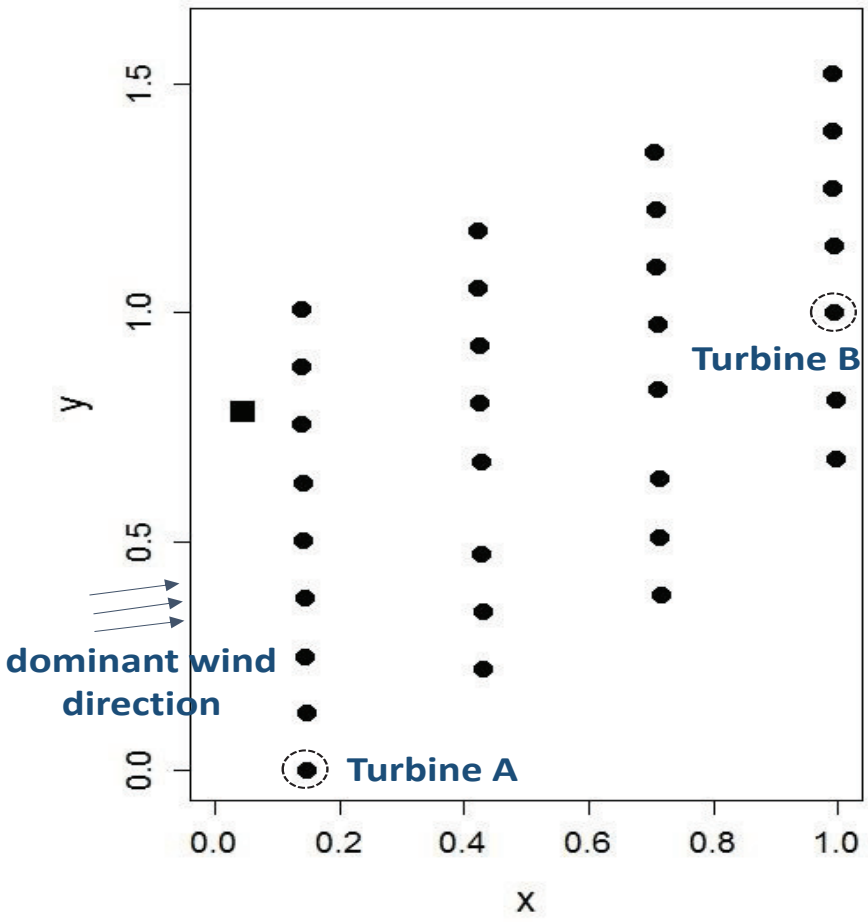

Figure 2.1: Wind farm layout

directions, the met-tower falls into the wake region, and the data collected at the met-tower does not represent the free-flow wind. In this chapter we limit our analysis in the dominant wind direction and use the data collected when the met-tower is not under wake. Under this direction, Turbine A in Figure 2.1 is an upstream turbine, and Turbine B in Figure 2.1 becomes a downstream turbine.

To understand the impacts of ambient wind conditions on power generations, Figure 2.2 shows the scatter plots of power generations from Turbine A and B versus the wind speed. The y-axis is the 10-minute average power generation in the standardized 0-1000 scale (we re-scale the power to 0-1000 to retain the data confidentiality), and the x-axis is the 10-minute average wind speed collected at the met-tower. The "+" marks indicate the power outputs from Turbine A, and the "$\circ$" marks correspond to the outputs from Turbine B. Figure 2.2 shows that both Turbine A and B tend to generate more power as the wind speed increases up to about $14 \sim 15$ meters per second (m/s) and then generate a steady level of power due to their blade pitch controls which reduce energy absorption to protect their blades in strong wind conditions (*Bianchi et al.*, 2007; *Yampikulsakul et al.*, 2014; *Lee et al.*, 2013).

Although all turbines in a wind farm exhibit similar nonlinear patterns shown in Figure 2.2, the power generation differs among multiple turbines due to their complex interactions in the spatial neighborhood. In particular, downstream turbines exhibit power deficits (i.e., smaller power generations) due to the wake effects and that the power deficits show heterogeneous patterns, depending on the wind condition. As Figure 2.2 shows, the difference of power outputs between Turbine A and B tends to increase as wind speed increases, and then diminishes under high wind speeds.

To understand the heterogeneous wake effects over a range of wind conditions in multiple turbines, Figure 2.3(a) depicts the power generations in one of the samples in the dataset when the wind speed is 12 m/s. The colors of each circle indicate the power generation levels at each turbine. A darker color in the solid circle repre-

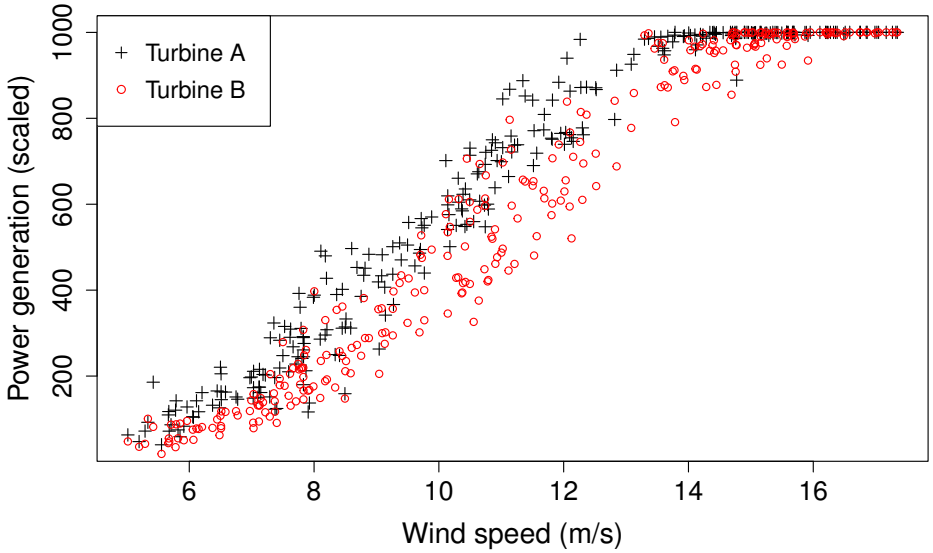

Figure 2.2: Heterogeneous power generation patterns at two turbines

sents a larger power generation. Note that in general, turbines on the left (upstream turbines) produce more power than those on the right (downstream turbines). On the contrary, the differences among power generations from multiple wind turbines are not significant when the wind speed is very low (Figure 2.3(b)) or high (Figure 2.3(c)). The rationale is when the wind speed is low (Figure 2.3(b)), upstream turbines' blades rotate slowly and a small amount of energy is extracted from wind. As a result, the energy loss due to the wake effects for the downstream turbines is not significant. Moreover, while the wind travels from upstream turbines to downstream turbines, it can recover energy to some extents. When the wind speed is high (Figure 2.3(c)), upstream turbines use pitch controls to generate a steady level of power, called the rated power, and they do not extract the maximum energy they can. As such, downstream turbines still face incoming wind with sufficient energy to convert to the rated power.

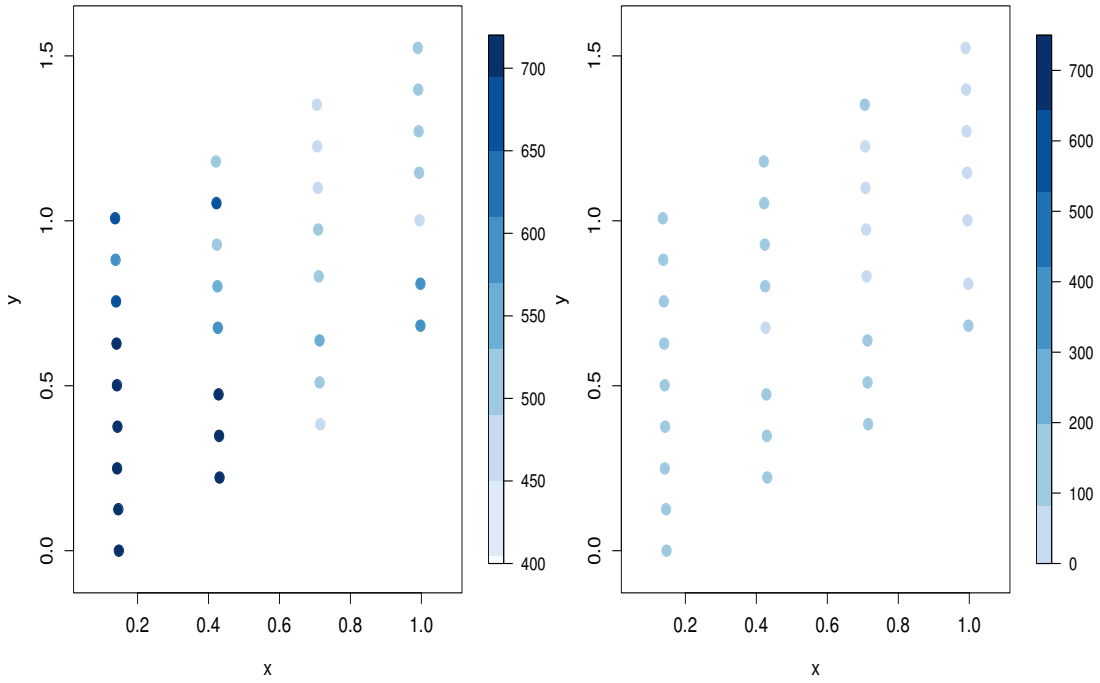

(a) When wind speed is 12 m/s

(b) When wind speed is 5 m/s

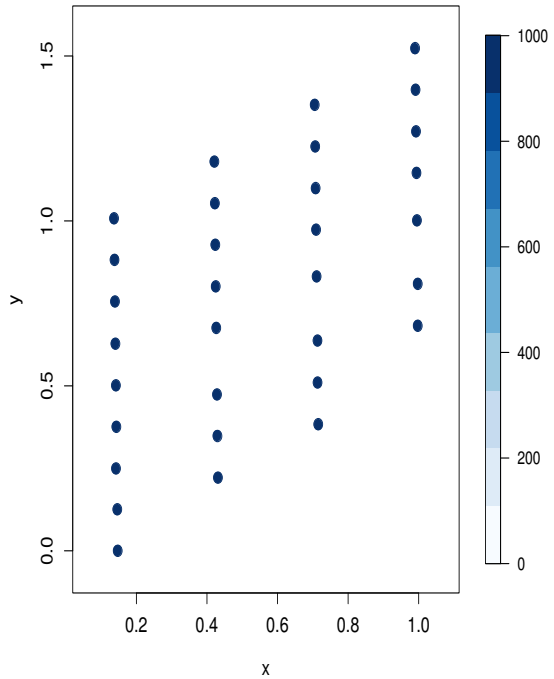

(c) When wind speed is 14 m/s

Figure 2.3: Power generations at multi-turbines under different wind speeds

2.2 Mathematical Model

This section provides a new modeling framework that addresses the heterogeneity in the power generation performance of multiple turbines, caused by the spatial variations coupled with wind conditions. Let $Y_{n,i}$ $(n = 1, \cdots, N; i = 1, 2, \cdots, I)$ be the power output of the n^{th} turbine at the i^{th} sample in the dataset, where N is the number of wind turbines in the wind farm and I is the total number of samples in the dataset. Let $\mathbf{x}_i = [x_i^1, x_i^2, \cdots, x_i^K]^T$ denote a vector of weather covariates (e.g. wind speed, turbulence intensity) at the i^{th} sample, measured at the met-tower, where K is the number of weather factors considered in the model.

We model the power generations at multiple turbines by decomposing the power output $Y_{n,i}$ into the global trend component $G(\cdot)$ and the spatial component $S(\cdot)$ as

$$Y_{n,i} = G(\mathbf{x}_i; \beta) + S(\mathbf{x}_i; \gamma_n) + \epsilon_{n,i}, \quad n = 1, \cdots, N; \; i = 1, \cdots, I, \tag{2.1}$$

where $\epsilon_{n,i}$ represents the white noise which is assumed to be an independent Gaussian random variable with the mean 0 and variance σ^2. Figure 2.2 shows the similarities in the general power generation patterns of multiple turbines. The first term $G(\cdot)$ explains the average pattern that turbines commonly exhibit in response to weather condition $\mathbf{x}_i$. In $G(\cdot)$, all of the turbines share the same parameter vector β. The second term $S(\cdot)$ handles the turbine-to-turbine variability with the turbine-specific random effect vector, γ_n. Figure 2.4 illustrates the idea of this decomposition scheme.

For notational simplicity, we suppress the subscript i in the subsequent discussions when no confusion arises, and use the model,

$$Y_n = G(\mathbf{x}; \beta) + S(\mathbf{x}; \gamma_n) + \epsilon_n, \quad n = 1, \cdots, N. \tag{2.2}$$

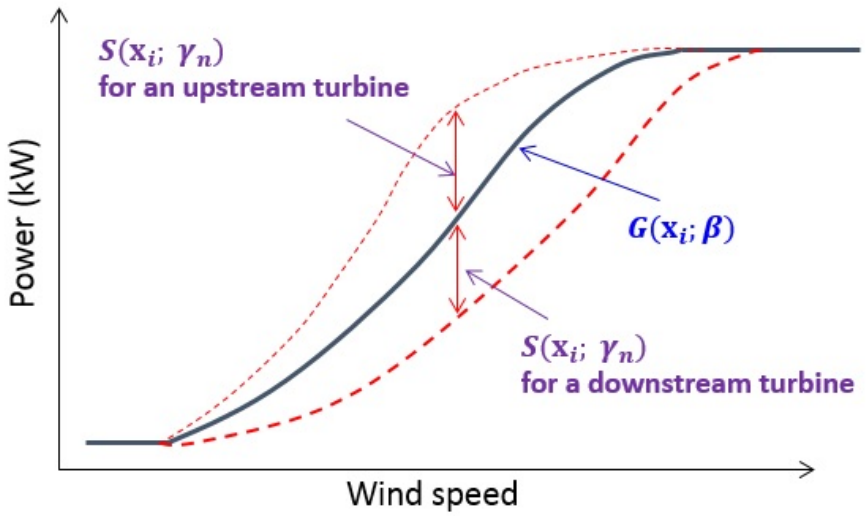

Figure 2.4: The illustration of the global-spatial decomposition in (2.1)

2.2.1 Modeling the global pattern

First, we model the global component $G(\mathbf{x};\beta)$ in (2.2) to represent the nonlinear pattern between the power output and weather conditions as shown in Figure 2.2. In the literature, several nonlinear regression methods, including the kernel-based method (*Salcedo-Sanz et al.*, 2011; *Jeon and Taylor*, 2012; *Bessa et al.*, 2012; *Lee et al.*, 2015b), support vector regression (*Mohandes et al.*, 2004; *Salcedo-Sanz et al.*, 2011; *Yampikulsakul et al.*, 2014), and neural networks (*Kariniotakis et al.*, 1996; *Li et al.*, 2001; *Quan et al.*, 2014), are proposed to capture the nonlinear relationship between weather covariates and power generations for a single turbine. Even though they can possibly capture the global patterns that multi-turbines commonly exhibit, they have limitations in incorporating turbine-to-turbine interactions. In this study, we use the spline regression (*Harvey and Koopman*, 1993; *Lee et al.*, 2013; *Friedman et al.*, 2009; *Choe et al.*, 2015) in the global term because it can be easily combined with the spatial component, while successfully capturing the nonlinearity.

Among various spline models, we use the basis spline, or B-spline, because it empirically shows a good performance in the dataset we used in this study. Specifically,

with the input data with K weather factors, $\mathbf{x} = [x^1, x^2, \cdots, x^K]^T$, we model $G(\mathbf{x}; \beta)$ as

$$G(\mathbf{x}; \beta) = \sum_{k=1}^{K} \mathbf{x}^{g,k} \beta^k, \tag{2.3}$$

where $\mathbf{x}^{g,k}$ is a row vector in the design matrix for the B-spline basis corresponding to the k^{th} weather factor x^k, and β^k is a column vector consisting of associated spline regression coefficients. We include the detailed description of the B-spline basis in Section 2.6.1.

2.2.2 Modeling the spatial variations

This section models the spatial variations. To capture the turbine-to-turbine variations, one common method is to use a random effect δ_n and model the power output Y_n as

$$Y_n = G(\mathbf{x}; \beta) + \delta_n + \epsilon, \quad n = 1, 2, \cdots, N, \tag{2.4}$$

where $\delta_n \sim N(0, \tau^2)$. The use of typical random effects, however, has two deficiencies in characterizing the wake effects. First, it assumes homogeneous turbine-to-turbine variations across weather conditions, i.e., the probabilistic characteristic of δ_n, $n = 1, \cdots, N$, remains the same regardless of the weather condition. The power deficit at a downstream turbine, however, shows a heterogeneous pattern as seen in Figure 2.2, which tends to be large in a mid-wind speed range but vanishes in both low- and high-wind speed ranges. In other words, the distribution of δ_n should depend on the weather condition. Second, it assumes independence among units (turbines in our case), i.e., it assumes δ_n to be independent of $\delta_m, n \neq m$. As such, typical random effects model cannot capture multi-turbine interactions.

To overcome these limitations and address the heterogeneous turbine interactions in a range of weather conditions, our approach is to replace δ_n with $S(\mathbf{x};\gamma_n)$ that depends on weather condition $\mathbf{x}$ and to make $S(\mathbf{x};\gamma_n)$ inter-dependent. Figure 2.2 indicates that the power difference among the two turbines shows a piecewise pattern in general. That is, the power difference is negligible at the low-wind speed range, then increases as wind speed increase up to about 12 m/s. It then decreases and finally diminishes to zero at the high wind-speed range. To flexibly capture such a piecewise pattern, we employ a spline function for $S(\mathbf{x};\gamma_n)$. In particular, similar to the global term, we use a B-spline function as follows:

$$S(\mathbf{x};\gamma_n) = \sum_{k=1}^{K} \mathbf{x}^{s,k}\gamma_n^k, \tag{2.5}$$

where $\mathbf{x}^{s,k}$ is a row vector of the design matrix for the B-spline basis associated with input x^k. Note that $\mathbf{x}^{s,k}$ in $S(\mathbf{x};\gamma_n)$ can differ from $\mathbf{x}^{g,k}$ in (2.3) if different B-spline degrees and knots are used for the global and spatial terms. Parameter γ_n^k is the column vector consisting of corresponding regression parameters. The regression parameter vector γ_n^k is turbine-specific for addressing the turbine-to-turbine variations, whereas the parameter vector β^k in (2.3) for the global term is shared by all turbines.

Next, to capture the spatial dependence caused by the wake effects, we treat the regression parameters in γ_n^k as random effects and make them inter-dependent. One possible way is to model each regression parameter using the GMRF (*Cressie*, 2015). We, however, note that treating each regression parameter as a random effect and individually modeling it with the GMRF is computationally expensive and could lead to an unnecessarily complicated model. Therefore, we introduce a single vector of random effects $\eta^k = [\eta_1^k, \eta_2^k, ..., \eta_N^k]^T$ for each weather factor x^k, and set the regression

parameter vector γ_n^k in (2.5) as $\gamma_n^k = \eta_n^k \cdot \gamma^k$. Then, the spatial term in (2.5) becomes

$$S(\mathbf{x}; \eta_n^{1:K}, \gamma) = \sum_{k=1}^{K} \eta_n^k \mathbf{x}^{s,k} \gamma^k, \tag{2.6}$$

where $\eta_n^{1:K}$ is a set of $\eta_n^1, \eta_n^2, \cdots, \eta_n^K$. With this simplification, the regression parameter vector γ^k becomes the same for every turbine, whereas the variations among individual turbines are captured by η_n^k for each input factor, x^k.

To illustrate how the spatial model in (2.6) can simplify the model in (2.5), suppose that $K = 1$ and the dimension of the row vector $\mathbf{x}^{s,1}$ is 4. With 30 turbines, the model in (2.5) includes $30 \times 4 = 120$ parameters for γ_n^1, and all of the 120 parameters are treated as random effects. Because of the large number of parameters that need to be estimated, our analysis with real data indicates that the resulting estimations are unstable. On the other hand, the simplified model in (2.6) uses 30 parameters for η_n^1 as random effects and 4 fixed parameters for γ^1. Consequently, the model in (2.6) significantly reduces the model complexity. Moreover, this simplification provides useful interpretations that γ^k addresses the heterogeneous power deficits in a range of weather condition, while η_n^k maintains the underlying idea of modeling the turbine-to-turbine variations.

To represent the multi-turbine interactions, we model η_n^k using the GMRF. Specifically, the distribution of η_n^k can be specified by the full conditional probability density function of the Gaussian form,

$$\eta_n^k | \{\eta_m^k : m \in \mathcal{N}(n)\} \sim N\left(\sum_{m \in \mathcal{N}(n)} z_{n,m} \eta_m^k, \tau_k^2 \right), \quad n = 1, 2, ..., N, \tag{2.7}$$

for the k^{th} weather factor. Here, $\mathcal{N}(n)$ denotes the n^{th} turbine's neighborhood turbines, and $z_{n,m}$ captures the dependence intensity between turbine n and turbine m, $n \neq m$. In the spatial modeling literature (*Besag*, 1974), the neighborhood is typi-

cally defined for the regular lattice data. However, the layout of wind farm in reality can be irregular. We will detail how we define the neighborhood turbines later.

Next, we define the dependence intensity $z_{n,m}$ in (2.7). Noting that both wind direction and distances among turbines affect the dependence intensity between two turbines, we use the directional spatial dependence intensity proposed in *Kaiser et al.* (2002),

$$z_{n,m} = \delta_1 \sin^2(\theta_{n,m}) \left(\frac{1}{d_{n,m}}\right)^h + \delta_2 \cos^2(\theta_{n,m}) \left(\frac{1}{d_{n,m}}\right)^h, \tag{2.8}$$

for $n, m = 1 \cdots, N, n \neq m$, where $\theta_{n,m}$ is the angle between the wind direction and the line connecting turbine n and turbine m, and $d_{n,m}$ is the distance between two turbines. The dependence intensity parameter $z_{n,m}$ decomposes the spatial dependence between the two turbines into two components: the first term in (2.8) corresponds to the dependence in the direction orthogonal to the wind direction, and the second term corresponds to the dependence in the wind direction. Figure 2.5 shows the correspondence between these two wind directions. Coefficients δ_1 and δ_2 measure the contributions in each direction. The exponent h scales how quickly the dependence intensity decreases as the distance increases.

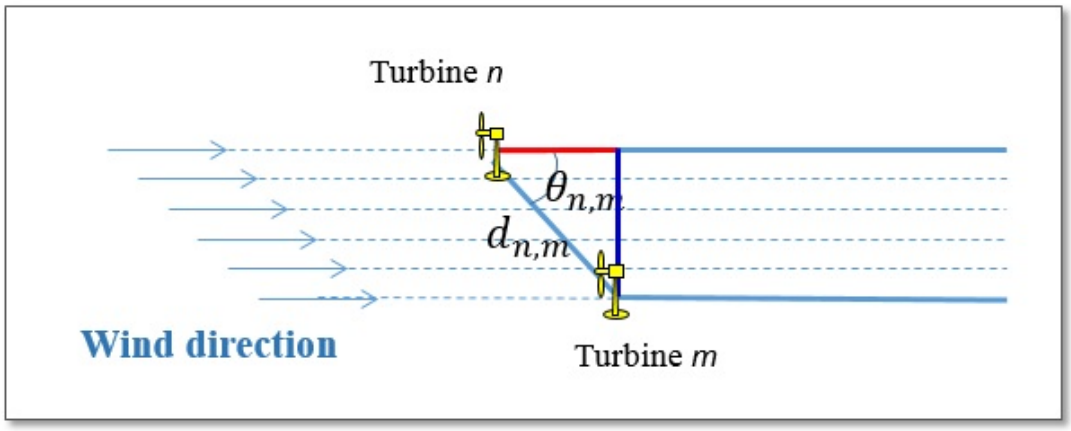

Figure 2.5: Illustration of two directions in the dependence intensity $z_{n,m}$

The full conditional density, specified in (2.7), allows us to obtain the joint density

function of $\boldsymbol{\eta}^k = [\eta_1^k, \eta_2^k, \cdots, \eta_N^k]^T$ as

$$f(\boldsymbol{\eta}^k) = (2\pi)^{-\frac{N}{2}} |Q^k|^{-\frac{1}{2}} \exp\left[-\frac{1}{2}(\boldsymbol{\eta}^k)^T Q^k \boldsymbol{\eta}^k\right], \tag{2.9}$$

where the precision matrix $Q^k = \tau_k^{-2}(\mathbb{1}_N - Z)$ (*Cressie*, 2015). Here, $\mathbb{1}_N$ is an $N \times N$ identity matrix, and Z is an $N \times N$ matrix whose $(n,m)^{th}$ off-diagonal element is $z_{n,m}$ defined in (2.8) and diagonal elements are zero.

For a proper GMRF model, the precision matrix Q^k needs to be symmetric and positive definite. First, the matrix Q^k is symmetric because of $z_{n,m} = z_{m,n}$ in (2.8). Next, Lemma 1 below derives a sufficient condition to ensure the positive definiteness of precision matrix Q^k (see Appendix in Section 2.6.2 for the proof).

Lemma 1: If $\max\{|\delta_1|, |\delta_2|\} < \min\left\{1/\left(\sum_{m=1, m\neq n}^{N} (1/d_{n,m})^h\right), n = 1, \cdots, N\right\}$, the precision matrix Q^k in (2.9) is positive definite.

We use the result of Lemma 1 in defining the prior distributions of δ_1 and δ_2 in the next section. Figure 2.6 summarizes the proposed modeling framework.

2.2.3 Parameter estimations

We estimate the model parameters in a Bayesian hierarchical inference framework. To facilitate computation, we use conjugate priors for some parameters (*Hoff*, 2009). For the regression coefficients in β^k and γ^k in the global and spatial terms, we use the multivariate Gaussian distribution as their priors with zero mean and covariance matrix $\sigma_1^2 \cdot \mathbb{1}$, where $\mathbb{1}$ is the identity matrix with an appropriate dimension. For σ^2 and each τ_k^2 $(k = 1, \cdots, K)$, we use the inverse Gamma distribution with parameters α_0, κ_0, and α_k, κ_k $(k = 1, ..., K)$ as their priors. For δ_1 and δ_2, no conjugate priors are available. Therefore, we use the uniform distribution for their priors. In particular, according to Lemma 1, the uniform distributions are bounded

by $\pm\min\left\{1/\left(\sum_{m=1,m\neq n}^{N}(1/d_{n,m})^h\right), n=1,\cdots,N\right\}$ to ensure that their posteriors are proper. Below we summarize the proposed Bayesian hierarchical framework for wake effects analysis, after recovering the subscript i to denote the i^{th} sample in the dataset.

$$\text{Level 1: } Y_{n,i}|\mathbf{x}_i,\beta^k,\gamma^k,\eta_n^k,\sigma^2 \sim N\left(\sum_{k=1}^{K}\left(\mathbf{x}_i^{g,k}\beta^k+\eta_n^k\mathbf{x}_i^{s,k}\gamma^k\right),\sigma^2\right), \tag{2.10}$$

$$n=1,...,N, i=1,...,I.$$

$$\text{Level 2: } \eta^k \sim MVN\left(0,\tau_k^{-2}(\mathbb{1}-Z)\right), k=1,...,K. \tag{2.11}$$

$$\text{Level 3: } \beta^k \sim MVN(0,\sigma_1^2\cdot\mathbb{1}), k=1,...,K, \tag{2.12}$$

$$\gamma^k \sim MVN(0,\sigma_1^2\cdot\mathbb{1}), k=1,...,K, \tag{2.13}$$

$$\delta_1,\delta_2 \sim \text{uniform}\Big(-\min\left\{1/\left(\sum_{m=1,m\neq n}^{N}(1/d_{n,m})^h\right), n=1,\cdots,N\right\},$$
$$+\min\left\{1/\left(\sum_{m=1,m\neq n}^{N}(1/d_{n,m})^h\right), n=1,\cdots,N\right\}\Big), \tag{2.14}$$

$$\tau_k^2 \sim IG(\alpha_k,\kappa_k), k=1,...,K, \tag{2.15}$$

$$\sigma^2 \sim IG(\alpha_0,\kappa_0). \tag{2.16}$$

Theorem 1 below states that with the hierarchal model structure in (2.10)-(2.16) and the result in Lemma 1, we can obtain a proper posterior density of the model parameters, i.e., the joint posterior density is integrable (see Appendix in Section 2.6.3 for the proof).

Theorem 1: Let θ denote a vector of parameters $\beta^k,\gamma^k,\delta_1,\delta_2,\sigma^2$ and τ_k^2 $(k=1,2,...,K)$. Assume that the prior densities of $\beta^k,\gamma^k,\delta_1,\delta_2,\sigma^2$ and τ_k^2 $(k=1,2,...,K)$ are independent of one another, and the boundary conditions for δ_1 and δ_2 specified in Lemma 1 are satisfied. Then the joint posterior density of θ and η^k $(k=1,...,K)$ is proper.

The posterior density for each parameter involves high-dimensional integrations,

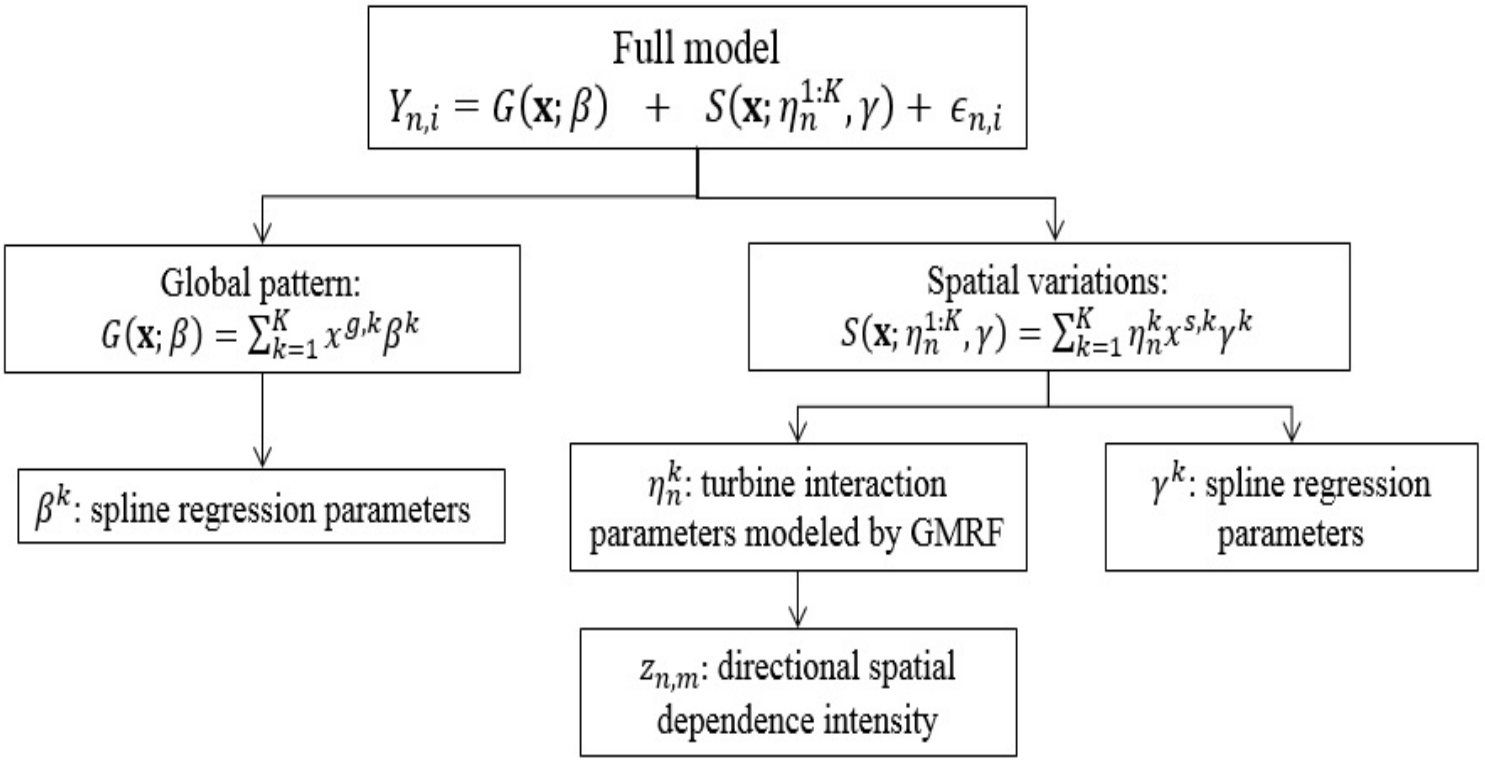

Figure 2.6: The global-spatial modeling framework for wake effects analysis

and it is not expressed as a closed form. As such, we use Markov Chain Monte Carlo (MCMC) methods to obtain the posterior means of the parameters. Given the input covariate vector, we obtain the fitted power at turbine n ($n = 1, \cdots, N$), using

$$\begin{aligned} \hat{Y}_{n,i} &= G(\mathbf{x}_i; \hat{\beta}) + S(\mathbf{x}_i; \hat{\gamma}_n) && (2.17) \\ &= G(\mathbf{x}_i; \hat{\beta}) + S(\mathbf{x}_i; \hat{\eta}_n^{1:K}, \hat{\gamma}) && (2.18) \\ &= \sum_{k=1}^{K} \left(\mathbf{x}_i^{g,k} \hat{\beta}^k + \hat{\eta}_n^k \mathbf{x}_i^{s,k} \hat{\gamma}^k \right), && (2.19) \end{aligned}$$

where $\hat{\beta}^k, \hat{\gamma}^k$ and $\hat{\eta}_n^k$ denote the posterior means of the corresponding parameters.

2.3 Implementation Details

This section discusses the details for implementing the proposed approach. From the original dataset, we extract the data in the dominant wind direction shown in Figure 2.1, when the measurements collected at the met-tower exhibit free-stream wind conditions. The resulting dataset with no missing measurements consists of 300 samples, and each sample includes the power outputs at all turbines in the wind farm and the met-tower's meteorological measurements of weather conditions.

As input factors, we consider the 10-minute average wind speed and the 10-minute average turbulence intensity. We also included other environmental factors such as humidity and air density in our analysis. Figure 2.7 shows the scatter plots between the power productions and four weather factors (wind speed, turbulence intensity, air density, and humidity). As indicated in Figure 2.7, there is no clear correlations between the power and air density and between the power and humidity. In fact, their inclusion did not actually improve the estimation accuracy. The outputs in our model are the 10-minute average power generations at individual turbines in the wind farm. In our implementation, we do not consider the wind travel time across the wind farm because it appears to be insignificant in the mid-size wind farm considered in

this study.

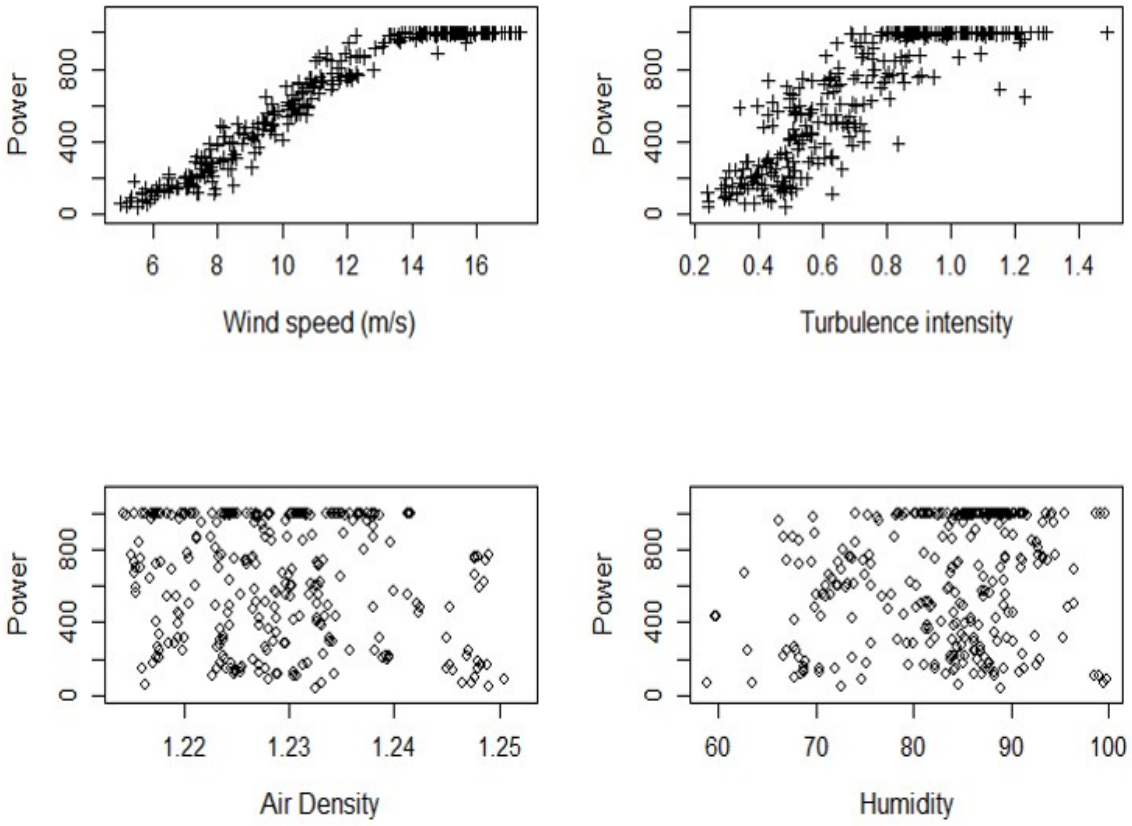

Figure 2.7: Scatter plots of power productions and four wind factors

For each input factor, we use the B-spline functions with different degrees in the global and spatial components. In the global component, to address the nonlinear pattern between the power generation and wind speed shown in Figure 2.2, we consider the B-spline function with degree of 2 or higher for wind speed. For the turbulence intensity, a simpler model appears to be capable of modeling the relationship between power and turbulence intensity. Therefore, we use the B-spline of degree 1 or 2 for the turbulence intensity. For the B-spline functions in the spatial component, the degree equals to, or smaller than, the degree in the global component is considered

in our implementation.

In defining the knots for wind speeds, we note that the wind speeds in the dataset range between 5 m/s and 17.5 m/s. Thus, we choose these two numbers as the boundary knots for the B-splines. In deciding internal knots, we consider that the rated wind speed of the wind turbines in our dataset is 15 m/s. The wind turbines produce a steady power level when wind speed is between 15 m/s and 17.5 m/s. Ideally, our B-splines should capture this piecewise pattern. Therefore, we select 15 m/s as one internal knot. For other internal knots, we use equivalent stepwise distance, which results in the internal knot locations of 7.5 m/s, 10 m/s, 12.5 m/s, and 15 m/s.

Next, in defining the knots for the turbulence intensities, we note that the turbulence intensities in the dataset ranges between 0.2 and 1.5. Thus, we use these two numbers as the boundary knots. In contrast with the rated wind speed, there are no specific numbers for the turbulence intensity available. Thus, we consider two internal knots with equal stepwise distance, i.e., 0.63 and 1.07, which generally capture the piecewise patterns between the turbulence intensity and power generations well. For each input factor, we use the same internal knots in the basis function for both the global and spatial components.

In defining the neighborhood turbines, the first- and second-order neighborhoods are typically considered. In our implementations, we define the neighborhood turbines as follows:

- For wind turbines which are not placed on the wind farm's boundaries, we define the first-order neighborhood turbines as the eight nearest surrounding wind turbines. The second-order neighborhood turbines of a specific turbine are defined as the first-order neighborhood turbines of this turbine's first-order neighborhood turbines.

- For the turbines on the boundary, we use a symmetric property. In other words,

if a turbine, say Turbine D, is a first-order neighborhood turbine to Turbine C, Turbine C becomes the first-order neighborhood turbine to Turbine D (See Figure 2.8). In addition, to define neighborhood turbines among turbines on the boundary, we set a threshold distance such that the turbines within the threshold distance become neighbors. In our implementation, the threshold is defined based on the wind farm size and the average distance among the neighborhood turbines within the boundary.

We consider both first- and second-order neighborhood turbines in our study. However, our preliminary analysis that used a second-order neighborhood did not improve the estimation performance. As such, we present the results using the first-order neighborhood for specifying $\mathcal{N}(n)$ in (2.7) over the use of the second-order neighborhood. We use 0.5 for h in defining the dependency intensity in (2.8) (Section 2.4 includes a sensitivity study with different values of h).

In the MCMC implementations, we do not assume any prior knowledge, and attempt to use non-informative priors. We set σ_1 in (2.12) and (2.13) to be 1000 to ensure a sufficiently large coverage for β^k and γ^k. To specify the parameters in the inverse Gamma priors in (2.15) and (2.16), we employ non-informative priors by using the same shape and scale parameters (*Gelman*, 2006). Specifically, we use $\alpha_k = \kappa_k = 0.1$ $(k = 0, 1, ..., K)$ (*Banerjee et al.*, 2014). The MCMC is conducted by calling the WinBUGS software from R using the function *bugs()* from the library "R2WinBUGS" (*Sturtz et al.*, 2005). We run the simulation for 10000 iterations with first 5000 iterations as burn-in iterations.

We employ a ten-fold cross validation (CV) to evaluate the estimation accuracy of the proposed approach, using three criteria: the root mean square error (RMSE),

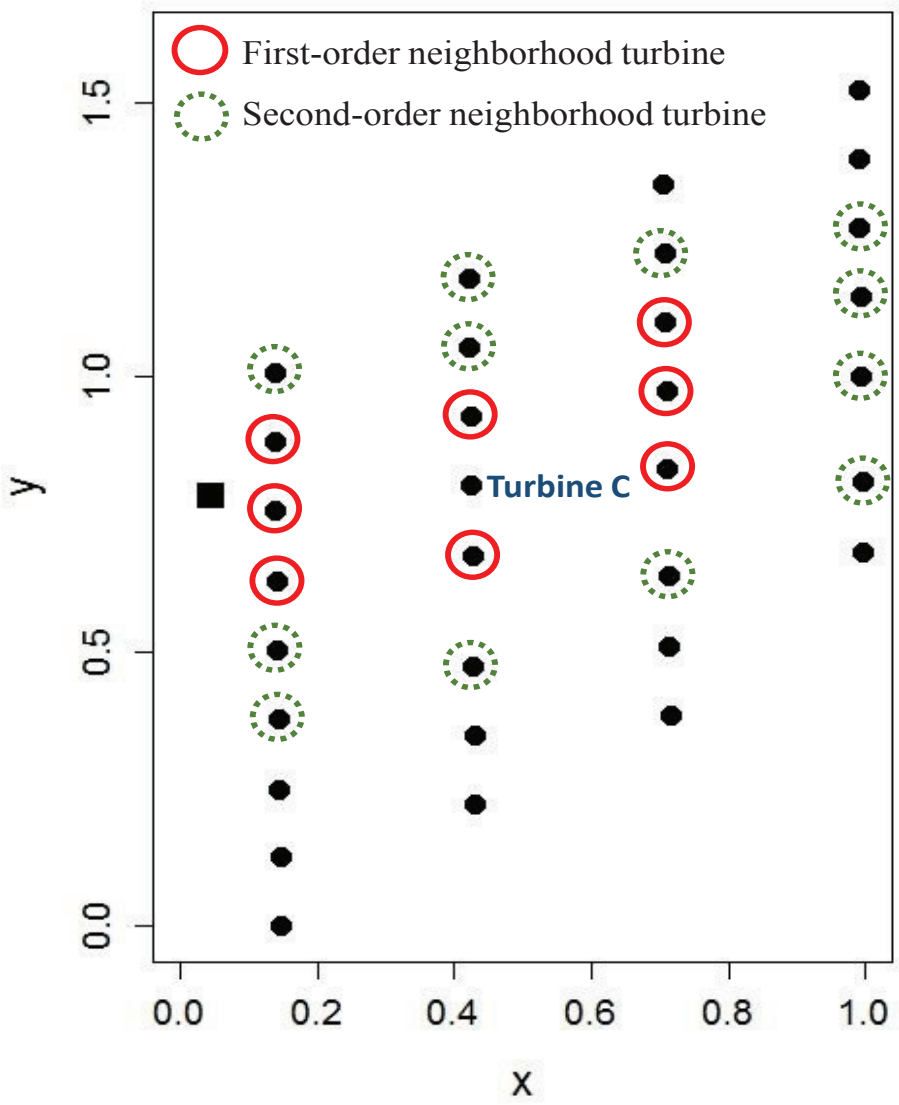

Figure 2.8: Illustrations of the first- and second-order neighborhood turbines of Turbine C

and the mean absolute error (MAE) defined as

$$RMSE = \sqrt{\frac{\sum_{n=1}^{N}\sum_{i=1}^{I_0}(Y_{n,i}-\hat{Y}_{n,i})^2}{N\cdot I_0}} \tag{2.20}$$

$$MAE = \frac{\sum_{n=1}^{N}\sum_{i=1}^{I_0}|Y_{n,i}-\hat{Y}_{n,i}|}{N\cdot I_0} \tag{2.21}$$

where I_0 is the size of a testing set, and $Y_{n,i}$ and $\hat{Y}_{n,i}$ are the actual and estimated power generation at the n^{th} turbine and the i^{th} sample in the testing set, respectively. Recall that in our implementation, the power generation is re-scaled to 0-1000 to retain the confidentiality of data source.

2.4 Case Study

This section discusses the computational results of the proposed model. We also compare its estimation accuracy with other alternative methods.

2.4.1 Computational results

We implement the proposed model with different B-spline degrees in both global and spatial terms. Table 2.1 summarizes the estimation results of eight models in terms of the average RMSE and MAE of ten testing sets in the 10-fold CV, and their standard deviations. The shorthand names in the first column of Table 2.1 specify the input covariates included in the model and the degrees of the spline functions in the global and spatial components. For example, G(W2T1)S(W2T1) refers to the model using the B-splines of degrees 2 and 1 for wind speed and turbulence intensity, respectively, in both global pattern $G(\cdot)$ and spatial component $S(\cdot)$. The first three models in Table 2.1, namely, G(W2)S(W1), G(W3)S(W1) and G(W3)S(W2), do not include the turbulence intensity as an input factor.

The comparisons between the first three models and other models in Table 2.1

suggest that including turbulence intensity in the input vector slightly improves the estimation accuracy. However, the fitting errors from different models are within one standard deviation, and no model significantly outperforms others. Therefore, we believe that any models would be acceptable. Overall, the model G(W2T1)S(W2T1) provides the smallest average errors in the testing sets, so we use it in subsequent discussions.

Table 2.1: Average and standard deviation of RMSE, and MAE from 10-fold CV (unit: normalized power in [0, 1000] KW)

Model	RMSE	MAE
G(W2)S(W1)	58.46 (6.86)	39.31 (4.77)
G(W3)S(W1)	58.45 (6.74)	39.54 (4.81)
G(W3)S(W2)	60.53 (8.29)	41.06 (5.50)
G(W2T1)S(W1)	57.12 (5.72)	39.26 (4.22)
G(W2T1)S(W2)	56.95 (5.86)	39.29 (4.33)
G(W2T1)S(W1T1)	57.15 (5.72)	39.15 (4.37)
G(W2T1)S(W2T1)	**56.68** (5.83)	**38.62** (4.44)
G(W2T2)S(W1T1)	57.10 (5.29)	38.92 (4.12)

Note: Each number in parentheses is the standard deviation of RMSEs, and MAEs from 10 testing sets.

Figure 2.9 depicts the fitted results at Turbine A and B using model G(W2T1)S(W2T1). As a remark, multiple estimations are made at the same wind speed in the figure due to the different values of turbulence intensity. In general, the estimated power at Turbine B at the downwind location is smaller than that of Turbine A at the upwind location, which is consistent with our observations. Moreover, the model can capture the heterogeneous power deficits at the downstream turbine; the difference of estimated power outputs between the two turbines (or the power deficit at Turbine B) increases as wind speed increases, but as the wind speed nears $14 \sim 15$ m/s, the difference becomes smaller.

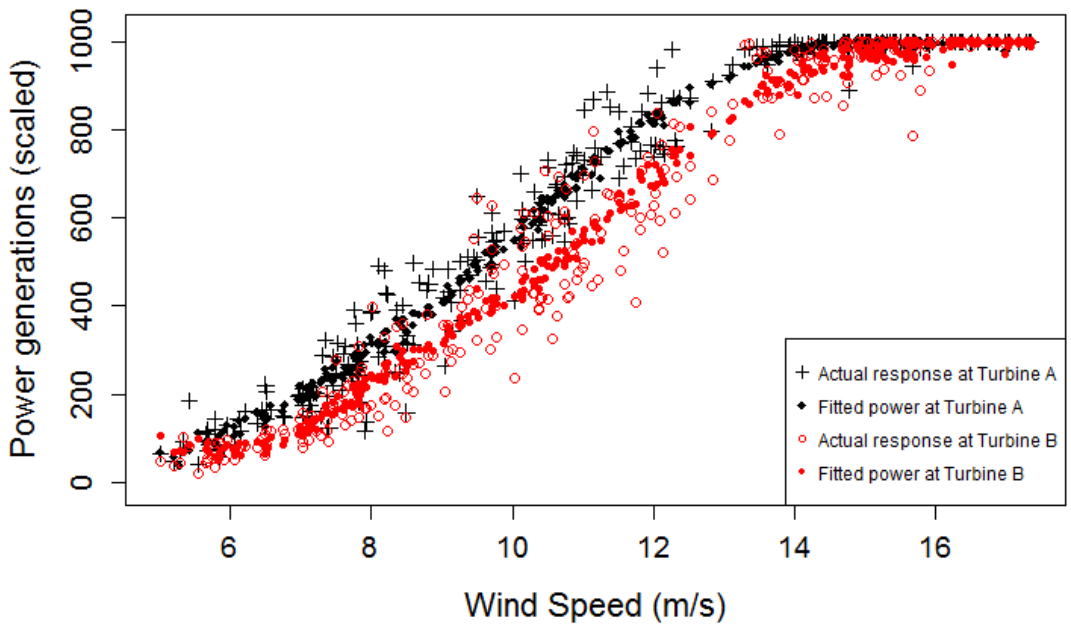

Figure 2.9: Fitted power at Turbines A and B using model G(W2T1)S(W2T1)

2.4.2 Sensitivity analysis

This section describes a sensitivity study for the exponent parameter h in (2.8) in defining the dependence intensity. Table 2.2 shows the results with different values for h in model G(W2T1)S(W2T1) and reports the average RMSE, and MAE of the ten testing sets. We note that the estimation results are not sensitive to the choice of the parameter h. Therefore, we keep using $h = 0.5$ in our subsequent analysis.

Table 2.2: Sensitivity analysis on h with model G(W2T1)S(W2T1)

	$h = 0.2$	$h = 0.5$	$h = 1$	$h = 1.5$	$h = 2$
RMSE	56.71	56.68	56.87	56.55	56.79
MAE	38.73	38.62	38.55	38.86	38.67

2.4.3 Comparison with alternative methods

We compare the estimation capability of the proposed modeling approach with other alternative models, including a physics-based engineering model and statistical models. The first model we consider is Jensen's model (*Jensen*, 1983; *Katic et al.*, 1986), one of the most widely used physics-based engineering models in the global wind industry. Jensen's model analytically predicts the incoming wind speed at each turbine as follows.

$$(Jensen): \quad V_{down} = (1 - \kappa_{deficit})V_{up}, \tag{2.22}$$

where V_{up} and V_{down} are the incoming wind speeds at an upstream turbine and a downstream turbine, respectively, and $\kappa_{deficit}$ is a wind speed deficit factor at a downstream turbine. Jensen's model in (2.22) specifies the relationship between two turbines. We use the extended version of Jensen's model that incorporates multiple wake interactions discussed in *Jensen* (1983). The value of $\kappa_{deficit}$ depends on a wake effect decay parameter and other wind farm-specific factors such as a distance between turbines and a rotor diameter. We use the wake effect decay parameter of 0.075 as suggested in *Katic et al.* (1986), *DTU Wind Energy* (2015), and *Staid* (2015).

Note that Jensen's model does not estimate the power generations because it focuses on estimating the incoming wind conditions at multiple turbines. Because our turbines have the same specification (i.e., same turbine model from the same manufacturer), we assume similar power generation patterns, given the same incoming wind speed at each turbine. Then, we construct a power curve for one of the upstream turbines (Turbine A in Figure 2.1) which is not in the wake region, and apply the resulting power curve to other turbines.

We also consider other statistical models. The first and simplest model contains

only the global component,

$$(GLB): \quad Y_n = \sum_{k=1}^{K} \mathbf{x}^k \beta^k + \epsilon, \quad n = 1, 2, ..., N, \tag{2.23}$$

where $\mathbf{x}^k$ is a row vector of design matrix of the B-spline basis with the k^{th} weather factor x^k measured at the met-tower. The spline regression parameter vector β^k is the same for all wind turbines, implying that the same regression function is used for all turbines.

The second statistical model individually fits the spline regression for each turbine as

$$(IND): \quad Y_n = \sum_{k=1}^{K} \mathbf{x}^k \beta_n^k + \epsilon, \quad n = 1, 2, ..., N, \tag{2.24}$$

where β_n^k differs for individual turbines, and the model separately builds a regression function using the data from each turbine. This model generates N (i.e., the number of turbines in a wind farm) regression functions.

The third statistical model uses the typical random effects, δ_n,

$$(RND): \quad Y_n = \sum_{k=1}^{K} \mathbf{x}^k \beta^k + \delta_n + \epsilon, \quad n = 1, 2, ..., N, \tag{2.25}$$

where $\delta_n \sim N(0, \tau^2)$. All turbines share the same spline regression parameters β^k as in GLB, but δ_n represents the turbine-to-turbine variability. This model assumes independence among δ_n, $n = 1, \cdots, N$.

Because the model G(W2T1)S(W2T1) provides the best estimation results in Section 2.4.1, we use the B-spline functions of degrees 2 and 1 for wind speed and turbulence intensity, respectively, in these three statistical models, and estimate their parameters using MCMC. Table 2.3 summarizes the comparison results. The model names in rows 4, 5, and 6 of the first column can be interpreted as in Table 2.1. We

summarize our observations as follows:

- Among all methods, the proposed modeling approach, G(W2T1)S(W2T1), produces the smallest estimation errors in terms of the three criteria. We also observe that overall, statistical models outperform Jensen's model. In particular, the estimation errors in Jensen's model are about double those in the statistical-based approaches.

- Understandably, the simplest model, GLB(W2T1), generates the highest estimation errors among the four statistical models because it does not account for the turbine-to-turbine variations.

- Even though the differences between our approach and other statistical models, IND and RND, are not significant in terms of the fitting errors, our model provides better interpretations in practical applications:

  - The model with the random effects, RND(W2T1), captures the variations among turbines, but it assumes the homogeneous power deficits across the weather conditions and the independence among the turbines.

  - The result from the individual model, IND(W2T1), is difficult to be used for understanding the multi-turbine dependencies because it presents a local modeling approach that individually analyzes the data from each turbine. Therefore, the IND model does not provide wind farm-level insights. On the contrary, the proposed model captures the interactions among turbines in an integrative manner, while preserving a strong fitting capability. This feature of our proposed model is critical for wind farm-level problems such as wind farm design and control optimization.

To further illustrate the major difference between the proposed approach and RND, Figure 2.10 shows the fitted power curves for the two turbines, Turbines A

Table 2.3: Performance comparison (unit: normalized power in [0, 1000] KW)

Model	RMSE	MAE
Jensen's model	124.18	92.09
G(W2T1)S(W2T1)	**56.68** (5.83)	**38.62** (4.44)
GLB(W2T1)	65.01 (6.24)	45.34 (4.97)
IND(W2T1)	56.91 (5.81)	39.07 (4.31)
RND(W2T1)	59.52 (5.98)	43.26 (4.10)

Note: Numbers inside the parentheses are the standard deviations of fitting errors from the ten testing sets. In Jensen's model, cross validation is not employed and the numbers are obtained from the fitting results in 300 samples.

and B, using RND with degree 2, RND(W2). Here, we exclude the turbulence intensity from the input vector and only include the wind speed as a covariate to see the limitation of RND more clearly. Figure 2.10 shows that the fitted curves for the two turbines are parallel, implying that the difference in the fitted power outputs is same across wind conditions. These results do not agree with actual power generation patterns, showing that RND cannot successfully capture the heterogeneous wake interactions among turbines.

2.4.4 Quantification of turbine-to-turbine variability

This section quantifies the variations of power generations at multiple turbines. We compute the power deficit at the n^{th} turbine of the i^{th} sample as

$$\hat{D}_{n,i} = \max_{m=1,\cdots,N} \hat{P}_{m,i} - \hat{P}_{n,i}. \tag{2.26}$$

That is, the power deficit at the the n^{th} turbine represents the difference between its estimated power output and the maximum estimated output among N turbines.

To illustrate, we consider the wind speed as the only input weather factor, and draw the box plots of power deficits at multiple wind speeds from 5 m/s to 16 m/s with a stepwise of 1 m/s as shown in Figure 2.11. Each box plot shows the minimum, first quartile, median, third quartile, and maximum power deficits at each wind speed.

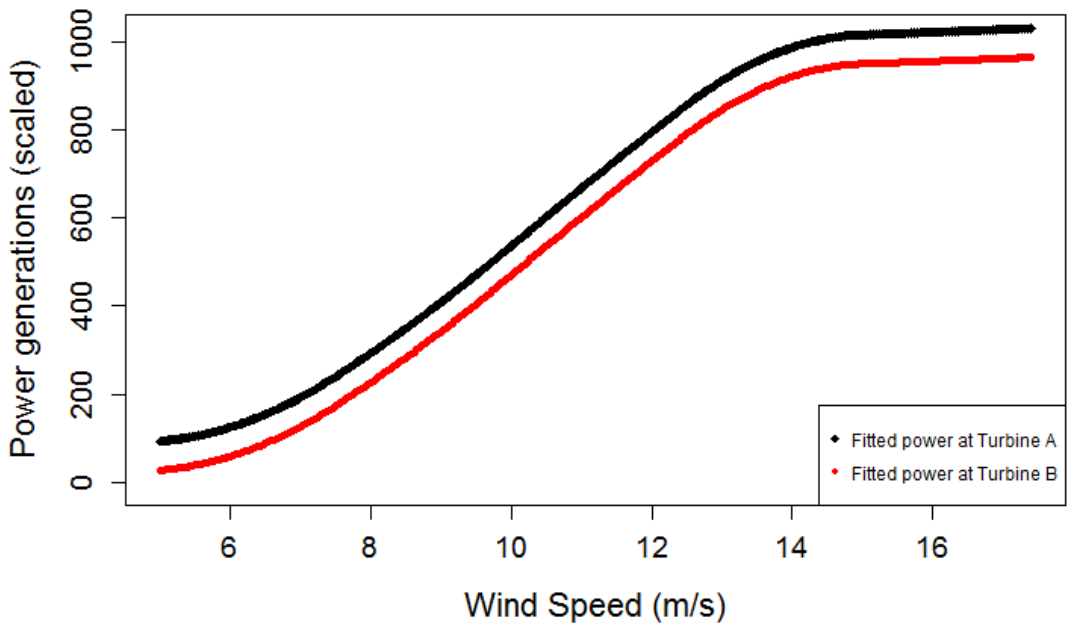

Figure 2.10: Estimated power curves for Turbines A and B using model RND(W2)

Figure 2.11 shows that the range of power deficits increases when the wind speed increases up to 12 m/s. This implies that the turbine-to-turbine variability increases as the wind speed increases. When wind speed is 12 m/s, the power deficit ranges from 0 to 184. Considering that the estimated power generation at Turbine A (the upstream turbine) is about 793, a turbine downstream generates 23% ($= 184/793 \times 100\%$) less power than Turbine A. When the wind speed is over 12 m/s, the turbine-to-turbine variability becomes smaller.

Overall, these results present good agreements with the observed data on the heterogeneous variability of power outputs. The results also indicate that controlling the power generation level at upstream turbines to absorb less energy from the wind can possibly increase the power generations at downstream turbines, thus optimizing overall performance at a wind farm level (*Annoni et al.*, 2014).

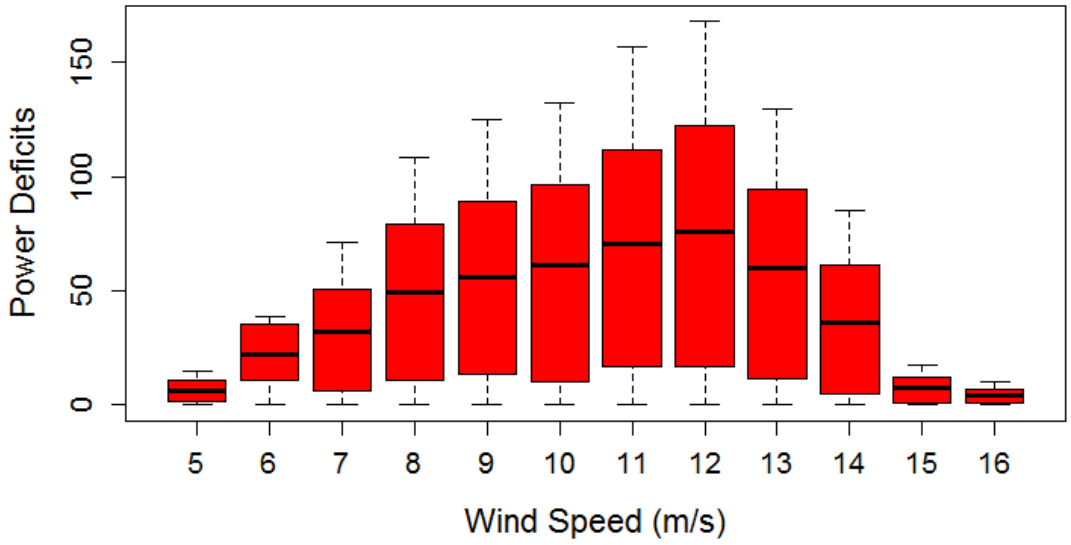

Figure 2.11: Box plots of estimated power deficits in multiple turbines using G(W2)S(W1)

2.5 Summary

A new approach is proposed for understanding the effects of unobserved wake effects on the heterogeneous power generations of multiple turbines under the dominant wind direction. The approach decomposes the power outputs into global and spatial components, respectively, to model the average pattern globally shared by all turbines and the turbine-specific variations. In representing the global pattern, B-splines are used to address the nonlinear relationship between power and weather conditions. For the spatial variations, we also use the B-spline functions where the spline regression parameters are modeled through GMRF to capture the interactions among neighboring turbines. A case study using actual data from a multi-turbine wind farm suggests that the proposed statistical approach successfully characterizes the heterogeneous wake effects, compared with other alternative methods.

2.6 Appendix for Chapter II

2.6.1 Description of B-spline basis and design matrix

For each weather factor x, suppose its domain is $[x_{min}, x_{max}]$. With a pre-specified degree D, let $x_{min} = \kappa_1 = \kappa_2 = ... = \kappa_d < \kappa_{d+1} < ... < \kappa_{T-d} = \kappa_{T-d+1} = ... = \kappa_T = x_{max}$ denote a non-decreasing sequence of the knots in the domain, where T is the total number of knots including the boundary knots. The B-spline basis can be defined recursively as (*Friedman et al.*, 2009)

$$b_{0,l}(x) = \begin{cases} 1, & \kappa_l \leq x < \kappa_{l+1} \\ 0, & \text{otherwise} \end{cases}, \tag{2.27}$$

and for $1 \leq d \leq D$,

$$b_{d,l}(x) = \frac{x - \kappa_l}{\kappa_{l+d-1} - \kappa_l} b_{d-1,l}(x) + \frac{\kappa_{l+d} - x}{\kappa_{l+d} - \kappa_{l+1}} b_{d-1,l+1}(x). \tag{2.28}$$

Then, the row of the design matrix with input x becomes $[b_{D,1}(x), b_{D,2}(x), ..., b_{D,T}(x)]^T$. In our modeling, for the k^{th} input factor x^k with the degree D^k and the total number of knot T^k, $\mathbf{x}^{g,k}$ in (2.3) becomes $\mathbf{x}^{g,k} = [b_{D^k,1}(x^k), b_{D^k,2}(x^k), ..., b_{D^k,T^k}(x^k)]^T$. Similarly, $\mathbf{x}^{s,k}$ in (2.5) can be defined.

2.6.2 Proof of Lemma 1

Lemma 1: If $\max\{|\delta_1|, |\delta_2|\} < \min\left\{1/\left(\sum_{m=1,m\neq n}^{N} (1/d_{n,m})^h\right), n = 1, \cdots, N\right\}$, the precision matrix Q^k in (2.9) is positive definite.

Proof. It suffices to show the positive definiteness of $\mathbb{1}_N - Z$. Suppose the condition $max\{|\delta_1|, |\delta_2|\} < min\left\{1/\left(\sum_{m=1,m\neq n}^{N} (1/d_{n,m})^h\right), n = 1, 2, \cdots, N\right\}$ holds. Then, for

$\forall n = 1, 2, ..., N,$

$$
\begin{aligned}
1 > & \quad max\{|\delta_1|, |\delta_2|\} \sum_{m=1, m\neq n}^{N} \left(\frac{1}{d_{n,m}}\right)^h && (2.29)\\
= & \quad \sum_{m=1, m\neq n}^{N} max\{|\delta_1|, |\delta_2|\} \left(\sin^2(\theta_{n,m}) \left(\frac{1}{d_{n,m}}\right)^h + \cos^2(\theta_{n,m}) \left(\frac{1}{d_{n,m}}\right)^h\right) && (2.30)\\
\geq & \quad \sum_{m=1, m\neq n}^{N} \left(|\delta_1| \sin^2(\theta_{n,m}) \left(\frac{1}{d_{n,m}}\right)^h + |\delta_2| \cos^2(\theta_{n,m}) \left(\frac{1}{d_{n,m}}\right)^h\right) && (2.31)\\
\geq & \quad \sum_{m=1, m\neq n}^{N} \left(\left|\delta_1 \sin^2(\theta_{n,m}) \left(\frac{1}{d_{n,m}}\right)^h + \delta_2 \cos^2(\theta_{n,m}) \left(\frac{1}{d_{n,m}}\right)^h\right|\right) && (2.32)\\
= & \quad \sum_{m=1, m\neq n}^{N} |z_{n,m}| && (2.33)
\end{aligned}
$$

As a result, $\sum_{m=1, m\neq n}^{N} |z_{n,m}| < 1, \forall n$. Note that the diagonal elements of $\mathbb{1}_N - Z$ are 1. Consequently, the matrix $\mathbb{1}_N - Z$ is diagonally dominant. This concludes that $\mathbb{1}_N - Z$ is positive definite under the condition (*Ortega*, 1987):

$$
max\{|\delta_1|, |\delta_2|\} < min\left\{1/\left(\sum_{m=1, m\neq n}^{N} (1/d_{n,m})^h\right), n = 1, 2, \cdots, N\right\}.
$$

□

2.6.3 Proof of Theorem 1

Theorem 1: Let θ denote a vector of parameters $\beta^k, \gamma^k, \delta_1, \delta_2, \sigma^2$ and τ_k^2 $(k = 1, 2, ..., K)$. Assume that the prior densities of $\beta^k, \gamma^k, \delta_1, \delta_2, \sigma^2$ and τ_k^2 $(k = 1, 2, ..., K)$ are independent of one another, and the boundary conditions for δ_1 and δ_2 specified in Lemma 1 are satisfied. Then the joint posterior density of θ and η^k $(k = 1, ..., K)$ is proper.

Proof. For notational simplicity, we consider $K = 1$ and omit the subscript and superscript "k" in the following proof. The extension to the case with $K > 1$ is straightforward due to the independence assumption among the parameters in θ in their priors. We use $p(\cdot)$ to denote the prior distribution, and $L(\cdot)$ to denote the

likelihood function. Y and X denote the response vector and covariate matrix, respectively.

The joint posterior density satisfies:

$$\begin{aligned} f(\theta,\eta|Y,X) &\propto L(Y|X,\theta,\eta)p(\eta|\theta)p(\theta) && (2.34)\\ &\propto L(Y|X,\theta,\eta)p(\eta|\tau^2,\delta_1,\delta_2)p(\delta_1)p(\delta_2)p(\sigma^2)p(\tau^2)p(\beta)p(\gamma). && (2.35)\end{aligned}$$

To show the posterior is proper, the integration of the righthand side in (2.35) should be finite. First, in the likelihood, we get

$$\begin{aligned} L(Y|X,\theta,\eta) &= (2\pi\sigma^2)^{-NI/2}\exp\left\{-\frac{1}{2\sigma^2}\sum_{n,i}[Y_{n,i}-(x_i^g\beta+\eta_n x_i^s\gamma)]^2\right\} && (2.36)\\ &\leq (\sigma^2)^{-NI/2}, && (2.37)\end{aligned}$$

where the inequality in (2.37) holds due to the fact that $[Y_{n,i}-(x_i^g\beta+\eta_n x_i^s\gamma)]^2\geq 0$.

Therefore, it suffices to show that the integration of the following term is finite, i.e.,

$$\int_{\theta,\eta}(\sigma^2)^{-NI/2}p(\eta|\tau^2,\delta_1,\delta_2)p(\delta_1)p(\delta_2)p(\sigma^2)p(\tau^2)p(\beta)p(\gamma)d\eta d\theta<\infty. \quad (2.38)$$

Due to the independence assumption in priors, we have

$$\begin{aligned} &\int_{\theta,\eta}(\sigma^2)^{-NI/2}p(\eta|\tau^2,\delta_1,\delta_2)p(\delta_1)p(\delta_2)p(\sigma^2)p(\tau^2)p(\beta)p(\gamma)d\eta d\theta && (2.39)\\ =\ &\left[\int_{\eta,\tau^2,\delta_1,\delta_2}p(\eta|\tau^2,\delta_1,\delta_2)p(\delta_1)p(\delta_2)p(\tau^2)d\eta d\tau^2 d\delta_1 d\delta_2\right]\\ &\cdot\left[\int_\beta p(\beta)d\beta\right]\cdot\left[\int_\gamma p(\gamma)d\gamma\right]\cdot\left[\int_\sigma(\sigma^2)^{-NI/2}p(\sigma^2)d\sigma\right]. && (2.40)\end{aligned}$$

Note that priors of β and γ are multivariate normal, so we have $\int_\beta p(\beta)d\beta=1$ and

$\int_\gamma p(\gamma)d\gamma = 1$. For σ^2, we use the inverse gamma distribution as its prior with parameters α_0 and κ_0. Then, we have

$$(\sigma^2)^{-NI/2}p(\sigma^2) \propto (\sigma^2)^{-NI/2-\alpha_0-1}\exp\left\{-\frac{\kappa_0}{\sigma^2}\right\}, \tag{2.41}$$

which is proportional to the density of the inverse Gamma distribution with parameters $NI/2+\alpha_0$ and κ_0. Therefore, the integration $\int_\sigma (\sigma^2)^{-NI/2}p(\sigma^2)d\sigma$ is finite.

Lastly, the first term in (2.40) becomes

$$\int_{\eta,\tau^2,\delta_1,\delta_2} p(\eta|\tau^2,\delta_1,\delta_2)p(\delta_1)p(\delta_2)p(\tau^2)d\eta d\tau^2 d\delta_1 d\delta_2 \tag{2.42}$$

$$= \int_{\delta_1,\delta_2}\left(\int_{\tau^2}\left(\int_\eta p(\eta|\tau^2,\delta_1,\delta_2)d\eta\right)p(\tau^2)d\tau^2\right)d\delta_1 d\delta_2. \tag{2.43}$$

When δ_1 and δ_2 satisfy the boundary condition specified in Lemma 1, η is a valid multivariate Gaussian random variable. Thus, we have $\int_\eta p(\eta|\tau^2,\delta_1,\delta_2)d\eta = 1$. Moreover, with the inverse Gamma distribution as a prior of τ^2, we $\int_{\tau^2} p(\tau^2)d\tau^2 = 1$. Finally, when we integrate δ_1 and δ_2 over a bounded set specified in Lemma 1, $\int_{\delta_1,\delta_2} d\delta_1 d\delta_2$ becomes finite, which shows that the joint posterior density is proper.

□

CHAPTER III

Direction-dependent Power Curve Modeling for Multiple Interacting Wind Turbines

3.1 Introduction

In Chapter II, we study that turbines in the downwind directions are impacted by wind deficits, producing less power, compared to upstream turbines. The proposed model in Chapter II is validated by only using the data collected under the dominant wind direction when the met-tower measures the free-flow wind conditions.

This chapter extends the model proposed in Chapter II to account for wake effects in different wind directions by using the data measured at the met-tower and data collected at turbine anemometers. Therefore, this chapter provides an integrative framework that quantifies the power generation performance of multiple interacting turbines in all wind directions.

To demonstrate the influence of wind directions on power generations in multiple turbines, we consider the partial layout of the wind farm used in Chapter II (Figure 3.1 (a)). When wind blows from left to right, turbines in the leftmost column, T1 through T9, are upstream turbines. When wind direction changes, the wake correlations change accordingly and some of these turbines become downstream turbines.

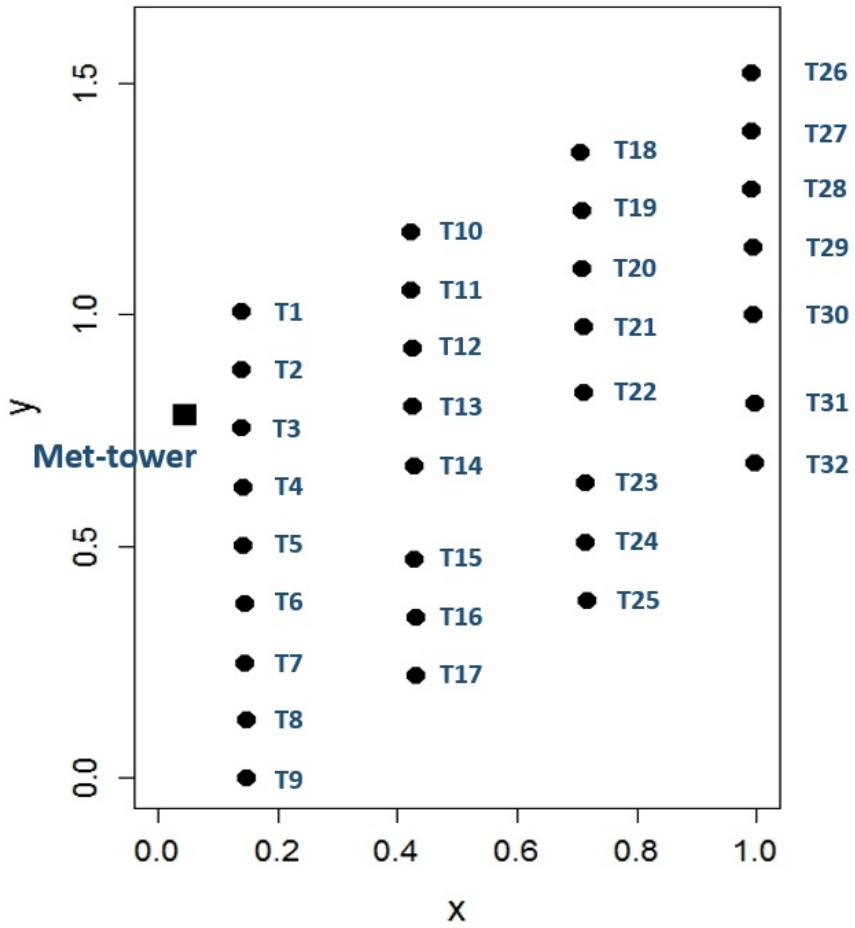

(a) Partial layout of a wind farm

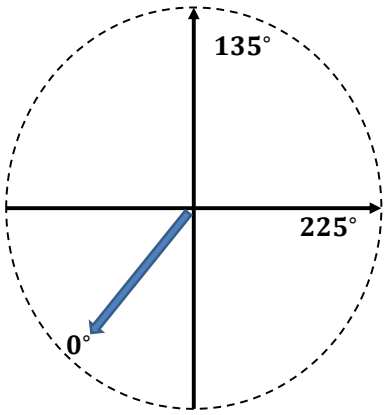

(b) Wind direction

Figure 3.1: Wind farm information (note: Tn denotes the *nth* turbine.)

Figure 3.2 shows the average power generations of the multiple turbines in Figure 3.1 under two different directions when the free-flow wind speed is between 11.9 and 12.1 m/s. We normalize the power generation level in 0-1000 scale. Each circle and '+' represent the average power from turbines whose indexes are shown in the x-axis. As wind flows through turbines, the power outputs decrease. Specifically, the turbines in the rightmost column, T26 through T32, generate the least amount of power when the direction is 225°. We observe the opposite pattern under 45°.

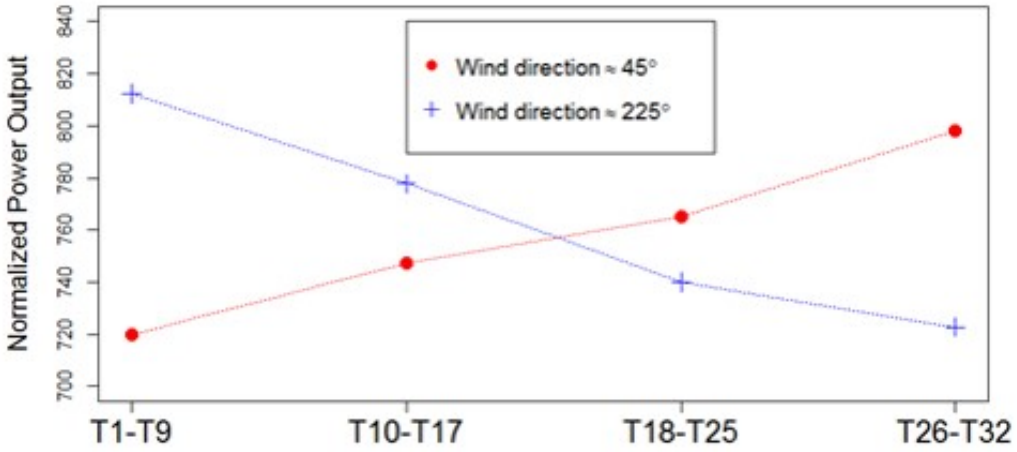

Figure 3.2: Normalized average power generations from turbines under two different directions with the free-flow speed between 11.9 m/s and 12.1 m/s

Figure 3.3 shows the power outputs from T8 and T32, where the x-axis and y-axis are the 10-minute average wind speed and normalized 10-minute average power output, respectively. In general, turbines generate more power as the wind speed increases from the cut-in speed of 4 m/s to the rated speed of about 15 m/s in our data set. Above the rated speed, their generation levels become steady due to the control algorithm to regulate power generation at high wind speeds. Despite the common trend exhibited by the two turbines, T8 tends to output less power when wind direction is between 40° and 50° (Figure 3.3(a)), but this pattern changes under 220° $\sim$ 230° (Figure 3.3(b)). As a result, the power curves for individual turbines should differ, depending on the wind direction.

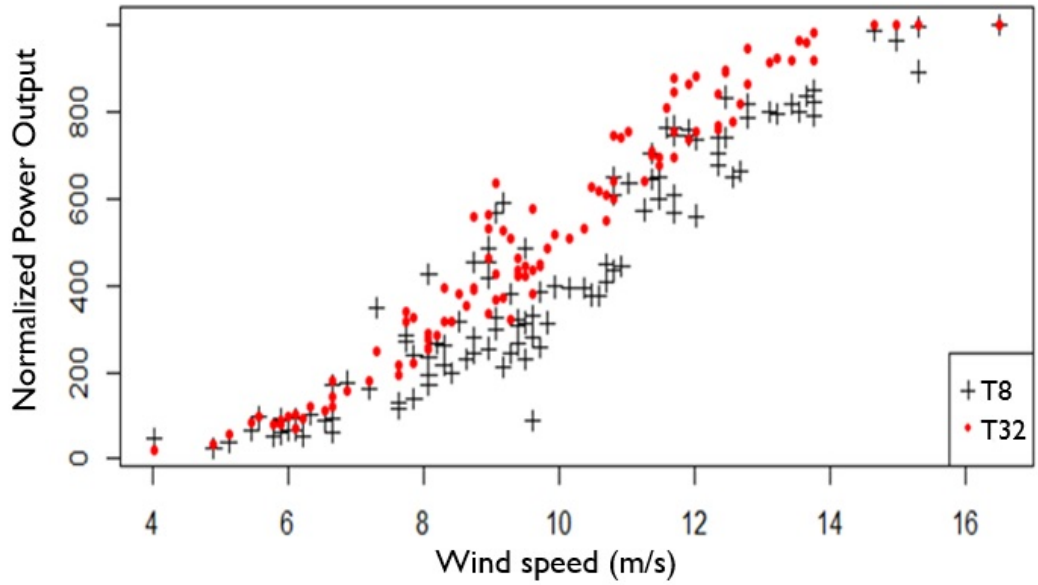

(a) When the wind direction is between 40° and 50°

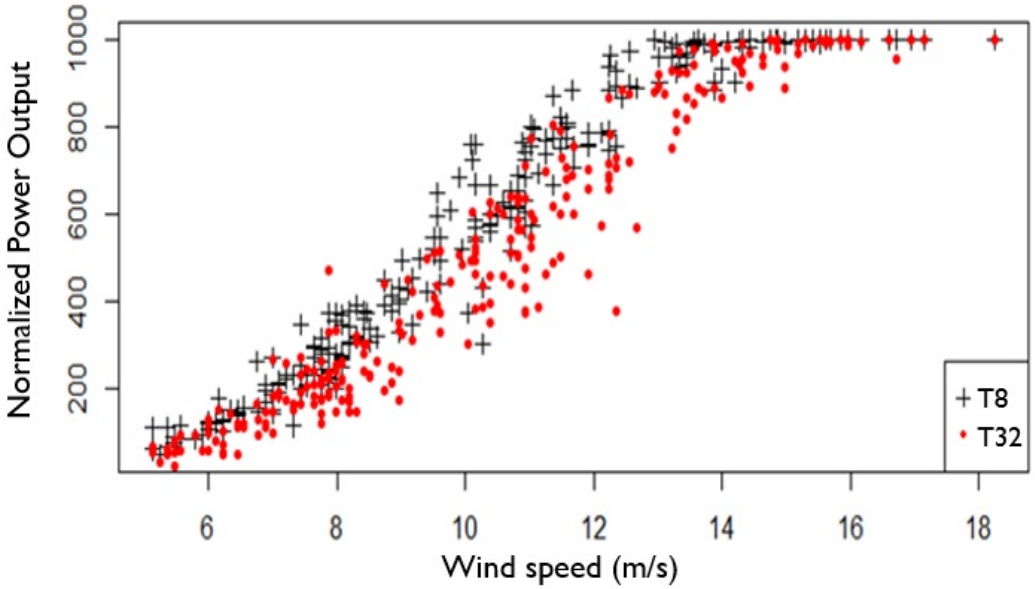

(b) When the wind direction is between 220° and 230°

Figure 3.3: Heterogeneous power generation patterns of T8 and T32 under two different wind directions

3.2 Methodology

3.2.1 Modeling multi-turbine power curves under wake effects

We use data obtained from a real wind farm's supervisory control and data acquisition (SCADA) system (*Zaher et al.*, 2009; *Yampikulsakul et al.*, 2014). In a typical wind farm, the SCADA system collects 10-minute average data. We use notations similar to those in Chapter II. Let $Y_{n,i}$ denote the 10-minute average power generation output of the n^{th} turbine ($n = 1, 2, \cdots, N$) at the i^{th} sample ($i = 1, 2, \cdots, I$) in the data set, where i denotes the time index at which the data sample is collected.

As seen in Figure 3.3, turbines exhibit similar patterns, regardless of wind directions. We refer to such a common pattern as a global pattern. Depending on the locations of turbines and wind directions, however, some turbines generate more (or less) power than that of the global pattern. We refer to such variations as spatial variations. Considering both the global pattern and spatial variations, we formulate the power curve at each turbine in a similar form proposed in Chapter II as follows:

$$Y_{n,i} = G(x_i; \beta) + S(x_i, d_i; \eta_n, \gamma) + \epsilon_{n,i}, \tag{3.1}$$

for $n = 1, \cdots, N$ and $i = 1, \cdots, I$, where x_i and d_i denote the 10-minute average free-flow wind speed and direction at the i^{th} sample, respectively. It should be noted that the same free-flow wind speed x_i is used as an input covariate for all turbines. Components $G(\cdot)$ and $S(\cdot)$ represent the global pattern and spatial variations, respectively, with β and γ denoting the regression parameters, and η_n denoting a turbine-specific random effect which captures the turbine-to-turbine variations. Parameters β, γ and η_n need to be learned from the data (the specific meaning of these parameters and their estimation procedure will be detailed in subsequent discussions). The white noise $\epsilon_{n,i}$ is assumed to be an independent Gaussian random variable with the mean 0 and variance σ^2.

Different from Chapter II, we do not include the turbulence intensity in (3.1), because the free-flow turbulence intensity measurements are only available when the met-tower is not under wake. For example, in the easterly direction, the turbulence intensity collected in the met-mast does not represent the free-flow measurement. For the wind speed, we use the nacelle transfer function (NTF) to estimate the free-flow wind speeds in all directions (*Curvers and Van der Werff*, 2008). The details of using the NTF function in implementations will be discussed in Section 3.3.

The global pattern characterizes the general relationship between the power and wind speed. Therefore, $G(x_i;\beta)$ in (3.1) does not include the direction d_i and turbine index n, and the same β is shared by all turbines under all directions. We model $G(x_i;\beta)$ with a regression function as

$$G(x_i;\beta) = X_{g,i}\beta, \tag{3.2}$$

where $X_{g,i}$ is a row vector in the design matrix corresponding to the wind speed x_i, and β is a column vector consisting of associated regression coefficients. This chapter uses the B-spline because of its flexible modeling capability (see details of B-spline in Section 2.6.1).

In contrast to the global trend shared by all turbines, the term $S(x_i, d_i; \eta_n, \gamma)$ in (3.1) is turbine-dependent with the turbine-specific parameter η_n, and it captures the influence of wake interactions among turbines on power generations. The spatial variations should also depend on the wind direction d_i. To characterize the heterogeneous spatial variations over a range of wind directions, we propose to use a set of canonical spatial models. We first present our approach for building canonical models and then generalize the canonical models to capture the wake interactions in any wind directions.

Let us consider L canonical spatial models. The number L can be pre-specified

using domain knowledge or learned from data (in Section 3.3 we discuss the effect of L on the estimation accuracy). Let $c_1, c_2, ..., c_L$ denote L pre-specified canonical wind directions. The l^{th} canonical model $S(x_i, c_l; \eta_{nl}, \gamma_l)$ represents the spatial variation of the n^{th} turbine's output, i.e., the discrepancy between the output from the n^{th} turbine and the output in the global term when the wind direction and speed are c_l and x_i, respectively. To represent the canonical model $S(x_i, c_l; \eta_{nl}, \gamma_l)$, we use a modeling approach similar to the global model in (3.2). Unlike the global model, however, this spatial term should capture the turbine-to-turbine variations, i.e., $S(x_i, c_l; \eta_{nl}, \gamma_l)$ at each turbine should differ. Therefore, we introduce the spatial random effect η_{nl} and model the l^{th} canonical model as

$$S(x_i, c_l; \eta_{nl}, \gamma_l) = \eta_{nl} X_{s,i} \gamma_l, \ l = 1, 2, ..., L. \tag{3.3}$$

Here, noting that the power deficit is heterogeneous over a range of wind speeds even under the same wind direction, we formulate $S(x_i, c_l; \eta_{nl}, \gamma_l)$ as a function of wind speed with the regression parameter vector γ_l. Similar to the global term, we use the B-spline for modeling $X_{s,i}\gamma_l$. As such, $X_{s,i}$ becomes a row vector in the design matrix for the B-spline basis and γ_l is the corresponding regression parameter vector.

The turbine-specific parameter η_{nl} in (3.3) captures the wake interactions among turbines, and thus, η_{nl} should depend on neighbor turbines. We formulate η_{nl} with the GMRF (*Rue and Held*, 2005; *Banerjee et al.*, 2014) as

$$\eta_{nl} | \{\eta_{ml} : m \in \mathcal{N}(n)\} \sim N\left(\sum_{m \in \mathcal{N}(n)} z_{n,m,l} \eta_{ml}, \tau_l^2 \right), \tag{3.4}$$

for $n, m = 1, 2, ..., N$ $(n \neq m)$, and $l = 1, 2, ..., L$, where $\mathcal{N}(n)$ is the set of turbine n's neighbor turbines and τ_l^2 is the conditional variance of η_{nl}. We define $\mathcal{N}(n)$ as the set of turbine n's surrounding turbines. Parameter $z_{n,m,l}$ is the dependence intensity

between turbine n and its neighboring turbine m.

For the two turbines placed close to each other, the dependence intensity $z_{n,m,l}$ should be large. We model $z_{n,m,l}$ using a direction-dependent intensity model that considers both distance and direction (*Kaiser et al.*, 2002):

$$z_{n,m,l} = \delta_{1,l} \sin^2(\theta_{n,m}) \left(\frac{1}{d_{n,m}}\right)^h + \delta_{2,l} \cos^2(\theta_{n,m}) \left(\frac{1}{d_{n,m}}\right)^h, \tag{3.5}$$

where $d_{n,m}$ is the distance between turbines n and m, and $\theta_{n,m}$ is the angle between two turbines considering the wind direction. Parameters $\delta_{1,l}$ and $\delta_{2,l}$ measure the dependence intensity in the orthogonal of and parallel to the wind direction, respectively. The interpretation of (3.5) is similar to (2.8). Scalar h ($h > 0$) is the scaling parameter that represents how quickly the intensity diminishes as the distance becomes larger.

Because the canonical spatial models capture the spatial variations under specific wind directions only, we need to generalize the canonical models in order to characterize the spatial variations under any directions. Clearly, when wind direction d_i is close to canonical wind direction c_l, the wake interaction patterns under direction d_i should be similar to that under direction c_l. The power generation pattern will also resemble the pattern under another adjacent canonical direction. Therefore, we model the spatial term $S(x_i, d_i; \eta_n, \gamma)$ in (3.1) using the weighted combination of two adjacent canonical models. Let $w_l(d_i)$ denote a similarity function between the l^{th} canonical direction c_l and the direction d_i in the i^{th} sample. We formulate $S(x_i, d_i; \eta_n, \gamma)$ as

$$S(x_i, d_i; \eta_n, \gamma) = \sum_{l=1}^{L} w_l(d_i) S(x_i, c_l; \eta_{nl}, \gamma_l), \tag{3.6}$$

for $i = 1, ..., I$, where $w_l(d_i)$ is non-zero when c_l is one of the two adjacent directions of d_i and zero for other non-adjacent directions (Figure 3.4).

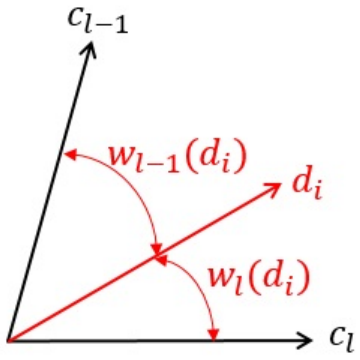

Figure 3.4: Canonical wind directions and similarity functions

We define $w_l(d_i)$ with the Gaussian kernel (*Friedman et al.*, 2009) as

$$w_l(d_i) \propto \begin{cases} \exp\left(-\dfrac{\|d_i - c_l\|^2}{\psi}\right), & \text{if } d_i \text{ is adjacent to } c_l; \\ 0, & \text{otherwise} \end{cases} \tag{3.7}$$

Here, $\|d_i - c_l\|$ is defined as $\min\{|d_i - c_l|, |360° - (d_i - c_l)|\}$. For example, for $d_i = 350°$ and $c_1 = 90°$, the difference between the two directions should be 100° instead of 260°. Note that $w_l(d_i)$ assigns a higher similarity measure to the direction that has a smaller difference. Scalar ψ quantifies how quickly the similarity decreases when d_i differs from c_l. We normalize $w_l(d_i)$ such that the sum of two non-zero weights becomes 1, i.e., $\sum_{l=1}^{L} w_l(d_i) = 1$, for each data sample i.

The similarity function in (3.7) can be defined differently. For example, we can alternatively use $w_l(d_i) \propto \|d_i - c_l\|^{-\alpha}$ with $\alpha > 0$ taking a similar role of ψ in (3.7). The results in our case study in Section 3.3 suggest that the estimation results are not sensitive to the choice of $w_l(d_i)$ formulation as long as it measures the closeness of d_i to c_l.

Figure 3.5 summarizes the proposed integrative model in capturing the variations in the power curves of multiple turbines under different wind directions.

3.2.2 Parameter estimation

To learn the canonical models and model parameters, we use the Bayesian hierarchical framework with three levels. The first level, which we refer to as the data model, specifies the model for the power output, given the canonical model and model parameters. With the global pattern in (3.2) and spatial variations in (3.6), the power output becomes

$$Y_{n,i} = X_{g,i}\beta + \sum_{l=1}^{L} w_l(d_i)\eta_{nl}X_{s,i}\gamma_l + \epsilon_{n,i}, \tag{3.8}$$

for $n = 1, 2, ..., N, i = 1, ..., I.$ and its likelihood function is

$$f(Y_{n,i}|\ X_{g,i}, X_{s,i}, \beta, \eta, \gamma, \sigma) = N\left(X_{g,i}\beta + \sum_{l=1}^{L} w_l(d_i)\eta_{nl}X_{s,i}\gamma_l, \sigma^2\right), \tag{3.9}$$

for $n = 1, 2, ..., N, i = 1, ..., I$, where η and γ denote sets of η_l's and γ_l's ($l = 1, \cdots, L$), respectively.

The second level specifies the spatial process model. With the conditional distribution for η_{nl} in (3.4), the joint distribution of $\eta_l = [\eta_{1l}, \eta_{2l}, \cdots, \eta_{Nl}]^T$ for each l becomes the multivariate normal distribution (*Cressie*, 2015; *Banerjee et al.*, 2014),

$$p(\eta_l|\delta_{1,l}, \delta_{2,l}, \tau_l^2) = MVN\left(0, \tau_l^2(\mathbb{1} - Z_l)\right), \tag{3.10}$$

where $\mathbb{1}$ is the identity matrix and Z_l is a $N \times N$ matrix whose $(n, m)^{th}$ off-diagonal element is $z_{n,m,l}$ in (3.5) and all diagonal elements are zeros.

The third level specifies a prior density for each parameter. Let θ denote a set of model parameters, $\beta, \gamma_l, \sigma^2, \tau_l^2, \delta_{1,l}, \delta_{2,l}$ ($l = 1, \cdots, L$). Then the parameter model is

$$p(\theta) \sim prior(\theta). \tag{3.11}$$

In (3.11), we use conjugate priors for $\beta, \gamma_l, \tau_l^2, \sigma^2$. Specifically, we use the multivariate

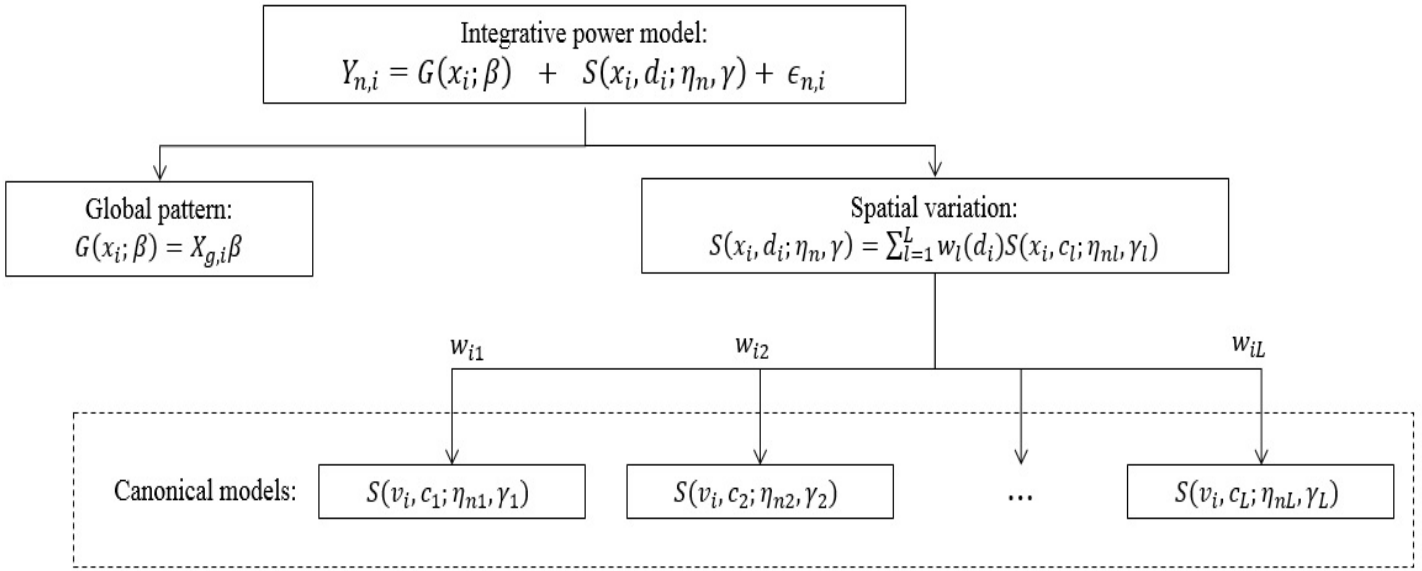

Figure 3.5: Overview of proposed integrative model using canonical spatial models and similarity functions

normal distribution for β and γ_l and the inverse Gamma distribution for τ_l^2 and σ^2 (*Banerjee et al.*, 2014). For $\delta_{1,l}$ and $\delta_{2,l}$, there are no conjugate priors, so we use uniform distributions to impose non-informative priors (see Section 3.5.1 for the full details of the priors and full conditionals used in this study).

With the Bayesian hierarchical formulation, we obtain the joint posterior distribution of η_l's and θ as

$$p(\eta_1, \eta_2, \cdots, \eta_L, \theta) \propto \prod_{n,i} \prod_{k} f(Y_{n,i} |\ X_{g,i}, X_{s,i}, \beta, \eta_l, \gamma_l, \sigma) p(\eta_l | \delta_{1,l}, \delta_{2,l}, \tau_l^2) p(\theta). \tag{3.12}$$

Because the joint posterior in (3.12) does not take a closed form, we use a sampling-based MCMC approach to simulate posterior samples for the model parameters. We implement MCMC using the WinBUGS software and call WinBUGS (*Lunn et al.*, 2012) from the R package (*Sturtz et al.*, 2005). Under the proposed Bayesian hierarchical framework, all of the model parameters, except $\delta_{1,l}$ and $\delta_{2,l}$ ($l = 1, \cdots, L$), have the closed-form full conditionals (see Section 3.5.1). Therefore, their posterior samples are drawn using Gibbs sampling. For $\delta_{1,l}$ and $\delta_{2,l}$, we note that their full conditional densities are log-concave (see Section 3.5.2), and WinBUGS employs the adaptive rejection sampling when the full conditionals are log-concave (*Lunn et al.*, 2012; *Gilks and Wild*, 1992).

Given the posterior samples, we use posterior means for estimating β, γ_l and η_{nl}, denoted as $\hat{\beta}, \hat{\gamma}_l$ and $\hat{\eta}_{nl}$, respectively, and estimate the direction-dependent power curve of each turbine as

$$\hat{Y}_{n,i} = X_{g,i}\hat{\beta} + \sum_{l=1}^{L} w_l(d_i)\hat{\eta}_{nl} X_{s,i}\hat{\gamma}_l, \tag{3.13}$$

for $n = 1, 2, ..., N, i = 1, ..., I$.

3.2.3 Learning latent canonical models

This section provides insights into how the proposed canonical models, which are latent and learned from the data, integratively capture the wake correlations over a range of wind directions. In the Gibbs sampling procedure, the posterior sample for η_l is obtained from $MVN(\mu_{\eta_l}, Q_{\eta_l}^{-1})$ with

$$\mu_{\eta_l} = \frac{1}{\sigma^2} Q_{\eta_l}^{-1} \times \left[\sum_{i=1}^{I} w_l(d_i) {\gamma_l}^T {X_{s,i}}^T (Y_i - X_{g,i}\beta \mathbb{1}_{N\times 1} - \sum_{j\neq l}^{L} w_j(d_i) X_{s,i}\gamma_j \eta_j) \right], \quad (3.14)$$

$$Q_{\eta_l} = \frac{1}{\tau_l^2}(\mathbb{1} - Z_l)^{-1} + \sum_{i=1}^{I} \frac{1}{\sigma^2} w_l^2(d_i) {\gamma_l}^T {X_{s,i}}^T X_{s,i}\gamma_l, \quad (3.15)$$

where Y_i denotes $[Y_{1,i}, Y_{2,i}, ..., Y_{N,i}]^T$ and $\mathbb{1}_{N\times 1}$ is a vector with all elements being 1 (see Section 3.5.1 for details).

These density parameters in (3.14) and (3.15) provide several important insights. First, the density parameters, which depend on $w_l(d_i)$, show that how the i^{th} sample obtained under the direction d_i affects the posterior density of η_l (see Figure 3.4). Each data sample has a different role in learning each canonical model through the similarity function $w_l(d_i)$. The data sample with a higher $w_l(d_i)$, i.e., when d_i is close to c_l, will have a greater impact on η_l's density parameters μ_{η_l} and Q_{η_l}.

Second, the last term $\sum_{j\neq l}^{L} w_j(d_i) X_{s,i}\gamma_j\eta_j$ inside the parentheses in (3.14), indicates that η_l is correlated with other η_j's. Therefore, all canonical models are correlated with one another, implying that all of the data samples are collectively used for learning multiple canonical models.

Moreover, the full conditional of η_l in (3.14) and (3.15) differs from the prior density in (3.4). The density in (3.4) formulates the *prior* correlation structure with our initial knowledge on the turbine-to-turbine interactions without using any information from the data. Under the Bayesian hierarchical modeling framework, we estimate

η_l using the joint information of the prior and observed data. The posterior density of η_l provides such insights in the Bayesian inference.

3.3 Case Study

We use 1000 samples obtained from the SCADA system of a real wind farm with more than 30 turbines. We implement MCMC with WinBUGS (*Lunn et al.*, 2012) and R (*Sturtz et al.*, 2005) statistical packages.

3.3.1 Implementation details

In our model in (3.1), x_i represents the free-flow wind speed at the i^{th} data sample. Typical wind farms have one (or a few) met-towers collecting free flow wind speeds in dominant wind directions. Our single met-tower provides free-flow wind conditions when the wind blows from west to east (Figure 3.1). When it blows in different directions, the wind flow passing the met-tower is heavily disturbed by other turbines, and as a result, the data collected from the met-tower does not represent the free wind condition.

To obtain the free wind speed in any wind direction, we employ the NTF, which uses the wind speed collected at the turbine anemometer and the speed measured at the met-tower (*Curvers and Van der Werff*, 2008). The NTF function estimates the free wind speed based on a regression equation. It uses the wind speed measured at the met-tower as the response variable and the wind speed measured at the anemometer installed on the nacelle in a upstream wind turbine as the predictor. The linear red line in Figure 3.6 shows the estimated regression line in our data set.

We note that this NTF approach for estimating the free-flow wind speeds may be restricted to large wind farms with met-towers. For small-scale wind farms that do not have a met-tower, other approaches should be employed to obtain the free-flow wind speeds. Additionally, we would like to point out that with a limited number of

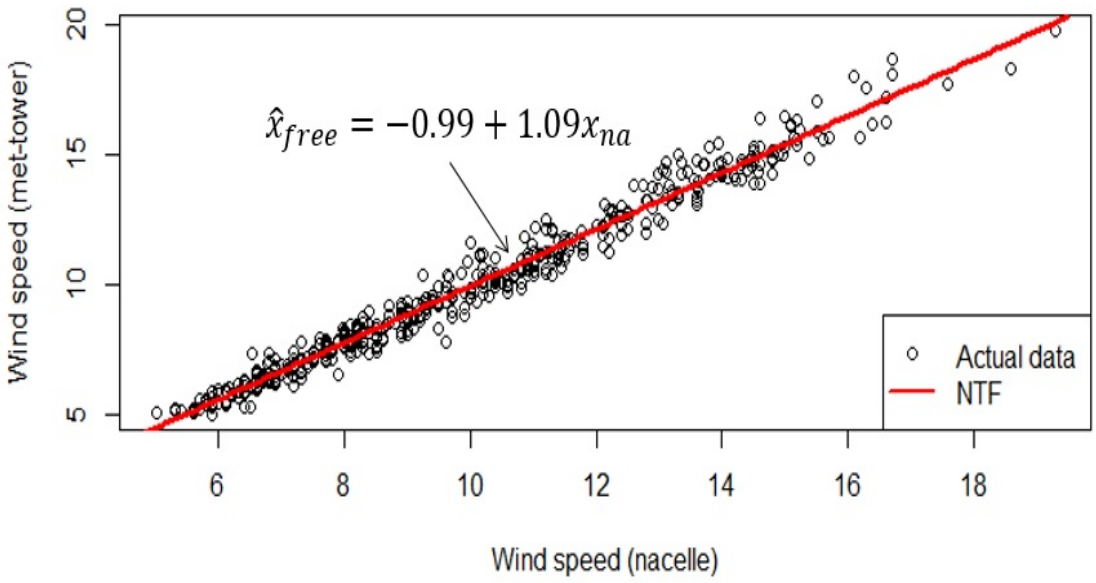

Figure 3.6: Estimated free-flow wind speed based on the wind speed measured at the anemometer on the nacelle using the Nacelle Transfer Function (NTF)

neighbor turbines in a small-scale wind farm, the advantage of our approach would be limited. This is because our approach utilizes data from neighbor turbines for characterizing the spatial correlations among turbines. As such, our approach would be useful for industrial-scale wind farms with dozens or hundreds of turbines.

For the spline functions in the global pattern in (3.2) and canonical models in (3.3), we use the same B-splines used in Chapter II. Specifically, we use the B-spline of degree 2 with five internal knots at 5 m/s, 7.5 m/s, 10 m/s, 12.5 m/s, and 15 m/s for both global and spatial terms. For h in (3.5), we use 0.5. For ψ in (3.7), our analysis with a wide range from 1 to 100 suggests that the performance of the proposed approach is not sensitive to the choice of ψ. In our analysis, we use $\psi = 20$.

In implementing MCMC, we discard the results from the first 5000 iterations as a burn-in period to wait until the Markov chain becomes fully stationary. We use the next 5000 samples to closely approximate the posterior distribution. We check the convergence of MCMC chains using statistical tests provided from the R package, coda

(*Plummer et al.*, 2006). The testing results indicate that most parameters converge well.

3.3.2 Implementation results

We implement the proposed approach with different numbers of canonical models. For each case, we consider evenly spaced canonical directions. For example, with $L = 8$, we set $c_1 = 22.5°, c_2 = 67.5°, c_3 = 112.5°, \cdots, c_8 = 337.5°$ (in Section 3.3.3, we consider another choice of canonical directions to investigate the robustness of our approach). To evaluate the performance, we employ ten-fold CV. In the 10-fold CV as we did in Chapter II. The accuracy of proposed approach is measured with RMSE and MAE.

Table 3.1 lists the estimation results of the proposed approach with different numbers of canonical models. It is interesting to see that the results are not sensitive to different canonical models. The RMSE and MAE of each model are within 1 standard deviation of other models in the 10-fold CV. This indicates that the similarity function defined in (3.7) can successfully capture the wake correlations between the canonical directions, even when a small number of canonical models are employed. The result with $L = 8$ provides the best results, and we use it in the remaining analysis.

Table 3.1: Average RMSE and MAE from 10-fold CV with different numbers of canonical models (unit: normalized power in [0, 1000] KW)

L	RMSE	MAE
4	68.57 (6.43)	47.20 (3.31)
6	67.25 (5.32)	47.15 (3.49)
8	65.93 (4.31)	45.88 (2.53)
12	66.63 (4.11)	46.34 (2.65)

Note: Numbers inside the parentheses are the standard deviations of fitting errors from the ten testing sets.

Figure 3.7(a) shows the estimated power curves of T8 and T32 under wind direc-

tion 45° and actual observations collected under $40° \sim 50°$. T8 generates less power than T32, as it is the downstream under 45°. In Figure 3.7(b), the estimated power curves of T8 and T32 under 225° can be explained likewise.

Figure 3.8 shows the estimated power curves of three wind turbines (T18, T21, and T25) under the wind direction 135°. Note that the locations of these four wind turbines are in the vertical direction (from the bottom to the top in Figure 3.1), the power deficits patterns observed from Figure 3.8 are consistent with their positions under this wind direction.

Similarly, Figure 3.9 shows the estimated power curves of four wind turbines (T8, T16, T24 and T32) under the wind direction 225° in the horizontal direction (from the left to the right in Figure 3.1). Under this wind direction, the leftmost turbine (T8) among these four turbines generates the largest power, while the rightmost turbine (T32) generates the least power.

The proposed model is also able to predict the power output at any given wind directions. Figure 3.10(a) shows the estimated power generation of T8 under $[0°, 360°]$ when wind speed is 12 m/s. The radius is the estimated power under the corresponding direction. T8 generates more power when wind direction ranges over $180° \sim 270°$ as it is the upstream turbine under this range, whereas it generates less power under $315° \sim 90°$. On the contrary, Figure 3.10(b) demonstrates that the power generation of T21 is not sensitive to the direction because it is located inside the wind farm.

Figure 3.11 depicts that T18 generates larger power outputs under 315° compared to those under other two directions. Moreover, the power deficits among different wind directions preserve the heterogeneous patterns. That is, the deficits are only significant when the wind speed is between 8 m/s and 14 m/s, while the deficits diminish when the wind speed is either low (<8 m/s) or high (>14 m/s).

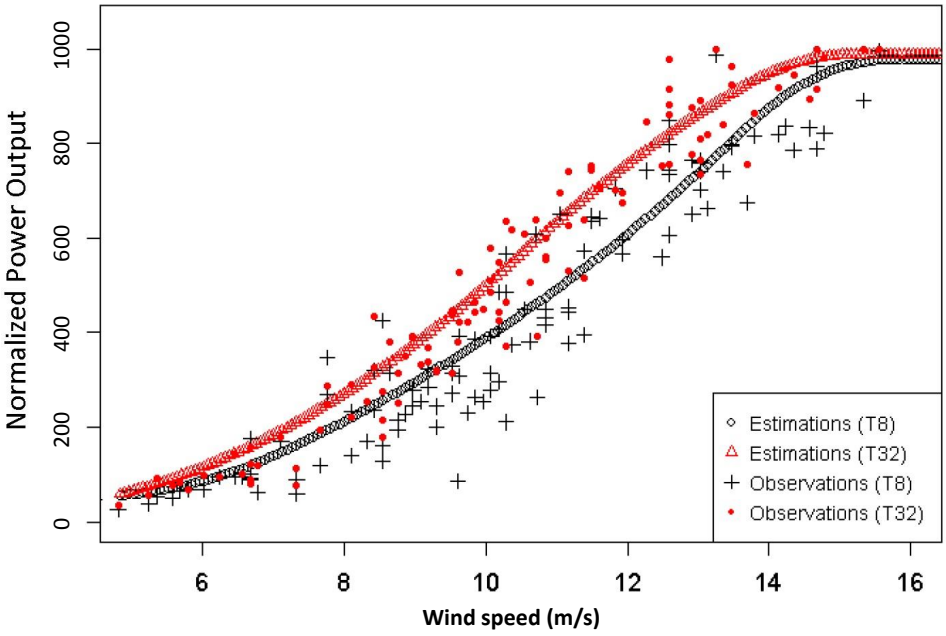

(a) Estimated power curves under 45° and actual observations under 40° ∼ 50°

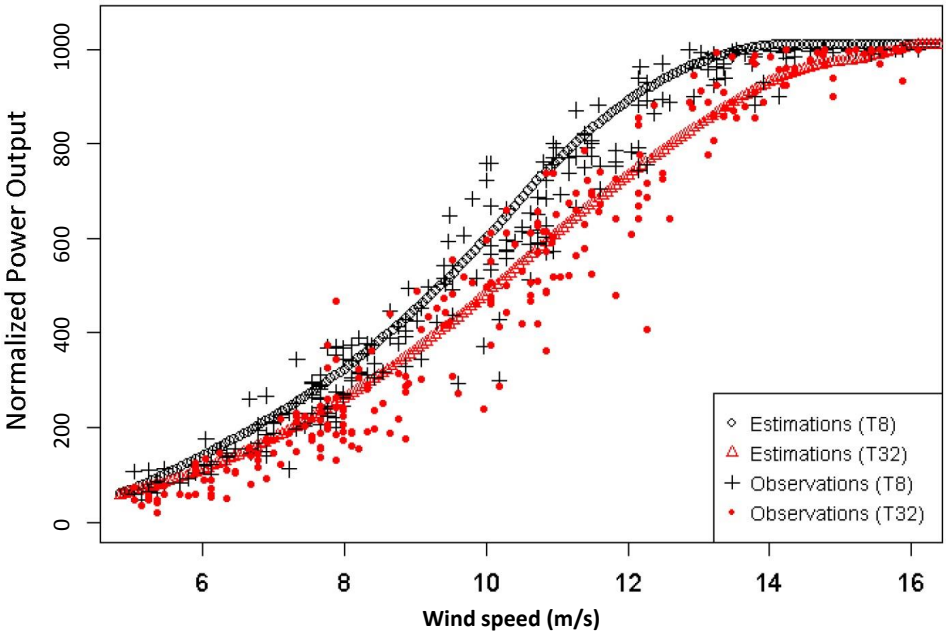

(b) Estimated power curves under 225° and actual observations under 220° ∼ 230°

Figure 3.7: Estimated and observed power outputs of T8 and T32

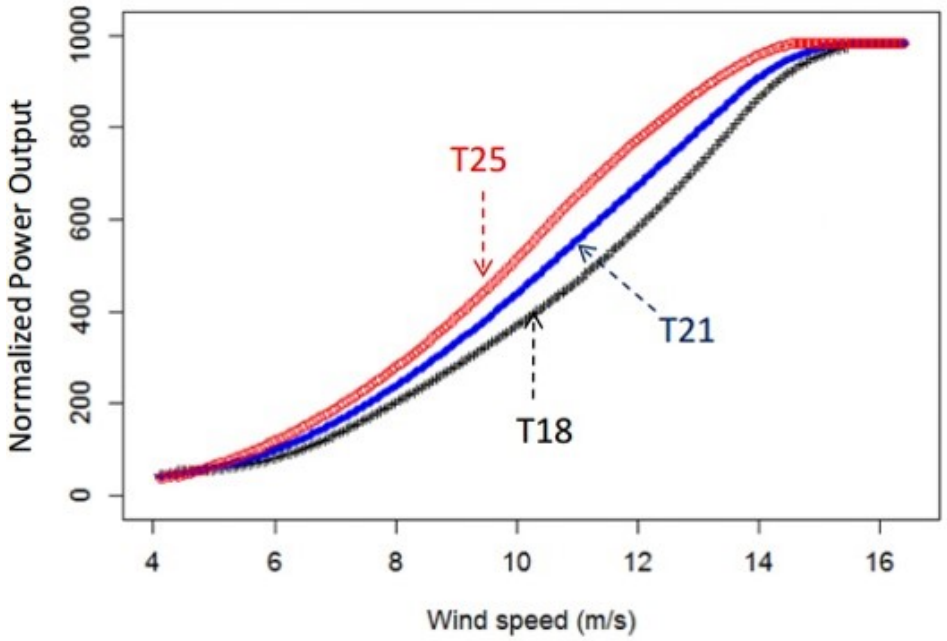

Figure 3.8: Estimated power curves of T18, T21, and T25 under the wind direction 135°

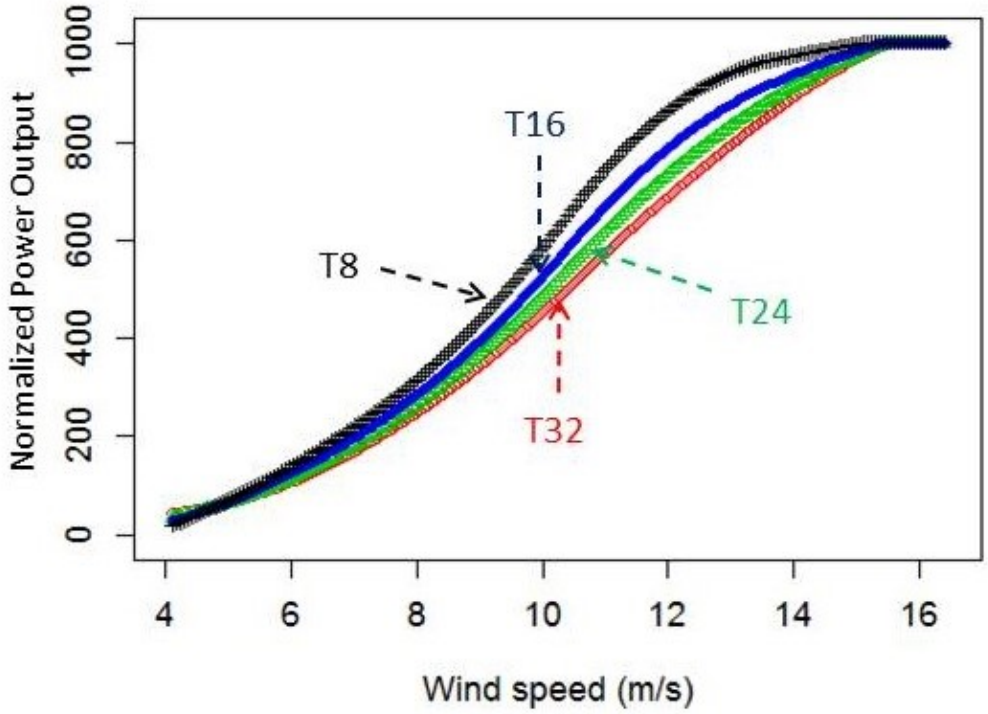

Figure 3.9: Estimated power curves of T8, T16, T24 and T32 under the wind direction 225°

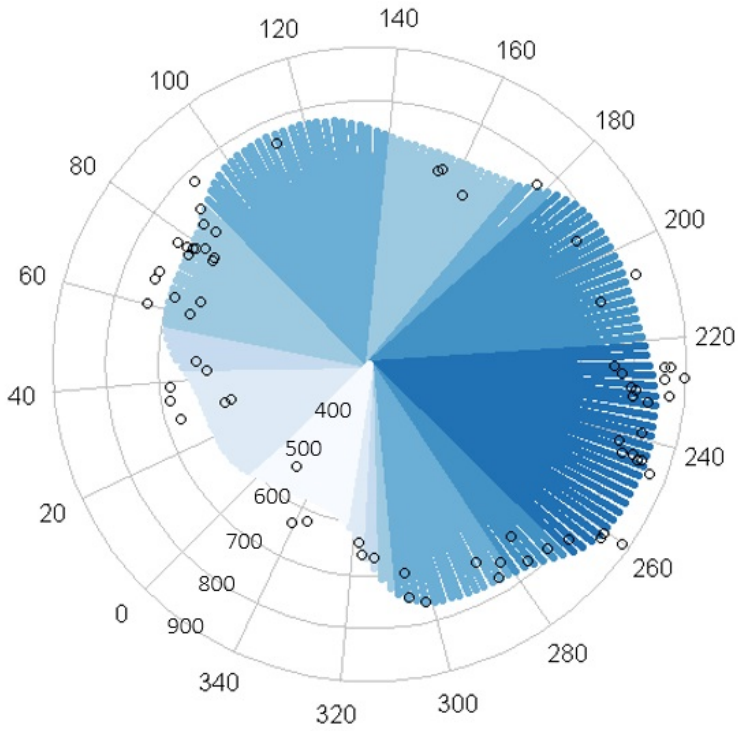

(a) T8

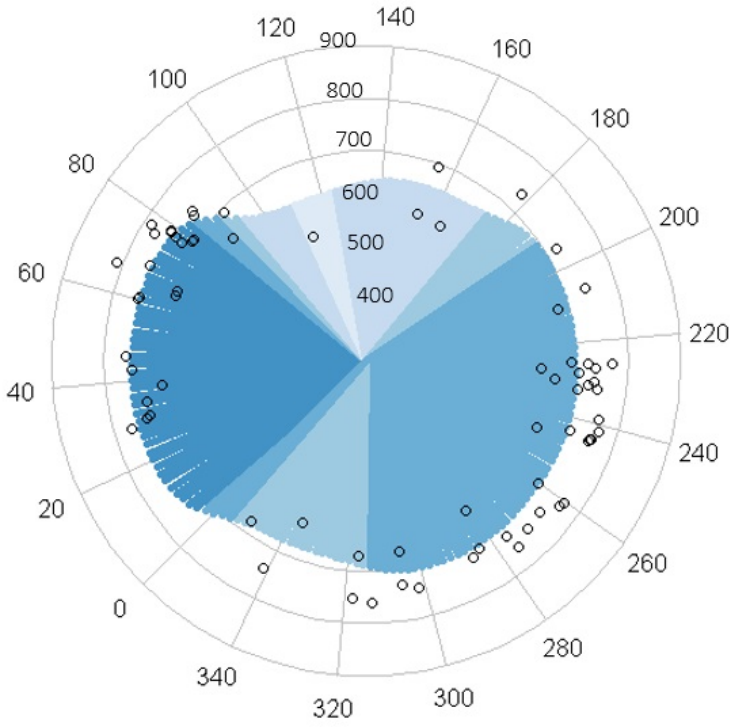

(b) T21

Figure 3.10: Estimated power when wind speed is 12 m/s (note: small circles denote the observed power outputs at 11.9 m/s $\sim$ 12.1 m/s)

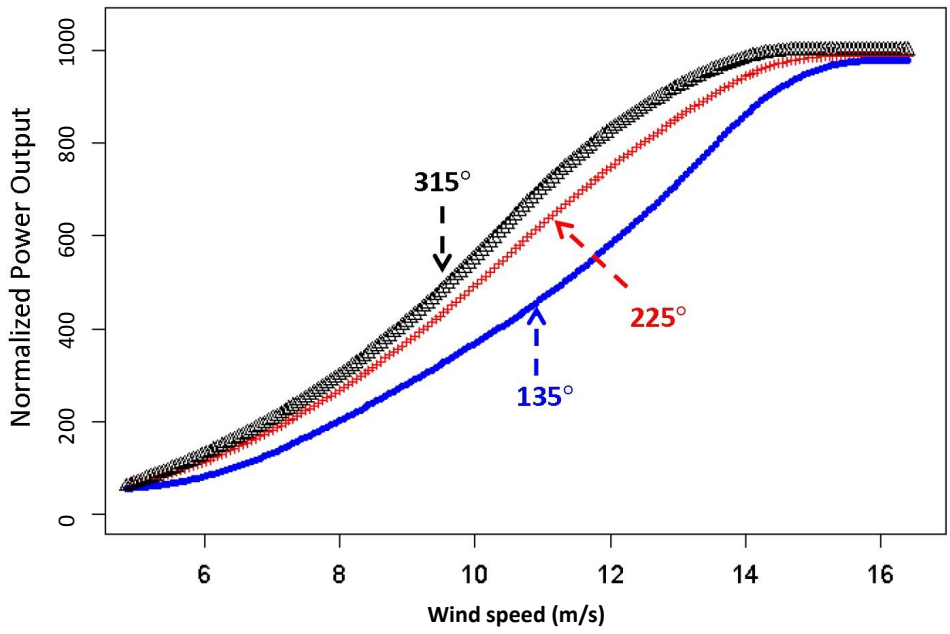

Figure 3.11: Estimated power curve of T18 under three different wind directions

3.3.3 Sensitivity analysis on canonical wind directions

To investigate the effect of the locations of canonical directions, we also implement the proposed approach with a different choice of canonical directions. Specifically, noting that in general, wind directions are not evenly distributed over $[0°, 360°]$ (see Figure 3.12 for the histogram of wind directions in our dataset). We consider the distribution of wind directions at the wind farm site. We decompose the direction such that each sector $[c_{l-1}, c_l]$, $l = 1, \cdots, L$, includes the same number of samples. Therefore, under the high frequency direction range (i.e., dominant wind directions), the sector between two canonical directions is narrow, whereas the sector is wide under the low frequency direction range. The red dashed lines in Figure 3.12 show this choice of canonical wind directions, while the blue solid lines depict the evenly spaced canonical wind directions.

The resulting average RMSE and MAE from the 10-fold CV with this set of unevenly spaced canonical directions are 66.08 and 45.88, respectively, which are

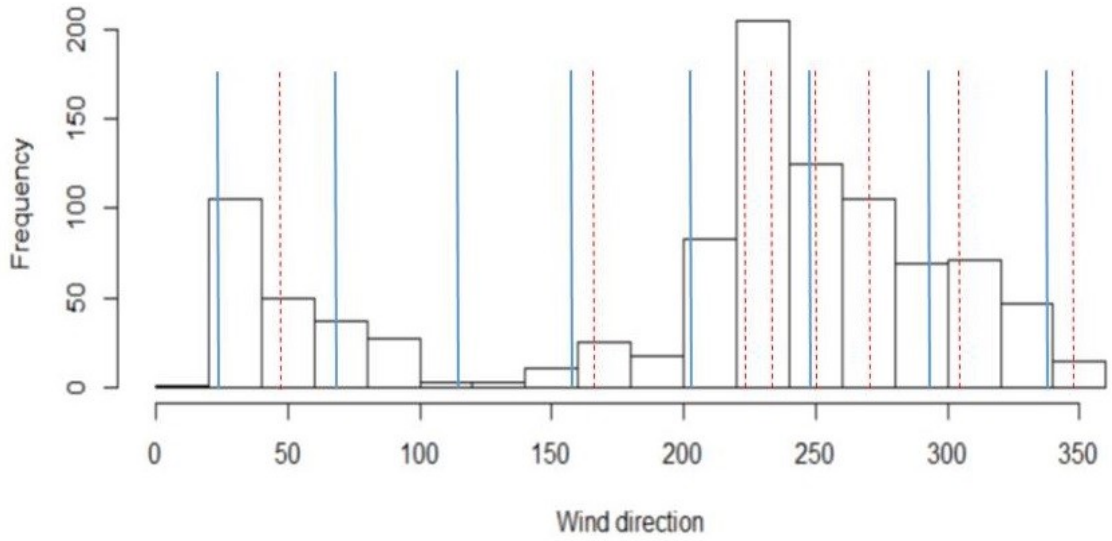

Figure 3.12: Histogram of wind directions and two different selections on canonical wind directions: blue solid lines divide the evenly spaced direction sectors, whereas the red dashed lines divide the sections with the equal number of observations at each section

very close to the estimation errors in Table 3.1 (see the fourth row with $L = 8$). This result suggests the robustness of the proposed approach on the choice of canonical directions.

3.3.4 Comparison with alternative approaches

We compare the performance of the proposed approach with several alternative methods. First, we implement the method in Chapter II using data in the dominant direction and apply the resulting power curves to estimate the power outputs over all directions. This approach is called an approach with dominant direction. Moreover we consider three individual models that have turbine-specific spline regression

parameters:

$$(\text{IND1}) : P_{n,i} = V_i\beta_n + D_i\gamma_n + \epsilon_{n,i}, \tag{3.16}$$

$$(\text{IND2}) : P_{n,i} = V_i\beta_n + D_i\gamma_n + T_i\lambda_n + \epsilon_{n,i}, \tag{3.17}$$

$$(\text{IND3}) : P_{n,i} = V_{s,i}\beta_n + V_{c,i}\gamma_n + \epsilon_{n,i}, \tag{3.18}$$

for $n = 1, ..., N$ and $i = 1, ..., I$. Here, in IND1, V_i and D_i are the row vectors in the design matrices corresponding to the wind speed v_i and direction d_i, respectively. We employ the B-spline for the wind speed and the cyclic B-spline for the wind direction. In IND2, we additionally include the interaction term T_i between wind speed and direction, where T_i is the row vector of the B-spline design matrix associated with the predictor $v_i d_i$. In IND3, $V_{s,i}$ and $V_{c,i}$ denote the row vectors of the B-spline design matrix corresponding to $v_i sin(d_i)$ and $v_i cos(d_i)$, respectively. Note that all three individual models have turbine-specific parameters. In each model, the model parameters are estimated separately using the power output data from each turbine, resulting N regression functions.

Table 3.2 compares the estimation performance of the proposed approach with alternative models in terms of the RMSE and MAE. Clearly, the proposed model outperforms other models. The result of the approach with dominant direction indicates that the power curves fitted under a fixed direction are not adequate to estimate the power outputs under other directions.

Table 3.2: Performance comparisons (unit: normalized power in [0, 1000] KW)

Model	RMSE	MAE
Proposed approach	65.93 (4.31)	45.88 (2.53)
Approach with dominant direction	86.19 (6.65)	59.33 (3.77)
IND1	70.13 (4.10)	49.53 (2.64)
IND2	68.27 (4.21)	48 .34 (2.84)
IND3	89.10 (7.64)	63.73 (3.77)

Note: Numbers inside the parentheses are the standard deviations of fitting errors from the ten testing sets.

Among the three individual models, we note that the estimation performance of IND2 is close to that of the proposed approach. Despite the small difference in this case, our method provides better implications for understanding the wake effects, because we directly model the interactions among turbines. Therefore, our approach can be possibly used for optimizing the wind farm control and/or layout design (which will be discussed in Chapter V). On the contrary, the individual approach does not model the inter-dependencies among turbines, so it is difficult to use it for improving the power generation efficiency at the wind-farm level.

3.4 Summary

An integrative approach is developed for fitting the direction-dependent power curves of multiple interacting wind turbines. Our approach uses a combination of canonical models and similarity functions to capture the wake correlations in any wind directions. A comprehensive case study suggests that the proposed approach improves the estimation accuracy of power outputs from the multiple turbines when compared with other individual approaches. The results also suggest that applying the power curves constructed under a specific direction is not adequate to achieve a high estimation accuracy in other directions.

3.5 Appendix for Chapter III

3.5.1 Full conditionals for model parameters

This section derives the conditional distribution for each model parameter. Let $\mathcal{D}_y$, $\mathcal{D}_v$ and $\mathcal{D}_d$ denote the sets of observed power, wind speed and direction, respectively.

- With $N(0, \sigma_1^2 \mathbb{1})$ as prior for each parameter in β, the full conditional for β is

$$\begin{aligned}
p(\beta|\mathcal{D}_y, \mathcal{D}_v, \mathcal{D}_d, \eta, \gamma, \sigma) &\propto \prod_{n,i} f(Y_{n,i}|\ X_{g,i}, X_{s,i}, \beta, \eta, \gamma, \sigma) p(\beta) \\
&\propto \prod_{i=1}^{I} \exp[-\frac{1}{2\sigma^2} \left(Y_i - X_{g,i}\beta \mathbb{1}_{N\times 1} - \sum_{j=1}^{L} w_j(d_i) X_{s,i} \gamma_j \eta_j \right)^T \\
&\quad \left(Y_i - X_{g,i}\beta \mathbb{1}_{N\times 1} - \sum_{j=1}^{L} w_j(d_i) X_{s,i} \gamma_j \eta_j \right)] \\
&\quad \times \exp\left(-\frac{1}{2} \beta^T \frac{1}{\sigma_1^2} \mathbb{1} \beta \right) \\
&\propto \exp[-\frac{1}{2} \beta^T \left(\sum_{i=1}^{I} \frac{1}{\sigma^2} {X_{g,i}}^T X_{g,i} + \frac{1}{\sigma_1^2} \mathbb{1} \right) \beta \\
&\quad + \sum_{i=1}^{I} \left(Y_i - \sum_{j=1}^{L} w_j(d_i) X_{s,i} \gamma_j \eta_j \right)^T \frac{1}{\sigma^2} \mathbb{1}_{N\times 1} X_{g,i} \beta] \\
&\sim MVN(\mu_\beta, Q_\beta^{-1}),
\end{aligned}$$

where

$$\begin{aligned}
Q_\beta &= \frac{1}{\sigma_1^2} \mathbb{1} + \sum_{i=1}^{I} \frac{1}{\sigma^2} {X_{g,i}}^T X_{g,i}, \\
\mu_\beta &= \frac{1}{\sigma^2} Q_\beta^{-1} \left[\sum_{i=1}^{I} {X_{g,i}}^T \mathbb{1}_{1\times N} \left(Y_i - \sum_{j=1}^{L} w_j(d_i) X_{s,i} \gamma_j \eta_j \right) \right].
\end{aligned}$$

- With $N(0, \sigma_1^2 \mathbb{1})$ as prior for each parameter in γ_l, the full conditional for γ_l is

$$\begin{aligned}
p(\gamma_l|\mathcal{D}_y, \mathcal{D}_v, \mathcal{D}_d, \eta, \beta, \sigma) &\propto \prod_{n,i} f(Y_{n,i}|\ X_{g,i}, X_{s,i}, \beta, \eta, \gamma, \sigma) p(\gamma_l) \\
&\quad \prod_{i=1}^{I} \exp[-\frac{1}{2\sigma^2} \left(Y_i - X_{g,i}\beta \mathbb{1}_{N\times 1} - \sum_{j=1}^{L} w_j(d_i) X_{s,i}\gamma_j\eta_j \right)^T \\
&\quad \left(Y_i - X_{g,i}\beta \mathbb{1}_{N\times 1} - \sum_{j=1}^{L} w_j(d_i) X_{s,i}\gamma_j\eta_j \right)] \\
&\quad \times \exp\left(-\frac{1}{2} {\gamma_l}^T \frac{1}{\sigma_1^2} \mathbb{1} \gamma_l \right) \\
&\propto \exp[-\frac{1}{2} {\gamma_l}^T \left(\sum_{i=1}^{I} \frac{1}{\sigma^2} w_l^2(d_i) \eta_l^T {X_{s,i}}^T X_{s,i} \eta_l + \frac{1}{\sigma_1^2}\mathbb{1} \right) \gamma_l \\
&\quad + \sum_{i=1}^{I} (P_i - X_{g,i}\beta \mathbb{1}_{N\times 1} - \sum_{j\neq l}^{L} w_j(d_i) X_{s,i}\gamma_j\eta_j)^T \\
&\quad \times \frac{1}{\sigma^2} w_l(d_i) \eta_l X_{s,i} \gamma_l] \\
&\sim MVN(\mu_{\gamma_l}, Q_{\gamma_l}^{-1}),
\end{aligned}$$

where

$$\begin{aligned}
Q_{\gamma_l} &= \frac{1}{\sigma_1^2}\mathbb{1} + \sum_{i=1}^{I} \frac{1}{\sigma^2} w_l^2(d_i) \eta_l^T {X_{s,i}}^T X_{s,i} \eta_l, \\
\mu_{\gamma_l} &= \frac{1}{\sigma^2} Q_{\gamma_l}^{-1} \left[\sum_{i=1}^{I} w_l(d_i) {X_{s,i}}^T \eta_l^T (Y_i - X_{g,i}\beta \mathbb{1}_{N\times 1} - \sum_{j\neq l}^{L} w_j(d_i) X_{s,i}\gamma_j\eta_j) \right].
\end{aligned}$$

- With the spatial process model in (3.10), the full conditional for η_l for each k is

$$\begin{aligned}
p(\eta_l|\mathcal{D}_y,\mathcal{D}_v,\mathcal{D}_d,\beta,\sigma) &\propto \prod_{n,i} f(Y_{n,i}|\ X_{g,i},X_{s,i},\beta,\eta,\gamma,\sigma)p(\eta_l) \\
&\propto \prod_{i=1}^{I}\exp[-\frac{1}{2\sigma^2}\left(Y_i - X_{g,i}\beta\mathbb{1}_{N\times 1} - \sum_{j=1}^{L} w_j(d_i)X_{s,i}\gamma_j\eta_j\right)^T \\
&\quad \left(Y_i - X_{g,i}\beta\mathbb{1}_{N\times 1} - \sum_{j=1}^{L} w_j(d_i)X_{s,i}\gamma_j\eta_j\right)] \\
&\quad \times\exp\left(-\frac{1}{2\tau_l^2}\eta_l^T(\mathbb{1}-Z_l)^{-1}\eta_l\right) \\
&\propto \exp[-\frac{1}{2}\eta_l^T\left(\sum_{i=1}^{I}\frac{1}{\sigma^2}w_l^2(d_i){\gamma_l}^T{X_{s,i}}^T X_{s,i}\gamma_l + \frac{1}{\tau_l^2}(\mathbb{1}-Z_l)^{-1}\right)\eta_l \\
&\quad +\sum_{i=1}^{I}(Y_i - X_{g,i}\beta\mathbb{1}_{N\times 1} - \sum_{j\neq l}^{L} w_j(d_i)X_{s,i}\gamma_j\eta_j)^T \\
&\quad \times\frac{1}{\sigma^2}w_l(d_i)X_{s,i}\gamma_l\eta_l] \\
&\sim MVN(\mu_{\eta_l},Q_{\eta_l}^{-1}),
\end{aligned}$$

where

$$\begin{aligned}
Q_{\eta_l} &= \frac{1}{\tau_l^2}(\mathbb{1}-Z_l)^{-1} + \sum_{i=1}^{I}\frac{1}{\sigma^2}w_l^2(d_i){\gamma_l}^T{X_{s,i}}^T X_{s,i}\gamma_l, \\
\mu_{\eta_l} &= \frac{1}{\sigma^2}Q_{\eta_l}^{-1}\left[\sum_{i=1}^{I} w_l(d_i){\gamma_l}^T{X_{s,i}}^T(Y_i - X_{g,i}\beta\mathbb{1}_{N\times 1} - \sum_{j\neq l}^{L} w_j(d_i)X_{s,i}\gamma_j\eta_j)\right].
\end{aligned}$$

- With the inverse gamma distribution $IG(\alpha_\tau,\kappa_\tau)$ as prior, the full conditional

for τ_l^2 is

$$\begin{aligned} p(\tau_l^2|\mathcal{D}_y, \eta_l) &\propto p(\eta_l|\tau_l^2)p(\tau_l^2) \\ &\propto \left|\frac{1}{\tau_l^2}(\mathbb{1} - Z_l)^{1/2}\right| \exp\left(-\frac{1}{2\tau_l^2}\eta_l^T(\mathbb{1} - Z_l)\eta_l\right) \exp\left(-\frac{\kappa_1}{\tau_l^2}\right)(\tau_l^2)^{-\alpha_1-1} \\ &\propto (\tau_l^2)^{-N/2-\alpha_1-1} \exp\left(-\frac{\kappa_1 + \eta_l^T(\mathbb{1} - Z_l)\eta_l/2}{\tau_l^2}\right) \\ &\sim IG(\alpha_\tau, \kappa_\tau), \end{aligned}$$

where

$$\begin{aligned} \alpha_\tau &= N/2 + \alpha_1, \\ \kappa_\tau &= \kappa_1 + \eta_l^T(\mathbb{1} - Z_l)\eta_l/2. \end{aligned}$$

- With $IG(\alpha_\sigma, \kappa_\sigma)$ as prior, the full conditional for σ^2 is

$$\begin{aligned} p(\sigma^2|\mathcal{D}_y, \beta, \eta, \gamma) &\propto \prod_{n,i} f(Y_{n,i}|\ X_{g,i}, X_{s,i}, \beta, \eta, \gamma, \sigma)p(\sigma^2) \\ &\propto \prod_{i=1}^{I} \exp[-\frac{1}{2\sigma^2}\left(Y_i - X_{g,i}\beta\mathbb{1}_{N\times 1} - \sum_{j=1}^{L} w_j(d_i)X_{s,i}\gamma_j\eta_j\right)^T \\ &\quad \left(Y_i - X_{g,i}\beta\mathbb{1}_{N\times 1} - \sum_{j=1}^{L} w_j(d_i)X_{s,i}\gamma_j\eta_j\right)] \\ &\quad \times(\sigma^2)^{-NI/2-\alpha_1-1} \exp\left[-\frac{\kappa_1}{\sigma^2}\right] \\ &\sim IG(\alpha_\sigma, \kappa_\sigma), \end{aligned}$$

where

$$\begin{aligned}
\alpha_\sigma &= NI/2 + \alpha_1, \\
\kappa_\sigma &= \kappa_1 + \frac{1}{2}\sum_{i=1}^{I}\left(Y_i - X_{g,i}\beta\mathbb{1}_{N\times 1} - \sum_{j=1}^{L} w_j(d_i)X_{s,i}\gamma_j\eta_j\right)^T \\
&\quad \left(Y_i - X_{g,i}\beta\mathbb{1}_{N\times 1} - \sum_{j=1}^{L} w_j(d_i)X_{s,i}\gamma_j\eta_j\right).
\end{aligned}$$

- With the uniform distribution as prior, the full conditional for $\delta_{1,l}$ and $\delta_{2,l}$ is not closed form, but it satisfies

$$p(\delta_{1,l}|\mathcal{D}_y, \mathcal{D}_v, \mathcal{D}_d, \eta_l, \tau_l^2, \delta_{2,l}) \propto \ |(\mathbb{1} - Z_l)^{1/2}| \exp\left(-\frac{1}{2\tau_l^2}\eta_l^T(\mathbb{1} - Z_l)\eta_l\right),$$

  for $-B \leq \delta_{1,l} \leq B$, and 0 elsewhere. The $(n,m)^{th}$ element of Z_l is specified in (3.5). The full conditional of $\delta_{2,l}$ has the same form of $\delta_{1,l}$ except that it is a function on $\delta_{2,l}$.

All parameters except $\delta_{1,l}$ and $\delta_{2,l}$ have closed forms of their full conditionals. The WinBUGS employs the Gibbs sampling to draw the posterior samples for those parameters. To sample $\delta_{1,l}$ and $\delta_{2,l}$, the adaptive rejection algorithm is used as their full conditionals are log-concave (*Lunn et al.*, 2012).

3.5.2 Proof of the log-concavity of the full conditionals of $\delta_{1,l}$ and $\delta_{2,l}$ for $l = 1, 2, ..., L$

The WinBUGS uses the adaptive rejection sampling when the parameter's full conditional density is log-concave (*Ntzoufras*, 2011; *Kéry and Schaub*, 2011). It has been known that the adaptive rejection sampling is more efficient than the Metropolis-Hastings algorithm.

This section shows the log-concavity for $\delta_{1,l}$, $l = 1, 2, ..., L$. The log-concavity

for $\delta_{2,l}$ can be similarly shown. Note that as the prior for $\delta_{1,l}$, we use the uniform distributions with the upper bound B and lower bound $-B$. Let $\mathcal{D}_y$, $\mathcal{D}_v$ and $\mathcal{D}_d$ denote the sets of observed power, wind speed and direction, respectively. The full conditional of $\delta_{1,l}$ is:

$$\begin{aligned} p(\delta_{1,l}|\mathcal{D}_y, \mathcal{D}_v, \mathcal{D}_d, \eta_l, \tau_l^2) &\propto p(\eta_l, \tau_l^2|\delta_{1,l}, \delta_{2,l}) P(\delta_{1,l}) \\ &\propto |(\mathbb{1} - Z_l)^{1/2}| \exp\left(-\frac{1}{2\tau_l^2}\eta_l^T(\mathbb{1} - Z_l)\eta_l\right) \text{ for } -B \leq \delta_{1,l} \leq B, \end{aligned}$$

and $p(\delta_{1,l}|\mathcal{D}_y, \mathcal{D}_v, \mathcal{D}_d, \eta_l, \tau_l^2) = 0$ for either $\delta_{1,l} < B$ or $\delta_{1,l} > B$, where

$$z_{n,m,l} = \delta_{1,l} \sin^2(\theta_{n,m}) d_{n,m}^{-h} + \delta_{2,l} \cos^2(\theta_{n,m}) d_{n,m}^{-h}. \tag{3.19}$$

with fixed $\theta_{n,m}, d_{n,m}^{-h}$ and h.

Let

$$f(\delta_{1,l}) = \begin{cases} |(\mathbb{1} - Z_l)^{1/2}| \exp\left(-\frac{1}{2\tau_l^2}\eta_l^T(\mathbb{1} - Z_l)\eta_l\right), & \text{if } -B \leq \delta_{1,l} \leq B, \\ 0, & \text{otherwise.} \end{cases} \tag{3.20}$$

To show the log-concavity, we need to show that

$$\log f(\xi\delta_{1\star,l} + (1-\xi)\delta_{1\star\star,l}) \geq \xi \log f(\delta_{1\star,l}) + (1-\xi) f(\delta_{1\star\star,l}), \quad 0 < \forall\xi < 1. \tag{3.21}$$

Suppose that either $\xi\delta_{1\star,l} + (1-\xi)\delta_{1\star\star,l} < -B$ or $\xi\delta_{1\star,l} + (1-\xi)\delta_{1\star\star,l} > B$. This occurs when at least one of $\delta_{1\star,l}$ and $\delta_{1\star\star,l}$ falls out of the interval $[-B, B]$. In this case, both sides of (3.21) is $-\infty$, which makes the inequality in (3.21) hold. If at least one of $\delta_{1\star,l}$ and $\delta_{1\star\star,l}$ falls out of the interval $[-B, B]$ and $\xi\delta_{1\star,l} + (1-\xi)\delta_{1\star\star,l}$ is between $-B$ and B, the inequality in (3.21) still holds.

Therefore, we only need to show that $f(\delta_{1,l})$ is log-concave for $-B \leq \delta_{1,l} \leq B$. Note that for $-B \leq \delta_{1,l} \leq B$, the matrix $\mathbb{1} - Z_l$ is always positive definite. Thus,

$f(\delta_{1,l})$ is always greater than 0 and well-defined. To show $f(\delta_{1,l})$ is log-concave, it suffices to show the second derivate of $\log f(\delta_{1,l})$ is non-positive. First note that

$$\log f(\delta_{1,l}) = \frac{1}{2}\log\left(|(\mathbb{1} - Z_l)|\right) - \frac{1}{2\tau_l^2}\eta_l^T(\mathbb{1} - Z_l)\eta_l \tag{3.22}$$

and $\frac{1}{2\tau_l^2}\eta_l^T(\mathbb{1} - Z_l)\eta_l$ is a linear function on δ_1^l. Thus, we have

$$(\log f(\delta_{1,l}))'' = \frac{1}{2}(\log\left(|(\mathbb{1} - Z_l)|\right))''. \tag{3.23}$$

Then

$$\begin{aligned}(\log\left(|(\mathbb{1} - Z_l)|\right))' &= \frac{1}{|(\mathbb{1} - Z_l)|}|(\mathbb{1} - Z_l)|tr\left((\mathbb{1} - Z_l)^{-1}(\mathbb{1} - Z_l)'\right) &(3.24)\\ &= tr((\mathbb{1} - Z_l)^{-1}(\mathbb{1} - Z_l)'), &(3.25)\end{aligned}$$

where $tr(\cdot)$ denotes the trace of the matrix.

As $\delta_{1,l}$ is linear in Z_l (3.19), then $(\mathbb{1} - Z_l)'$ does not include $\delta_{1,l}$. Therefore, we have

$$(\log\left(|(\mathbb{1} - Z_l)|\right))'' = -tr\left((\mathbb{1} - Z_l)^{-1}(\mathbb{1} - Z_l)'(\mathbb{1} - Z_l)^{-1}(\mathbb{1} - Z_l)'\right) \tag{3.26}$$

Because Z_l is symmetric, $(\mathbb{1} - Z_l)'$ and $(\mathbb{1} - Z_l)^{-1}$ are also symmetric. Moreover, $(\mathbb{1} - Z_l)^{-1}$ is positive definite. Then $(\mathbb{1} - Z_l)'(\mathbb{1} - Z_l)^{-1}(\mathbb{1} - Z_l)'$ is also positive semidefinite because for any vector x, we have $x^T(\mathbb{1} - Z_l)'(\mathbb{1} - Z_l)^{-1}(\mathbb{1} - Z_l)'x = [(\mathbb{1} - Z_l)'x]^T(\mathbb{1} - Z_l)^{-1}(\mathbb{1} - Z_l)'x \geq 0$.

Finally, for a positive definite matrix $(\mathbb{1} - Z_l)^{-1}$, there exists a matrix M such

that $MM^T = (\mathbb{1} - Z_l)^{-1}$. Then, from (3.26) we have

$$\begin{aligned} (\log(|(\mathbb{1} - Z_l)|))'' &= -tr\left(MM^T(\mathbb{1} - Z_l)'(\mathbb{1} - Z_l)^{-1}(\mathbb{1} - Z_l)'\right) && (3.27) \\ &= -tr\left(M^T(\mathbb{1} - Z_l)'(\mathbb{1} - Z_l)^{-1}(\mathbb{1} - Z_l)'M\right). && (3.28) \end{aligned}$$

As $(\mathbb{1}-Z_l)'(\mathbb{1}-Z_l)^{-1}(\mathbb{1}-Z_l)'$ is positive semidefinite, $M^T(\mathbb{1}-Z_l)'(\mathbb{1}-Z_l)^{-1}(\mathbb{1}-Z_l)'M$ is also positive semidefinite. This implies that

$$(\log(|(\mathbb{1} - Z_l)|))'' \leq 0. \tag{3.29}$$

This shows the second derivative of $\log f(\delta_{1,l})$ is non-positive, which implies that $f(\delta_{1,l})$ is concave.

CHAPTER IV

Quantification of the VG Upgrade under Wake Effects

4.1 Introduction

In wind industry, the VG installation on the turbine blades is important in efforts of improving the power generation efficiency of a wind turbine (*Paraschivoiu*, 2002; *Massouh and Dobrev*, 2007). The benefits of installing the VG are mainly two-folds: A main benefit, it increases the power production at the VG upgraded turbine. Another benefit is that it reduces the turbulence of the wind flows (*Timmer and Van Rooij*, 2003; *Storms and Jang*, 1994). Both aspects may change the wake interactions among turbines. However, existing studies have been focusing on the power improvement at a single VG upgraded turbine without considering wake effects (*Sullivan*, 1984; *Lee et al.*, 2015b).

In this chapter, we examine the effect of the VG upgrade on power generation efficiency in the presence of the wake effects in a multi-turbine wind farm. The motivation of this chapter is from the fact that the VG upgrade can reduce the wind flow's turbulence. As a result, the VG upgrade may change the wake characteristics among turbines, consequently affecting power generation efficiency at the VG upgraded turbine and their neighbor turbines.

We use a dataset collected from an operational wind farm. Please note that the wind farm considered in this chapter is different from that studied in the previous chapters. Figure 4.1 shows the partial layout of the wind farm. Due to the confidentiality of the dataset, we slightly change the locations of turbines, while preserving the order of upstream and downstream turbines under the wind direction as specified by the arrows along the left side. The VG is installed at Turbine T6 several years after the wind farm became operational. The data collected before and after the VG upgrade is available. We consider the wind direction from the left to the right (westerly direction) when the met-tower is not under wake. The met-tower measures the free-flow wind speed and other wind conditions such as the turbulence intensity in the westerly direction.

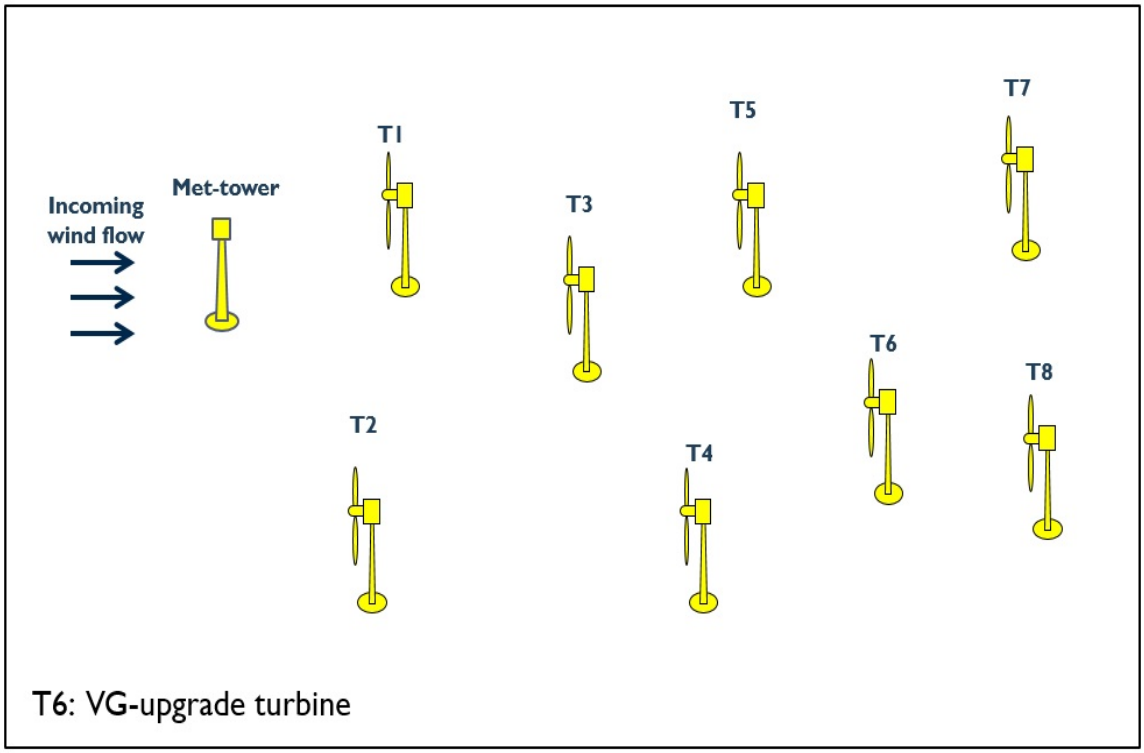

Figure 4.1: Locations of the VG upgraded and neighboring turbines

As Figure 4.1 shows, the westerly wind flow passes through at least four wind turbines before it meets T6. As such, T6 is heavily affected by the wake effects.

Therefore, its VG upgrade effect should be quantified in combination with wake effects. Figure 4.2 shows the power generations of T1, one of the upstream turbines, and the upgraded turbine T6 from the dataset collected before the VG installation in the westerly wind direction. The x-axis is the 10-minute average wind speed measured at the met-tower, and the y-axis is the 10-minute average power outputs (we rescale the power output to [0, 1000] KW for keeping the data confidentiality). Clearly, Figure 4.2 shows that T6 generates less power than T1 in general.

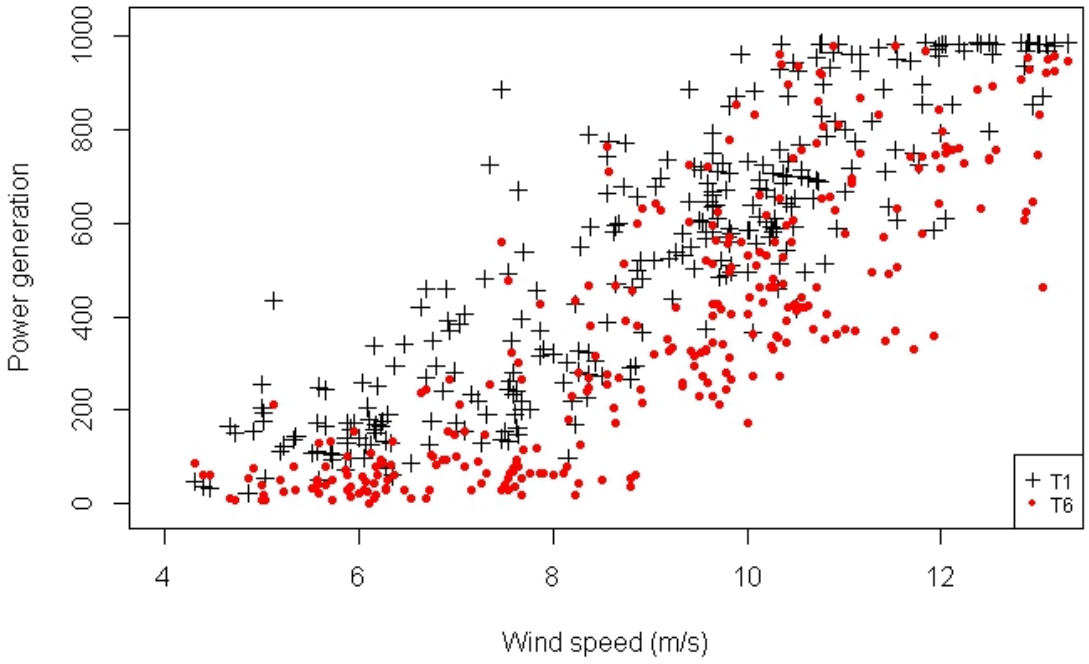

Figure 4.2: Power outputs from T1 (control turbine) and T6 (upgraded turbine)

To see the VG effect, Figure 4.3 depicts the the power outputs of T6 before and after the VG installation. Despite large amounts of noise, T6 appears to generate more power after the VG installation. Wind farm operators need quantitative assessments about the power gain obtained from the upgrade, so that they can justify the upgrade investment. Building upon the model presented in Chapter II, this chapter

investigates how much power gain can be obtained from the VG upgrade.

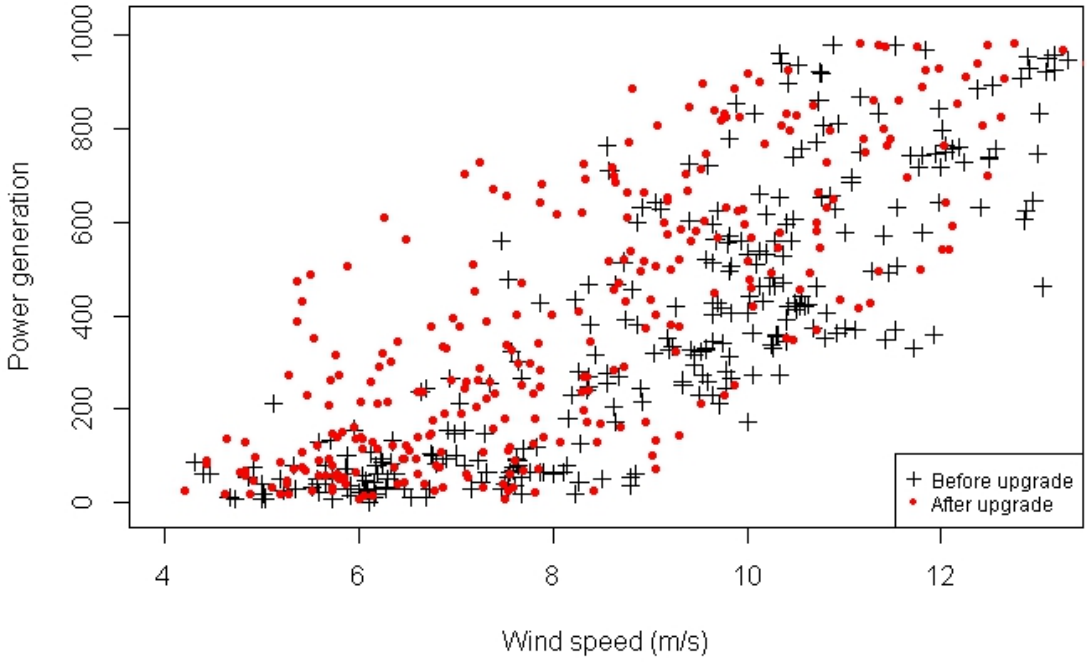

Figure 4.3: Power outputs before and after the VG upgrade in T6

4.2 Mathematical Model

This section presents the mathematical model to quantify the VG effect on the power gain. We build the multi-turbines' power outputs model before and after the VG installation separately and compute the power output difference between the two models.

4.2.1 Modeling power generations before the VG installation

Following the model proposed in Chapter II, we model the wind turbines' power outputs before the VG installation as functions of wind speed and turbulence intensity.

Note that without the VG installation, the wake effect is the only internal factor influencing power generations. Following the global-spatial decomposition proposed in Chapter II, we model the power output of each turbine before the VG upgrade as

$$Y_n^{bf}(v_i, t_i) = G^{bf}(v_i, t_i; \beta^{bf}) + S^{bf}(v_i, t_i; \eta_n^{bf}, \gamma^{bf}) + \epsilon_{n,i}, \quad n = 1, ..., N;\ i = 1, ..., I, \tag{4.1}$$

where $Y_n^{bf}(v_i, t_i)$ denotes the power output of turbine n in the i^{th} sample given the wind speed v_i and turbulence intensity t_i. Parameter $\epsilon_{n,i}$ is a Gaussian white noise with the mean 0 and the variance σ^2.

We model the global component $G^{bf}(v_i, t_i; \beta^{bf})$ in (4.1) as an additive B-spline functions as follows:

$$G^{bf}(v_i, t_i; \beta) = V_{g,i}\beta^{bf,v} + T_{g,i}\beta^{bf,t}, \tag{4.2}$$

where the vectors $V_{g,i}$ and $T_{g,i}$ denote the rows of design matrix corresponding to the B-spline basis of the wind speed v_i and the turbulence intensity t_i, with their associated parameters $\beta^{bf,v}$ and $\beta^{bf,t}$, respectively. The details of constructing the B-spline basis are described in Section 2.6.1.

We model the spatial component $S^{bf}(v_i, t_i; \eta_n, \gamma^{bf})$ in (4.1) with the similar approach discussed in Chapter II as follows:

$$S^{bf}(v_i, t_i; \eta_n^{bf}, \gamma^{bf}) = \eta_n^{bf,v} V_{s,i}\gamma^{bf,v} + \eta_n^{bf,t} T_{s,i}\gamma^{bf,t}, \tag{4.3}$$

where the row vectors $V_{s,i}$ and $T_{s,i}$ denote the rows of design matrix corresponding to the B-spline basis of the wind speed v_i and the turbulence intensity t_i. Here, $V_{g,i}$ and $T_{g,i}$ in (4.2) can be different from $V_{s,i}$ and $T_{s,i}$ in (4.3), respectively, when different degrees in B-spline functions are employed. The two sets of random effects $\eta_n^{bf,v}$ and

$\eta_n^{bf,t}$ for $n = 1, 2, ..., N$ are modeled by the GMRF to represent the interactions among wind turbines. Parameters $\gamma^{bf,v}$ and $\gamma^{bf,t}$ capture the heterogeneous wake effects on power productions over a range of wind speeds and turbulence intensity, respectively.

4.2.2 Modeling the power generations after the VG installation

The VG upgrade may change the spatial interactions among wind turbines. Therefore, we model the power outputs after the upgrade by employing both global and spatial terms.

We take four different approaches. First, from Figure 4.3, we note that the power curve of the upgraded turbine T6 is changed after the VG installation. This upgraded power curve at T6 would be different from those in other non-upgraded turbines. Therefore, we include the upgrade term $\Delta_n(v_i, t_i; \lambda)$ for the upgraded turbine as

$$\text{(Mod 1)} : Y_n^{af}(v_i, t_i) = \hat{G}^{bf}(v_i, t_i; \hat{\beta}^{bf}) + \Delta_n(v_i, t_i; \lambda) + S^{af}(v_i, t_i; \eta_n^{af}, \gamma^{af}) + \epsilon_{n,i}, \tag{4.4}$$

for $n = 1, ..., N; i = 1, ..., I$, where the global component $\hat{G}(v_i, t_i; \hat{\beta}^{bf})$ is estimated using the data before the upgrade in Section 4.2.1, whereas and the spatial component $S^{af}(v_i, t_i; \eta_n, \gamma^{af})$ needs to be re-estimated using the data after the upgrade, because the VG installation may change the turbine interactions.

The upgrade term $\Delta_n(v_i, t_i; \lambda)$ represents the power curve change at the upgraded turbine, defined as

$$\Delta_n(v_i, t_i; \lambda) = \begin{cases} V_{g,i}\lambda^v + T_{g,i}\lambda^t, & \text{for the upgraded turbine} \\ 0, & \text{for other turbines} \end{cases} \tag{4.5}$$

where the covariate vectors $V_{g,i}$ and $T_{g,i}$ are the same row vectors described in (4.2), assuming that the VG upgrade has an impact on the general relationship between the

power productions and wind conditions, which is modeled by the global component. Parameter vectors λ^v and λ^t have same dimensions of $V_{g,i}$ and $T_{g,i}$, respectively, indicating the effect from the VG upgrade on power productions.

Our second approach estimates the global term using the data after the VG upgrade as

$$\text{(Mod 2)}: \quad Y_n^{af}(v_i, t_i) = G^{af}(v_i, t_i; \beta^{af}) + \Delta_n(v_i, t_i; \lambda) + S^{af}(v_i, t_i; \eta_n^{af}, \gamma^{af}) + \epsilon_{n,i}, \tag{4.6}$$

for $n = 1, ..., N; i = 1, ..., I$. In this model, all parameters are estimated with the data collected after the VG upgrade.

We also consider two additional alternative models to estimate the power outputs after the VG installation. Similar to the model proposed in (4.4) and (4.6), we consider the following two models:

$$\text{(Mod 3)}: \quad Y_n^{af}(v_i, t_i) = \hat{G}^{bf}(v_i, t_i; \hat{\beta}^{bf}) + S^{af}(v_i, t_i; \eta_n^{af}, \gamma^{af}) + \epsilon_{n,i}, \tag{4.7}$$

where $\hat{G}^{bf}(v_i, t_i; \hat{\beta^{bf}})$ is estimated by using the data before the VG upgrade, and

$$\text{(Mod 4)}: \quad Y_n^{af}(v_i, t_i) = G^{af}(v_i, t_i; \beta^{af}) + S^{af}(v_i, t_i; \eta_n^{af}, \gamma^{af}) + \epsilon_{n,i}, \tag{4.8}$$

where $G^{af}(v_i, t_i; \beta^{af})$ is estimated by using the data after the VG upgrade. Note that the difference between Mod 3 and 4 and Mod 1 and 2 depends on whether the update term $\Delta_n(v_i, t_i; \lambda)$ is included or not.

Similar to the Bayesian inference made in Chapter II, we estimate the parameters in the Bayesian hierarchical framework. The posterior means are used for estimating parameters in all four models.

4.3 Quantification of VG upgrade

We quantify the site-specific power gain from the VG upgrade. Suppose that the density function of the wind speed's distribution is $f_V(v)$. The turbulence intensity is defined as the ratio of the standard deviation of the wind speed over the mean of the wind speed during a specific interval, e.g., 10 minutes. Therefore, the turbulence intensity is a function of the wind speed v, and we consider the conditional distribution of the turbulence intensity t given the wind speed v as a probability density function $f_{t|v}(t)$.

We quantify the VG effect with the following average power gain (APG) at the n^{th} turbine:

$$\text{APG}(n) = \int_v \left\{ \int_t \left[\hat{Y}_n^{af}(v,t) - \hat{Y}_n^{bf}(v,t) \right] f_{t|v}(t) dt \right\} f_v(v) dv, \tag{4.9}$$

where $\hat{Y}_n^{bf}$ and $\hat{Y}_n^{af}$ denote the estimated power output at the n^{th} turbine before and after the VG upgrade, respectively.

Moreover, we note that other factors such as humidity, temperature and air density also affect the power generation efficiency. As such, we need to eliminate the effect of those factors on the power output when we estimate the power gain from the VG upgrade. We introduce the controlled APG that measures the improvement on the upgraded turbine in comparison with a control turbine as

$$\text{Controlled APG}(n) = APG(n) - APG(n'), \tag{4.10}$$

where n' is the index of the control turbine.

Because the estimated power outputs at each wind speed and turbulence intensity in (4.9)-(4.10) are not in closed-form, we take a sampling-based approach to approximate the APG and the controlled APG. Specifically, we first draw M wind speed

samples $v_m, m = 1, ..., M$, from the density function $f_V(v)$. Then at each sampled v_m, we sample J turbulence intensity samples t_j, $j = 1, ..., J$, from the conditional density function $f_{t|v}(t)$. Then the integration in (4.9) is approximated by

$$\text{APG}(n) \approx \frac{1}{MJ} \sum_{m=1}^{M} \left\{ \sum_{j=1}^{J} \left[\hat{Y}_n^{af}(v_m, t_j) - \hat{Y}_n^{bf}(v_m, t_j) \right] \right\}. \tag{4.11}$$

Similarly we can approximate the controlled APG in (4.10). In our implementation, we use $M = 1000$ and $J = 1000$.

4.4 Case Study

This section performs a case study on a real dataset. This dataset consists of 300 samples before the VG upgrade and 300 samples after the VG upgrade, respectively. We use the data obtained during same season before and after the upgrade, e.g., data collected from May to July.

4.4.1 Implementation results on fitting the power outputs

This section shows the computational results from implementing the proposed methods. In defining the knots for the B-splines, we note that the wind speeds in this dataset range between 4 m/s and 13 m/s. Thus, we choose these two numbers as the boundary knots for the B-splines. In deciding internal knots, we choose internal knot locations of 6 m/s, 7.5 m/s, 9 m/s, and 10.5 m/s. In defining the knots for the turbulence intensities, we consider two internal knots with equal stepwise distance, i.e., 0.33 and 0.66. We normalize the power outputs in 0-1000 scale.

We implement the four models, Mod 1 through Mod 4, discussed in Section 4.2 and evaluate the performance of each model through the 10-fold CV. Table 4.1 summarizes the average RMSE and MAE from the 10 testing sets and its corresponding standard deviations. Among the four models, Mod 2 provides the smallest errors in terms

of both RMSE and MAE, however the differences with other models appear to be negligible.

Table 4.1: Average RMSE and MAE in all turbines from 10-fold CV (unit: normalized power in [0-1000] KW)

Model	RMSE	MAE
Mod 1	159.98 (17.37)	126.44 (12.52)
Mod 2	158.29 (17.24)	125.53 (12.34)
Mod 3	160.94 (18.42)	127.77 (13.96)
Mod 4	160.81 (18.95)	127.84 (14.44)

Note: Numbers inside the parentheses are the standard deviations of fitting errors from the ten testing sets.

Table 4.2 summarizes the average RMSE and MAE only for the upgraded turbine from the 10 testing sets and its corresponding standard deviation. Both average RMSE and MAE in Table 4.2 are larger than their counterparts in Table 4.1. This is because the upgraded turbine is a downstream turbine and in general, power outputs from downstream turbines are more variable than upstream turbines. Similar to that in Table 4.1, Mod 2 provides the smallest errors in terms of both RMSE and MAE among the four alternative models, although the differences are minimal.

Table 4.2: Average RMSE and MAE in the upgraded turbine from 10-fold CV (unit: normalized power in [0-1000] KW)

Model	RMSE	MAE
Mod 1	176.88 (18.51)	143.53 (17.15)
Mod 2	173.84 (15.29)	135.53 (15.07)
Mod 3	177.28 (15.52)	143.27 (15.18)
Mod 4	176.57 (16.16)	138.51 (14.88)

Note: Numbers inside the parentheses are the standard deviations of fitting errors from the ten testing sets.

Figures 4.4(a) and (b) show the actual observations before and after the VG upgrade and the corresponding estimated power outputs of the upgraded turbine from Mod 2. In general, the fitted power outputs capture the power generation pattern well.

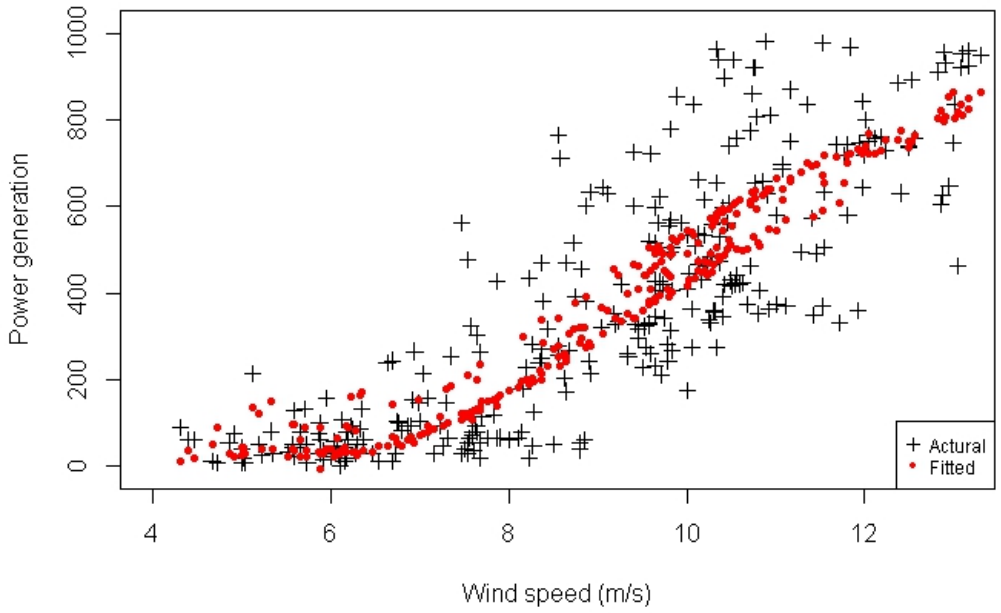

(a) Before the VG upgrade

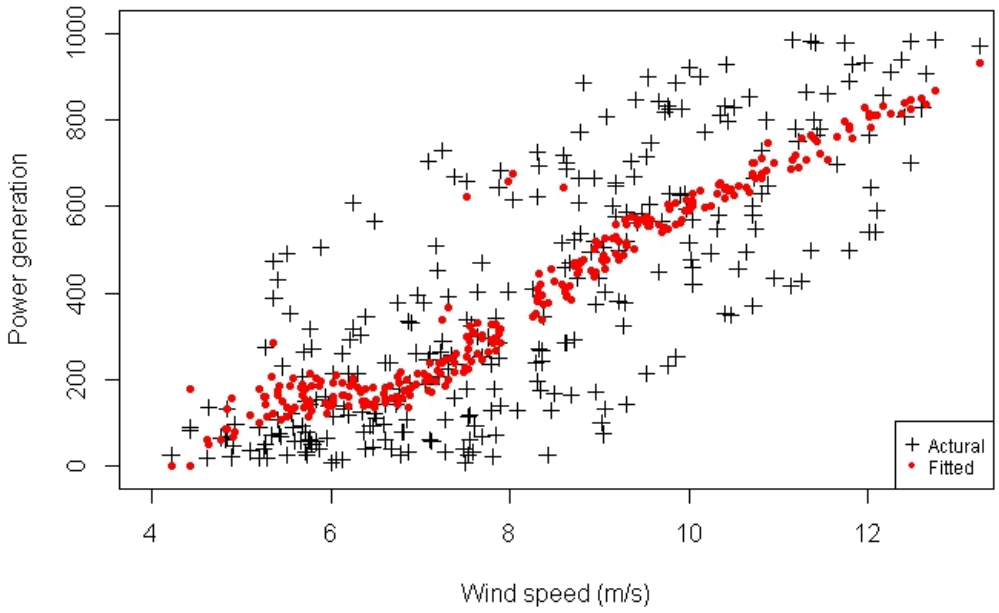

(b) After the VG upgrade

Figure 4.4: Fitted and actual power outputs at T6

To visualize the increased power gain, Figure 4.5 compares the two fitted power outputs of the upgraded turbine from Mod 2, one before and the other after the upgrade. We can clearly observe that the estimated power outputs are larger after the upgrade, indicating the improvement of power generation efficiency. Because the turbulence intensity can be different for the same wind speed, we can observe multiple power outputs given the same wind speed in Figure 4.5.

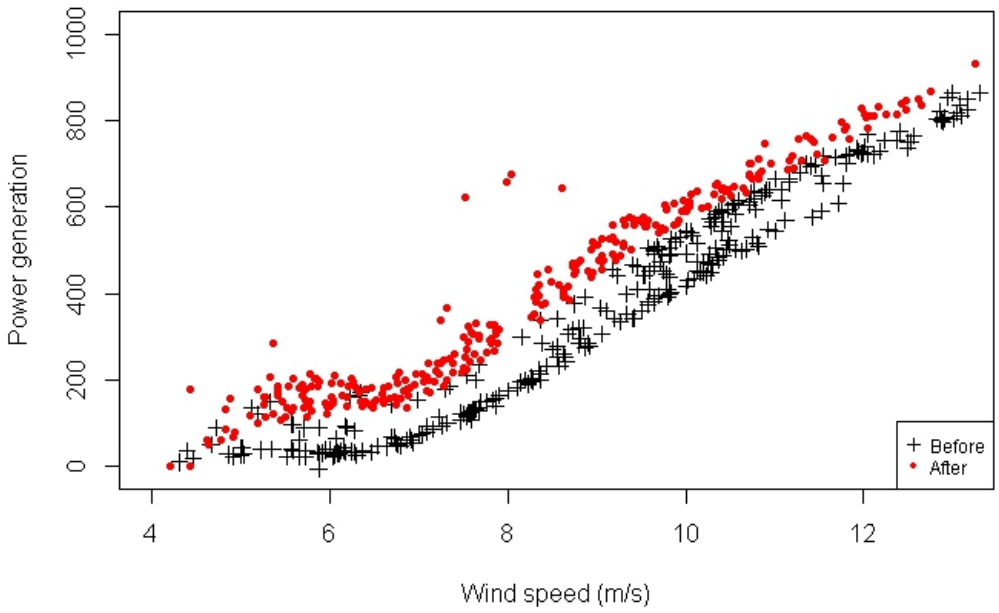

Figure 4.5: Comparison of estimated power outputs at T6 before and after the VG upgrade

4.4.2 Modeling wind conditions

To quantify the APG and the controlled APG, we need to determine the site-specific density functions of the wind speed and turbulence intensity (*Garcia et al.*, 1998; *Hau and Von Renouard*, 2006). First, we fit several different functions including Weibull, Log-normal and Gamma distributions with the observed wind speed measurements. Among them the Weibull distribution appears to provide the best fitting

result in our dataset. Figure 4.6 shows the empirical and fitted distributions of wind speeds as well as the Q-Q and P-P plots, generated from the model utility test using the function fistdist() from the R package "fitdisrplus" (*Delignette-Muller et al.*, 2015). The estimated shape and the scale parameters of the Weibull distribution using the maximum likelihood estimation (MLE) are 1.85 and 6.56, respectively.

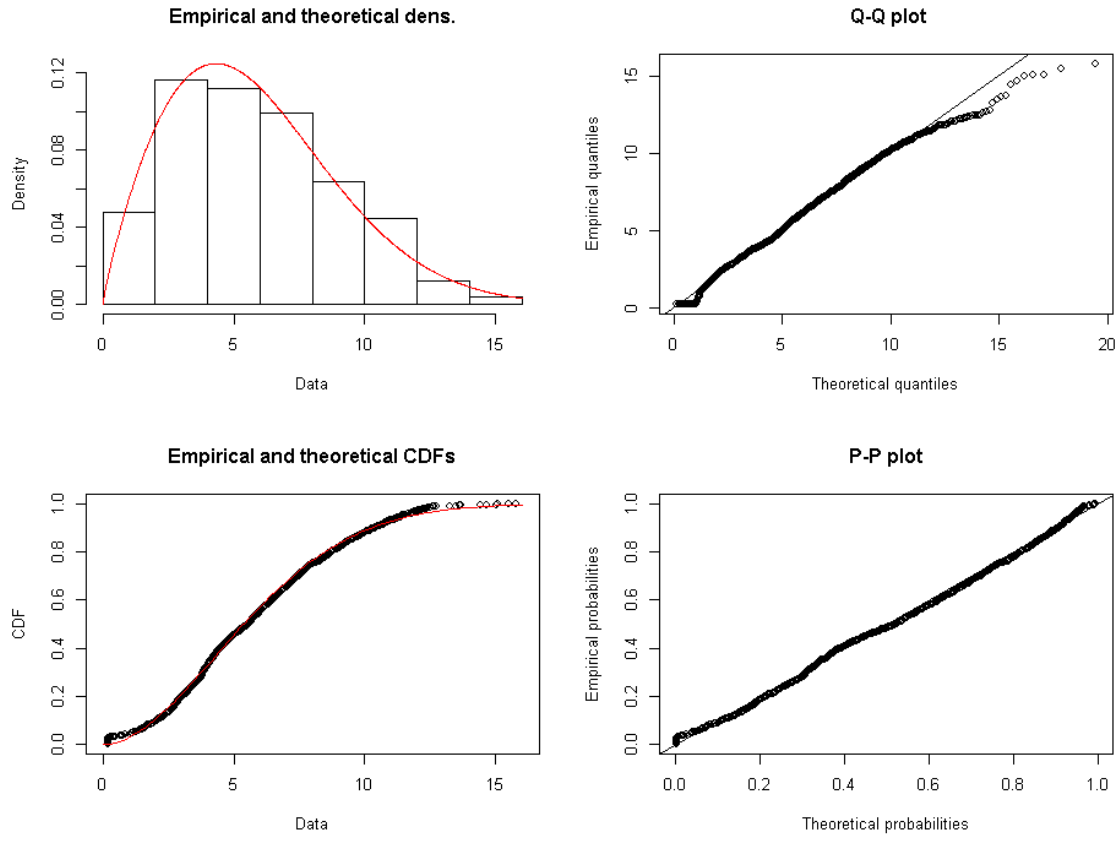

Figure 4.6: Model utility test on the wind speed assuming the Weibull distribution

Considering the fact that the turbulence intensity is always non-negative, we use the log-normal density for modeling the conditional distribution function $f_{t|v}(t)$. To estimate the conditional density function $f_{t|v}(t)$, Figure 4.7 shows the negative correlation between the wind speed and the logarithm of the turbulence intensity in our dataset. We employ a simple linear regression to model the logarithm of the turbulence intensity as a function on the wind speed, and obtain the conditional density of

$f_{t|v}(t)$ as

$$f_{t|v}(t) \sim \log N(-1.842 - 0.102v, 0.4608). \tag{4.12}$$

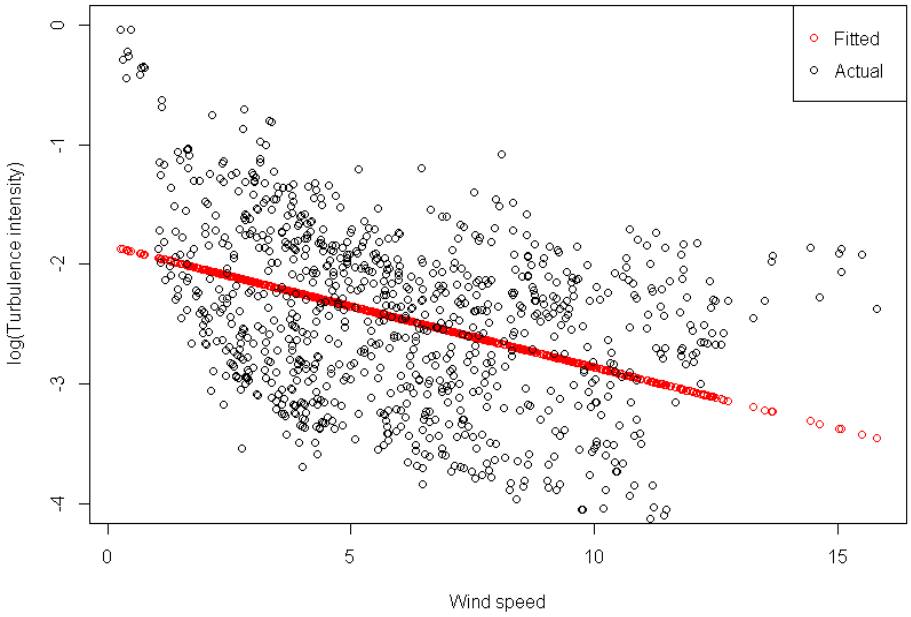

Figure 4.7: Scatter plot of the wind speed and turbulence intensity and fitted regression line

4.4.3 Computational results on quantifying the power gain due to VG upgrade

Based on the results from the 10-fold CV in Section 4.4.1, we use Mod 2 to estimate the APG and controlled APG. We consider two control turbines T1 and T2, which are upstream turbines in the westerly direction (see Figure 4.1).

In addition to obtain the APG and the controlled APG at the upgraded turbine T6 in Figure 4.1, we also compute the APG and the controlled APG at T6's immediate downstream turbine T8. This is to investigate how the VG upgrade at T6 affects the power generation efficiency at its downstream turbine.

Table 4.3 summarizes the estimated APGs and the controlled APGs at the two turbines T6 and T8. The results suggest that the VG installation improves the power generation efficiency at the upgraded turbine (see the second row) in terms of both the APG and the controlled APG. Interestingly, when compared with the two control turbines, the upgraded turbine produces more power after the VG installation date. Moreover, the downstream turbine T8 exhibits the positive controlled APGs after the VG upgrade at T6. This result may indicate that the reduction of the turbulence due to the VG installed at T6 may result in the improvement of the power production at its downstream turbine (*Lin*, 2002; *Massouh and Dobrev*, 2007).

Table 4.3: Estimated APG and controlled APGs with two control turbines (unit: normalized power in [0,1000] KW

	APG	Controlled APG	
		With T1	With T2
Upgraded turbine, T6	98.23	203.74	217.98
Downstream turbine, T8	-1.77	103.74	117.97

However, the power gain we obtain in this case study is much larger than those reported in the literature (*Lee et al.*, 2015b). Therefore, the proposed method in this chapter needs further investigation with more data from several VG upgrade cases.

4.5 Summary

This chapter devises a new approach for quantifying the power gain after the VG upgrade. The method proposed in this chapter considers the wake effects, because the VG installation can alter the interaction pattern with neighbor turbines. The results suggest that a positive power gain can be obtained at the upgraded turbine as well as its downstream turbine. The proposed method can help practitioners evaluate the net profit when they consider the VG installation. The method can be also applicable to quantify the effects of other retrofitting upgrades on the power output at existing turbines. From a financial perspective, wind farm operators could use this method

to evaluate the net profit when deciding to include VGs in new turbines.

CHAPTER V

Conclusions and Future Research Directions

5.1 Conclusions

Based on economics, geography, and transmission constraints, modern utility-scale wind farm developers prefer to site turbines close together. The wake effects of closely sited multiple turbines, however, alters power generation patterns and consequently, a facility's overall power output. Globally, as utility-scale wind farms increase in both number and size, wake effects quantification will become a critical part of efforts to maximize net energy production. Given the U.S. Department of Energys wind vision of 35% by 2050 (*U.S. Department of Energy*, 2015), there is a pressing need to analyze the dynamic characteristics of wind farm operations.

This dissertation discusses three topics in wind energy to meet challenges arising from the interactions among wind turbines. Instead of taking the conventional approach, i.e. estimating the local wind field in a wind farm, this dissertation directly estimates the power outputs of multiple turbines.

The major accomplishments of this dissertation can be outlined as follows:

1. *A new statistical approach for characterizing heterogeneous wake effects under a dominant wind direction*:

   A new approach is proposed for understanding the effects of unobserved wake

effects on the heterogeneous power generations of multiple turbines under the dominant wind direction. The approach decomposes the power outputs into global and spatial components, respectively, to model the average pattern globally shared by all turbines and the turbine-specific variations. In representing the global pattern, B-splines are used to address the nonlinear relationship between power and weather conditions. For the spatial variations, we also use the B-spline functions where the spline regression parameters are modeled through GMRF to capture the interactions among neighboring turbines. A case study using data from a real-world multi-turbine wind farm suggests that the proposed statistical approach successfully characterizes the heterogeneous wake effects, compared with alternative methods.

2. *A new direction-dependent power curve modeling approach for multiple interacting wind turbines*:

   An integrative approach is developed for fitting the direction-dependent power curves of multiple interacting wind turbines. Our approach uses a combination of canonical models and similarity functions to capture the wake correlations in any wind directions. The results of a comprehensive case study suggests that the proposed approach improves the estimation accuracy of power outputs from the multiple turbines compared with other individual approaches. The result also suggests that applying the power curves constructed under a specific direction is not adequate to achieve high estimation accuracy in other directions.

3. *A new approach to quantify the VG upgrade under wake effects*:

   A new approach is devised for quantifying the power gain after the VG upgrade. The proposed method considers the wake effects, because a VG installation can alter the interaction pattern with neighbor turbines. The results suggest that the positive power gain can be obtained at the upgraded turbine as well as its

downstream turbine. The proposed method can help practitioners evaluate the net profit when they consider the VG installation. The method can be also applicable to quantify the effects of other retrofitting upgrades on the power output at existing turbines, or when deciding to include VGs in new turbines.

5.2 Future Research Directions

The methodologies and models developed in this dissertation could be further extended in both methodology and application aspects. Some possible directions are outlines below:

1. *Developments on the Bayesian adaptive regressions splines for the power curve modeling*:

   Throughout the power curve modeling in this dissertation, we empirically choose the knots and degrees in the B-spline functions for modeling the power curve. The results indicate that our choice of knots and degrees empirically fits the power patterns well. However, depending on the wind turbine specification such as cut-in, rated, cut-out wind speeds and rated power, different knots and degrees should be used. In the future research, we plan to consider the splines with the locations of knots determined by the data, rather than being fixed *a priori*, for example, by using the Bayesian multivariate adaptive regression splines (*Lee et al.*, 2013).

2. *Developments on computationally efficient methods to simulate posterior distributions*:

   This dissertation builds models under the Bayesian framework, and uses the MCMC to sample the posterior distributions, which becomes computationally demanding. To analyze large-size wind farms with hundreds of turbines, computationally efficient methods would be appealing for simulating the posterior

distributions. For example, instead of MCMC, the variational Bayes can be employed to reduce the computational time for estimating model parameters (*Woolrich and Behrens*, 2006).

3. *Applications on the wind farm's reliability analysis under the wake effects*:
   Turbines in a downwind location are not only impacted by the wind speed deficits, thus capturing less energy, but they are also subject to increased loads due to the turbulence generated by the upstream turbines. Therefore, downstream turbines could deteriorate faster than upstream turbines. Capitalizing on the wake effect model proposed in this dissertation, the reliability of wind turbines in a wind farm will be analyzed to achieve optimal generation efficiency and ensure reliability in wind farms.

4. *Applications on optimizing the wind farm control*:
   The proposed approach in this dissertation can be possibly used for optimizing the wind farm control (*Senjyu et al.*, 2006; *Yang et al.*, 2016). One possible approach is to include the control parameters in the model. For example, the yaw angle which changes the wake direction can be incorporated into the similarity function proposed in Chapter III. The specific form of the similarity function that incorporates the control parameters will be the subject of our future study.

5. *Applications on the wind farm layout optimization*:
   The proposed approach in this dissertation can be effectively used for wind farm layout design optimization. Specifically, we believe the proposed model can be used as a surrogate model of sophisticated CFD model. The CFD model can achieve a high accuracy in estimating the wake effects, but with a greater computational cost. To overcome the computational difficulty, we can generate a small number of samples from the CFD model to build the proposed model. In particular, in our model, the correlation structure among multiple turbines

depends on the distance among turbines. By generating samples in different distances, we can parameterize the correlation as a function of distance and optimize the inter-distances among turbines. Alternatively, our approach can be used to link the CFD model with simpler engineering models, e.g., Jensen's model. In the literature, statistical surrogate models have been used to link multi-fidelity models (*Qian and Wu*, 2008), based on which the layout optimization can be performed.

BIBLIOGRAPHY

BIBLIOGRAPHY

Adaramola, M., and P.-Å. Krogstad (2011), Experimental investigation of wake effects on wind turbine performance, *Renewable Energy*, *36*(8), 2078–2086.

Ailliot, P., V. Monbet, and M. Prevosto (2006), An autoregressive model with time-varying coefficients for wind fields, *Environmetrics*, *17*(2), 107–117.

Annoni, J., P. Seiler, K. Johnson, P. Fleming, and P. Gebraad (2014), Evaluating wake models for wind farm control, in *American Control Conference (ACC) 2014*, pp. 2517–2523.

Banerjee, S., B. P. Carlin, and A. E. Gelfand (2014), *Hierarchical modeling and analysis for spatial data*, CRC Press.

Barbounis, T. G., J. B. Theocharis, M. C. Alexiadis, and P. S. Dokopoulos (2006), Long-term wind speed and power forecasting using local recurrent neural network models, *IEEE Transactions on Energy Conversion*, *21*(1), 273–284.

Barton, J. P., and D. G. Infield (2004), Energy storage and its use with intermittent renewable energy, *IEEE Transactions on Energy Conversion*, *19*(2), 441–448.

Besag, J. (1974), Spatial interaction and the statistical analysis of lattice systems, *Journal of the Royal Statistical Society, Series B*, *36*(2), 192–236.

Bessa, R. J., V. Miranda, A. Botterud, J. Wang, and E. M. Constantinescu (2012), Time adaptive conditional kernel density estimation for wind power forecasting, *IEEE Transactions on Sustainable Energy*, *3*(4), 660–669.

Bianchi, F. D., R. J. Mantz, and H. De Battista (2007), *The Wind and Wind Turbines*, Springer.

Boyle, G. (2012), *Renewable Energy: Power for a Sustainable Future*, Oxford University Press and Open University.

Brake, D., J. Hammitt, and G. Pechlivanoglou (2014), Method for determining optimum vortex generator placement for maximum efficiency on a retrofitted wind turbine generator of unknown aerodynamic design, U.S. Patent 8,746,053.

Byon, E. (2013), Wind turbine operations and maintenance: A tractable approximation of dynamic decision-making, *IIE Transactions*, *45*(11), 1188–1201.

Byon, E., L. Ntaimo, and Y. Ding (2010), Optimal maintenance strategies for wind turbine systems under stochastic weather conditions, *IEEE Transactions on Reliability*, *59*(2), 393–404.

Byon, E., Y. Choe, and N. Yampikulsakul (2016), Adaptive modeling and prediction in time-variant processes with application to wind power systems, *IEEE Transactions on Automation Science and Engineering*, *13*(2), 997–1007.

Chen, P., T. Pedersen, B. Bak-Jensen, and Z. Chen (2010), Arima-based time series model of stochastic wind power generation, *IEEE Transactions on Power Systems*, *25*(2), 667–676.

Choe, Y., E. Byon, and N. Chen (2015), Importance sampling for reliability evaluation with stochastic simulation models, *Technometrics*, *57*(3), 351–361.

Chowdhury, S., J. Zhang, A. Messac, and L. Castillo (2012), Unrestricted wind farm layout optimization (uwflo): Investigating key factors influencing the maximum power generation, *Renewable Energy*, *38*(1), 16–30.

Christiansen, M. B., and C. B. Hasager (2005), Wake effects of large offshore wind farms identified from satellite sar, *Remote Sensing of Environment*, *98*(2), 251–268.

Crespo, A., J. Hernandez, and S. Frandsen (1999), Survey of modelling methods for wind turbine wakes and wind farms, *Wind Energy*, *2*(1), 1–24.

Cressie, N. (2015), *Statistics for spatial data*, John Wiley & Sons.

Curvers, A., and P. Van der Werff (2008), OWEZ wind farm efficiency, *Tech. Rep. ECN-E–08-092*.

Damousis, I. G., M. C. Alexiadis, J. B. Theocharis, and P. S. Dokopoulos (2004), A fuzzy model for wind speed prediction and power generation in wind parks using spatial correlation, *IEEE Transactions on Energy Conversion*, *19*(2), 352–361.

de Almeida, R. G., E. D. Castronuovo, and J. P. Lopes (2006), Optimum generation control in wind parks when carrying out system operator requests, *IEEE Transactions on Power Systems*, *21*(2), 718–725.

Delignette-Muller, M. L., C. Dutang, et al. (2015), fitdistrplus: An r package for fitting distributions, *Journal of Statistical Software*, *64*(4), 1–34.

Dowell, J., and P. Pinson (2016), Very-short-term probabilistic wind power forecasts by sparse vector autoregression, *IEEE Transactions on Smart Grid*, *7*(2), 763–770.

Enkvist, P., T. Nauclér, and J. Rosander (2007), A cost curve for greenhouse gas reduction, *McKinsey Quarterly*, *1*, 34.

Fleming, P. A., P. M. O. Gebraad, S. Lee, J.-W. van Wingerden, K. Johnson, M. Churchfield, J. Michalakes, P. Spalart, and P. Moriarty (2014), Evaluating techniques for redirecting turbine wakes using SOWFA, *Renewable Energy*, *70*, 211–218.

Flohr, P., E. Gutmark, B. Paikert, and C. Paschereit (2003), Vortex generator with controlled wake flow, U.S. Patent App. 10/621,379.

Friedman, J., T. Hastie, and R. Tibshirani (2009), *The elements of statistical learning: data mining, inference, and prediction*, Springer, 2nd ed.

Fthenakis, V., and H. C. Kim (2009), Land use and electricity generation: A life-cycle analysis, *Renewable and Sustainable Energy Reviews*, *13*(6), 1465–1474.

Garcia, A., J. Torres, E. Prieto, and A. De Francisco (1998), Fitting wind speed distributions: a case study, *Solar Energy*, *62*(2), 139–144.

Gelman, A. (2006), Prior distributions for variance parameters in hierarchical models (comment on article by browne and draper), *Bayesian analysis*, *1*(3), 515–534.

Gilks, W. R., and P. Wild (1992), Adaptive rejection sampling for Gibbs sampling, *Applied Statistics*, pp. 337–348.

Hansen, K. S., R. J. Barthelmie, L. E. Jensen, and A. Sommer (2012), The impact of turbulence intensity and atmospheric stability on power deficits due to wind turbine wakes at horns rev wind farm, *Wind Energy*, *15*(1), 183–196.

Harvey, A., and S. J. Koopman (1993), Forecasting hourly electricity demand using time-varying splines, *Journal of the American Statistical Association*, *88*(424), 1228–1236.

Hau, E., and H. Von Renouard (2006), *The wind resource*, Springer.

Hoff, P. D. (2009), *A first course in Bayesian statistical methods*, Springer Science & Business Media.

Jensen, N. O. (1983), A note on wind generator interaction, *Technical Report. Riso-M-2411*, Riso National Laboratory, Roskilde, Denmark.

Jeon, J., and J. W. Taylor (2012), Using conditional kernel density estimation for wind power density forecasting, *Journal of the American Statistical Association*, *107*(497), 66–79.

Johnson, K. E., and N. Thomas (2009), Wind farm control: addressing the aerodynamic interaction among wind turbines, in *Proceedings of the 2009 conference on American Control Conference*, pp. 2104–2109.

Kaiser, M. S., M. J. Daniels, K. Furakawa, and P. Dixon (2002), Analysis of particulate matter air pollution using Markov random field models of spatial dependence, *Environmetrics*, *13*(5-6), 615–628.

Kaltschmitt, M., W. Streicher, and A. Wiese (2007), *Renewable energy: technology, economics and environment*, Springer Science & Business Media.

Kariniotakis, G., G. Stavrakakis, and E. Nogaret (1996), Wind power forecasting using advanced neural networks models, *IEEE transactions on Energy Conversion*, *11*(4), 762–767.

Katic, I., J. Højstrup, and N. Jensen (1986), A simple model for cluster efficiency, in *European Wind Energy Association Conference and Exhibition*, pp. 407–410.

Kéry, M., and M. Schaub (2011), *Bayesian population analysis using WinBUGS: a hierarchical perspective*, Academic Press.

Kim, S.-H., H.-K. Shin, Y.-C. Joo, and K.-H. Kim (2015), A study of the wake effects on the wind characteristics and fatigue loads for the turbines in a wind farm, *Renewable Energy*, *74*, 536 – 543.

Korpaas, M., A. T. Holen, and R. Hildrum (2003), Operation and sizing of energy storage for wind power plants in a market system, *International Journal of Electrical Power & Energy Systems*, *25*(8), 599–606.

Kusiak, A., and Z. Song (2010), Design of wind farm layout for maximum wind energy capture, *Renewable Energy*, *35*(3), 685–694.

Lackner, M. A., and C. N. Elkinton (2007), An analytical framework for offshore wind farm layout optimization, *Wind Engineering*, *31*(1), 17–31.

Lee, G., E. Byon, L. Ntaimo, and Y. Ding (2013), Bayesian spline method for assessing extreme loads on wind turbines, *The Annals of Applied Statistics*, *7*(4), 2034–2061.

Lee, G., Y. Ding, M. G. Genton, and L. Xie (2015a), Power curve estimation with multivariate environmental factors for inland and offshore wind farms, *Journal of the American Statistical Association*, *110*(509), 56–67.

Lee, G., Y. Ding, L. Xie, and M. G. Genton (2015b), A kernel plus method for quantifying wind turbine performance upgrades, *Wind Energy*, *18*(7), 1207–1219.

Lei, M., L. Shiyan, J. Chuanwen, L. Hongling, and Z. Yan (2009), A review on the forecasting of wind speed and generated power, *Renewable and Sustainable Energy Reviews*, *13*(4), 915–920.

Li, H., K. Shi, and P. McLaren (2005), Neural-network-based sensorless maximum wind energy capture with compensated power coefficient, *IEEE Transactions on Industry Applications*, *41*(6), 1548–1556.

Li, S., D. C. Wunsch, E. A. O'Hair, and M. G. Giesselmann (2001), Using neural networks to estimate wind turbine power generation, *IEEE Transactions on Energy Conversion*, *16*(3), 276–282.

Lin, J. C. (2002), Review of research on low-profile vortex generators to control boundary-layer separation, *Progress in Aerospace Sciences*, *38*(4), 389–420.

Lunn, D., C. Jackson, N. Best, A. Thomas, and D. Spiegelhalter (2012), *The BUGS Book: A Practical Introduction to Bayesian Analysis*, CRC Press, Boca Raton, FL.

Massouh, F., and I. Dobrev (2007), Exploration of the vortex wake behind of wind turbine rotor, in *Journal of Physics: Conference Series*, vol. 75, p. 012036, IOP Publishing.

Mohandes, M., T. Halawani, S. Rehman, and A. A. Hussain (2004), Support vector machines for wind speed prediction, *Renewable Energy*, *29*(6), 939–947.

Mueller-Vahl, H., G. Pechlivanoglou, C. Nayeri, and C. Paschereit (2012), Vortex generators for wind turbine blades: A combined wind tunnel and wind turbine parametric study, in *ASME Turbo Expo 2012: Turbine Technical Conference and Exposition*, pp. 899–914, American Society of Mechanical Engineers.

Ntzoufras, I. (2011), *Bayesian modeling using WinBUGS*, vol. 698, John Wiley & Sons.

Ortega, J. M. (1987), *Matrix Theory*, Plenum Press, New York and London.

Paraschivoiu, I. (2002), *Wind turbine design: with emphasis on Darrieus concept*, Presses inter Polytechnique.

Plummer, M., N. Best, K. Cowles, and K. Vines (2006), Coda: convergence diagnosis and output analysis for mcmc, *R news*, *6*(1), 7–11.

Porté-Agel, F., H. Lu, and Y.-T. Wu (2010), A large-eddy simulation framework for wind energy applications, in *Fifth International Symposium on Computational Wind Engineering*.

Pourhabib, A., J. Z. Huang, and Y. Ding (2016), Short-term wind speed forecast using measurements from multiple turbines in a wind farm, *Technometrics*, *58*(1), 138–147.

Qian, P. Z. G., and C. F. J. Wu (2008), Bayesian hierarchical modeling for integrating low-accuracy and high-accuracy experiments, *Technometrics*, *50*(2), 192–204.

Quan, H., D. Srinivasan, and A. Khosravi (2014), Short-term load and wind power forecasting using neural network-based prediction intervals, *IEEE Transactions on Neural Networks and Learning Systems*, *25*(2), 303–315.

American Wind Energy Association (2014), Wind power's consumer benefits, *Technical report.*, Washington DC.

American Wind Energy Association (2015), AWEA U.S. wind industry first quarter 2015 market report, *Technical report.*, Washington DC.

U.S. Department of Energy (2015), Wind vision: A new era for wind power in the united states, *Technical Report. DOE/GO-102015-4557*, Washington DC.

U.S. Global Wind Energy Council (2015), GWEZ global wind statistics 2014, *Technical report.*, Brussels, Belgium.

DTU Wind Energy (2015), Wind resources for energy production of wind turbines, `http://www.wasp.dk/wasp#details__wakeeffectmodel`, accessed: 2015-09-18.

National Renewable Energy Laboratory (2012), High-tech tools tackle wind farm performance, `http://www.nrel.gov/news/features/2012/1995`, accessed: 2017-04-23.

UpWind Solutions (2015), Windpower engineering webinar - vortex generators on wind turbines, `https://www.slideshare.net/upwindsolutions/windpower-engineering-webinar-vortex-generators-on-wind-turbines`, accessed: 2017-04-17.

Rue, H., and L. Held (2005), *Gaussian Markov random fields: theory and applications*, CRC Press.

Salcedo-Sanz, S., E. G. Ortiz-Garcı, Á. M. Pérez-Bellido, A. Portilla-Figueras, L. Prieto, et al. (2011), Short term wind speed prediction based on evolutionary support vector regression algorithms, *Expert Systems with Applications*, *38*(4), 4052–4057.

Sánchez, I. (2006), Recursive estimation of dynamic models using cook's distance, with application to wind energy forecast, *Technometrics*, *48*(1), 61–73.

Senjyu, T., R. Sakamoto, N. Urasaki, T. Funabashi, H. Fujita, and H. Sekine (2006), Output power leveling of wind turbine generator for all operating regions by pitch angle control, *IEEE Transactions on Energy Conversion*, *21*(2), 467–475.

Staid, A. (2015), Statistical modeling to support power system planning, Ph.D. thesis, Johns Hopkis University, Washington D.C.

Storms, B. L., and C. S. Jang (1994), Lift enhancement of an airfoil using a gurney flap and vortex generators, *Journal of Aircraft*, *31*(3), 542–547.

Sturtz, S., U. Ligges, and A. E. Gelman (2005), R2WinBUGS: a package for running WinBUGS from R, *Journal of Statistical software*, *12*(3), 1–16.

Sullivan, T. (1984), Effect of vortex generators on the power conversion performance and structural dynamic loads of the mod-2 wind turbine, *National Aeronautics and Space Administration Report*, *1*.

Timmer, W., and R. Van Rooij (2003), Summary of the delft university wind turbine dedicated airfoils, in *ASME 2003 Wind Energy Symposium*, pp. 11–21, American Society of Mechanical Engineers.

Vermeer, L., J. N. Sørensen, and A. Crespo (2003), Wind turbine wake aerodynamics, *Progress in Aerospace Sciences*, *39*(6), 467–510.

Weigt, H. (2009), Germanys wind energy: The potential for fossil capacity replacement and cost saving, *Applied Energy*, *86*(10), 1857–1863.

Woolrich, M. W., and T. E. Behrens (2006), Variational bayes inference of spatial mixture models for segmentation, *IEEE Transactions on Medical Imaging*, *25*(10), 1380–1391.

Wu, Y.-T., and F. Porté-Agel (2011), Large-eddy simulation of wind-turbine wakes: evaluation of turbine parametrisations, *Boundary-layer Meteorology*, *138*(3), 345–366.

Yampikulsakul, N., E. Byon, S. Huang, S. Shawn, and M. You (2014), Condition monitoring of wind turbine system with nonparametric regression-based analysis, *IEEE Transactions on Energy Conversion*, *29*(2), 288–299.

Yang, H., K. Xie, H.-M. Tai, and Y. Chai (2016), Wind farm layout optimization and its application to power system reliability analysis, *IEEE Transactions on Power Systems*, *31*(3), 2135–2143.

You, M., E. Byon, J. Jin, and G. Lee (2017), When wind travels through turbines: A new statistical approach for characterizing heterogeneous wake effects in multi-turbine wind farms, *IIE Transactions*, *49*(1), 84–95.

Zaher, A., S. McArthur, D. Infield, and Y. Patel (2009), Online wind turbine fault detection through automated scada data analysis, *Wind Energy*, *12*(6), 574–593.